Volume 6 DECEMBER, 1935 Number 12

PHYSICS

A Journal of General and Applied Physics

Effect of Certain Discontinuities on the Pressure Distribution in a Loaded Soil

M. A. BIOT, *Graduate School of Engineering, Harvard University*

(Received June 21, 1935)

The pressure distribution due to a concentrated load on a semi-infinite elastic body is given by the well-known Boussinesq solution for either the two-dimensional or three-dimensional case. We here investigate the effect on such a pressure distribution, taken at the depth h, of the presence at that depth of a slippery rigid bed (case (b)); of a perfectly rough rigid bed (case (c)); and of a perfectly flexible but inextensible thin layer embedded in the material (case (d)). Both pressure distributions in the two and three-dimensional problems are calculated for each case, Fig. 5 and Fig. 6. Several authors have already investigated case (b) and case (c) in two dimensions (2), (3). Their results are in perfect accordance with ours. The author is indebted to Dr. A. Casagrande for suggesting this investigation as a contribution to the field of soil mechanics.

GENERAL SOLUTION OF THE EQUATIONS OF ELASTICITY

IN the following paper, solutions of the equations of elasticity are needed which give both the stresses and the displacements. Therefore it will be easier to start from the equations relating the displacements u, v, w.

$$\nabla^2 u+\frac{1}{1-2\nu}\frac{\partial\Theta}{\partial x}=0,\quad \nabla^2 v+\frac{1}{1-2\nu}\frac{\partial\Theta}{\partial y}=0,\quad \nabla^2 w+\frac{1}{1-2\nu}\frac{\partial\Theta}{\partial z}=0 \tag{1}$$

where $\nabla^2=\frac{\partial^2}{\partial x^2}+\frac{\partial^2}{\partial y^2}+\frac{\partial^2}{\partial z^2}$, $\Theta=\frac{\partial u}{\partial x}+\frac{\partial v}{\partial y}+\frac{\partial w}{\partial z}$,

ν is the Poisson ratio of the material.

It was established by Neuber[1] that a general solution of these equations may be found as follows.

We call Φ_0 a scalar function of x, y, z satisfying the Laplace equation $\nabla^2\phi_0=0$.

We call Φ a vector, such that each of its Cartesian components ϕ_x ϕ_y ϕ_z satisfies the Laplace equation

$$\nabla^2\phi_x=0,\quad \nabla^2\phi_y=0,\quad \nabla^2\phi_z=0.$$

A very general solution of the equations of elasticity (1) can then be expressed as

$$\begin{aligned} u&=-(\partial/\partial x)(\phi_0+x\phi_x+y\phi_y+z\phi_z)+4(1-\nu)\phi_x,\\ v&=-(\partial/\partial y)(\phi_0+x\phi_x+y\phi_y+z\phi_z)+4(1-\nu)\phi_y,\\ w&=-(\partial/\partial z)(\phi_0+x\phi_x+y\phi_y+z\phi_z)+4(1-\nu)\phi_z; \end{aligned} \tag{2}$$

or in vectorial notation

$$\mathbf{u}=-\text{grad}\,(\phi_0+\mathbf{r}\cdot\Phi)+4(1-\nu)\Phi.$$

The expression for Θ becomes in terms of the arbitrary functions above

$$\Theta=\text{div}\,\mathbf{u}=-\text{div grad}\,\phi_0-\text{div grad}\,\mathbf{r}\cdot\Phi+4(1-\nu)\,\text{div}\,\Phi.$$

Since $\text{div grad}\,\phi_0=\nabla^2\phi_0=0$

and $\text{div grad}\,\mathbf{r}\cdot\Phi=\nabla^2(x\phi_x+y\phi_y+z\phi_z)=2\,\text{div}\,\Phi$,

we find $$\Theta=2(1-2\nu)\,\text{div}\,\Phi. \tag{3}$$

The vertical stress component σ_z and the horizontal shear $\tau_{xz}\tau_{yz}$ are the only stress com-

[1] Neuber, "Ein neuer Ansatz zür Lösung räumlicher Probleme der Elastizitätstheorie," Zeits. f. angew. Math. und Mechanik **14**, 4 (1934).

ponents we shall need in the following theory. They are given by

$$\frac{\sigma_z}{2G}=\frac{\partial w}{\partial z}+\frac{\nu\Theta}{1-2\nu},\quad \frac{\tau_{xz}}{G}=\frac{\partial w}{\partial x}+\frac{\partial u}{\partial z},\quad \frac{\tau_{yz}}{G}=\frac{\partial w}{\partial y}+\frac{\partial v}{\partial z}, \tag{4}$$

where G is the shear modulus of the material and ν the Poisson ratio.

It is important to note that the factor $(1-2\nu)$ disappears in the value of σ_z when using the value of Θ given by (3),

$$\sigma_z/2G=\partial w/\partial z+2\nu \operatorname{div}\Phi. \tag{4$_1$}$$

This shows that the value of the term $\nu\Theta/(1-2\nu)$ when $\nu=\frac{1}{2}$, $\Theta=0$, tends toward the limit $2\nu \operatorname{div}\Phi$.

The Two-Dimensional Problem

Let us consider first the two-dimensional problem where the load is concentrated on a line and has the value P per unit length (Fig. 1). We shall assume that the ground is elastic, of elasticity modulus E, and shall restrict ourselves to the case where the Poisson ratio is $\nu=\frac{1}{2}$, which means that the material of the ground is supposed to be incompressible. Four cases will be investigated.

(a) The ground is infinitely extended and deep. The pressure distribution at the depth h is given by the well-known Boussinesq solution.

(b) The ground is infinitely extended but of finite depth h. It is resting on a rock base, perfectly rigid; no friction forces are supposed to act between the rock and the upper ground. They can slip with respect to each other without the slightest resistance (Fig. 2). This case has been calculated by various authors.[2] Their result, derived by a different method, is found in proper accordance with ours.

(c) The same case as in (b) but where perfect adhesion is supposed to exist between the upper ground layer and the rock surface. No slippage whatever is allowed to occur; the two materials are assumed to stick together perfectly. This case was investigated by Marguerre[3] for $\nu=0$. Comparison with his paper shows that there is no practical difference between the cases $\nu=0$ and $\nu=\frac{1}{2}$. The pressure distribution is calculated at the rock surface (depth h).

(d) There is a horizontal infinite inextensible but perfectly flexible layer at the depth h. The pressure distribution on that layer due to P is calculated. This case corresponds to the problem of a clay substratum containing a thin horizontal sand layer.

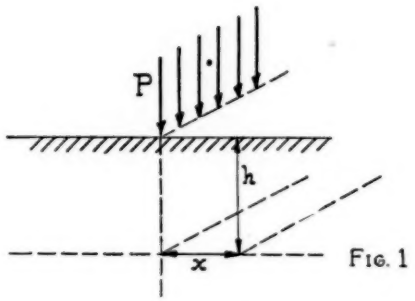

Fig. 1

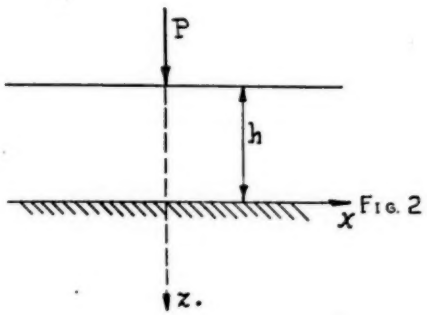

Fig. 2

In cases (a) and (b) the pressure distribution is found to be independent of the elasticity constants of the ground, while it depends on the Poisson ratio ν for cases (d) and (c). Hence the result for cases (a) and (b) is not affected by the restrictive assumption that $\nu=\frac{1}{2}$.

Case (a)

We take the z axis directed positive downward, the x axis being at the surface of the ground, and we assume that all the xz planes are identical. It is possible to find solutions of the elasticity equations for which all the variables are cosine or sine functions of x by the assumption:

$$\phi_0=(Ae^{\lambda z}+Be^{-\lambda z})\cos\lambda x,\qquad \phi_z=(Ce^{\lambda z}+De^{-\lambda z})\cos\lambda x,\quad \phi_x=\phi_y=0, \tag{5}$$

where A, B, C, D, λ, are arbitrary constants.

By substituting this into Eqs. (2), (4) and (4$_1$), we obtain;

$$\frac{\sigma_z}{2G}=-\frac{\partial^2\phi_0}{\partial z^2}-z\frac{\partial^2\phi_z}{\partial z^2}+2(1-\nu)\frac{\partial\phi_z}{\partial z},\qquad \frac{\tau_{xz}}{G}=-\frac{2\partial}{\partial x}\left[\frac{\partial\phi_0}{\partial z}+z\frac{\partial\phi_z}{\partial z}-(1-2\nu)\phi_z\right]. \tag{6}$$

Since we assume incompressibility, $\nu=\frac{1}{2}$,

$$\sigma_z/2G=-\partial^2\phi_0/\partial z^2-z\partial\phi_z/\partial z^2+\partial\phi_z/\partial z,$$
$$\tau_{xz}/G=-2(\partial/\partial x)[\partial\phi_0/\partial z+z\partial\phi_z/\partial z]. \quad (7)$$

At infinite depth we must have $\sigma_z=\tau_{xz}=0$ and this is only possible if $A=C=0$. We then have

$$\tau_{xz}/G=2\lambda \sin \lambda x[-B\lambda e^{-\lambda z}-zD\lambda e^{-\lambda z}].$$

By introducing the condition that the surface carries only a normal load and no shear, τ_{xz} must be zero for $z=0$, hence $B=0$. The expression for σ_z then reduces to

$$\sigma_z/2G=-D\lambda e^{-\lambda z}(1+z\lambda)\cos \lambda x.$$

This last relation shows that if the surface $z=0$ is loaded with a normal pressure distribution, $-\sigma_{z0}=q_0 \cos \lambda x$, the pressure at the depth $z=h$ is

$$-\sigma_z=q=q_0 e^{-\lambda h}(1+h\lambda)\cos \lambda x. \quad (8)$$

Now an arbitrary surface loading $p_0(x)$ may be represented by means of the Fourier integral as a superposition of sine loadings of various wave-lengths.

$$p_0(x)=(1/\pi)\int_0^\infty d\lambda\int_{-\infty}^{+\infty} d\xi p_0(\xi)\cos \lambda(x-\xi).$$

The pressure distribution $q(x)$ at the depth h is derived from relation (8) and the above Fourier integral.

$$q(x)=\frac{1}{\pi}\int_0^\infty d\lambda\int_{-\infty}^{\infty} d\xi p_0(\xi)e^{-\lambda h}(1+h\lambda)\cos \lambda(x-\xi),$$

which can be written

$$q(x)=\frac{1}{\pi}\int_{-\infty}^{+\infty} p_0(\xi)d\xi\int_0^\infty d\lambda e^{-\lambda h}(1+h\lambda)\cos \lambda(x-\xi).$$

If the surface loading $p_0(x)$ is concentrated within a small region $(-\epsilon,+\epsilon)$ such that the total load is

$$P=\int_{-\epsilon}^{\epsilon} p(\xi)d\xi.$$

The pressure distribution at a depth h due to that load is

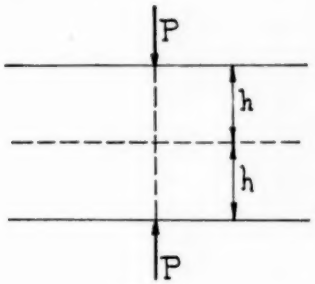

FIG. 3.

$$q(x)=(P/\pi)\int_0^\infty e^{-\lambda h}(1+\lambda h)\cos \lambda x d\lambda,$$
$$q(x)=(P/\pi h)\int_0^\infty e^{-\alpha}(1+\alpha)\cos \alpha(x/h)d\alpha. \quad (9)$$

As will be seen, this yields the well-known Boussinesq solution.

Case (b)

The soft ground is supposed to rest on a rigid rock base, no friction occurring at the surface of contact (Fig. 2). This case is identical with the symmetrical loading illustrated by Fig. 3. In order to proceed as in case (a) and use the Fourier integral, we first have to consider a sinusoidal loading which is symmetrical with respect to the plane at depth h.

We take the x axis at the rock surface, the surface of the ground being at $z=h$ and its symmetrical image at $z=-h$, (Fig. 3). A symmetrical solution of the equations of elasticity is found by putting

$$\phi_0=\cosh \lambda z \cos \lambda x, \quad \phi_z=A \sinh \lambda z \cos \lambda x.$$

The application of formula (7) gives the value of the horizontal shear.

$$\tau_{xz}/G=2\lambda \sin \lambda x[\lambda \sinh \lambda z+Az\lambda \cosh \lambda z].$$

Since no shear is acting at the boundaries $z=\pm h$, we have the condition

$$\sinh \lambda h+hA \cosh \lambda h=0$$

or

$$A=-\sinh \lambda h/h \cosh h\lambda.$$

With this value of A the value of σ_z is given by Eq. (7).

$$\frac{\sigma_z}{2G}=\left[\frac{z}{h}\frac{\sinh \lambda h \sinh \lambda z}{\cosh \lambda h}-\frac{\sinh \lambda h \cosh \lambda z}{\lambda h \cosh \lambda h}-\cosh \lambda z\right]\times\lambda^2 \cos \lambda x.$$

This last relation shows that if a pressure $q_0 \cos \lambda x$ is acting at $z=-h$, the pressure q on the plane of symmetry $z=0$, which represents the rock surface, is

$$q=\frac{2(\sinh \lambda h+\lambda h \cosh \lambda h)}{\sinh 2\lambda h+2\lambda h} q_0 \cos \lambda x.$$

Proceeding as in case (a) by the use of the Fourier integral, we find the pressure distribution at $z=0$ due to a concentrated load P at the surface $z=-h$

$$p=\frac{2P}{\pi h}\int_0^\infty \frac{\alpha \cosh \alpha+\sinh \alpha}{\sinh 2\alpha+2\alpha} \cos \alpha \frac{x}{h} d\alpha. \quad (10)$$

This checks with the formula found by Melan.[2] It gives the pressure p at the rock surface when no friction occurs as a function of the horizontal distance x from the vertical line of application of the load P.

Case (c)

This case considers the same material, soft ground lying on rigid rock, but here the upper soft material is supposed to stick perfectly to the rock surface.

We take the x axis at the rock surface and the z axis directed positive downward, as in case (b), (Fig. 2), and start from a solution which is sinusoidal along x

$$\begin{aligned}\phi_0&=(Ae^{\lambda z}+Be^{-\lambda z})\cos \lambda x,\\ \phi_z&=(Ce^{\lambda z}+De^{-\lambda z})\cos \lambda x, \quad (11)\\ \phi_x&=\phi_y=0.\end{aligned}$$

We have three boundary conditions

$$u=0 \text{ at } z=0,\ w=0 \text{ at } z=0,\ \tau_{zz}=0 \text{ at } z=-h. \quad (12)$$

We remember that we assume the soft material to be incompressible ($\nu=\frac{1}{2}$). With this value of the Poisson ratio, we get from formulae (2) and (7)

$$\begin{aligned}u&=\lambda \sin \lambda x[Ae^{\lambda z}+Be^{-\lambda z}+zCe^{\lambda z}+zDe^{-\lambda z}],\\ w&=-\cos \lambda x[(Ae^{\lambda z}-Be^{-\lambda z})\lambda\\ &\quad +Ce^{\lambda z}(\lambda z-1)-De^{-\lambda z}(\lambda z+1)],\\ \tau_{zz}/G&=2\lambda \sin \lambda x[(Ae^{\lambda z}-Be^{-\lambda z})\lambda\\ &\quad +z\lambda(Ce^{\lambda z}-De^{-\lambda z})],\\ \sigma_z/2G&=\lambda \cos \lambda x[Ce^{\lambda z}(1-\lambda z)\\ &\quad -De^{-\lambda z}(1+\lambda z)-\lambda(Ae^{\lambda z}+Be^{-\lambda z}). \quad (13)\end{aligned}$$

The three boundary conditions determine three of the constants $A\ B\ C\ D$ in terms of the fourth one. Calculating the coefficients $B\ C\ D$ in terms of A, we find that the value of σ_z at the rock surface ($z=0$) is

$$\sigma_z/2G=2A\lambda^2 \cos \lambda x(\cosh \lambda h+h\lambda \sinh \lambda h)/\lambda h \cosh \lambda h$$

and at the surface of the ground ($z=-h$) it is

$$\sigma_z/2G=2A\lambda^2 \cos \lambda x(\cosh^2 \lambda h+(h\lambda)^2)/\lambda h \cosh \lambda h.$$

This shows that if a pressure $q_0 \cos \lambda x$ acts at the surface of the ground, a pressure

$$q=(\cosh \lambda h+\lambda h \sinh \lambda)/(\cosh^2 \lambda h+(\lambda h)^2)$$

is acting at the surface of the rock.

Using the Fourier integral as in the previous cases, we find the pressure distribution p at the surface of the rock due to a concentrated load P acting at the surface of the ground.

$$p(x)=\frac{P}{\pi h}\int_0^\infty \frac{\cosh \alpha+\alpha \sinh \alpha}{\cosh^2 \alpha+\alpha^2} \cos \alpha \frac{x}{h} d\alpha.$$

This formula coincides with Marguerre's result for the case $\nu=\frac{1}{2}$.[3]

Case (d)

The soft ground is here supposed to be infinitely deep and to contain at the depth h an inextensible but perfectly flexible thin layer to which the soft ground sticks perfectly so that only vertical motion at that depth is permissible.

We take the x axis at depth h on the inextensible layer and the z axis positive downward, and a sinusoidal solution in x as in case (c). The only difference with the preceding case is the boundary condition (12). The vertical displacement w at $z=0$ is not zero, but is related to the normal stress on that layer. To find this relation,

[2] L. N. G. Filon, Phil. Trans. Roy. Soc. London, 1903; E. Melan, Beton und Eisen 18 (1919).

[3] Marguerre, "Druckverteilung durch eine elastische Schicht auf starrer rauher Unterlage," Ing. Archiv **2** (1931).

let us consider a sinusoidal solution applying to the infinitely deep material located below that layer. This is a case analogous to case (a). Since the material is infinitely deep, we must have $A=C=0$ and the horizontal displacement u deduced from formula (2) with $\nu=\frac{1}{2}$ is found to be

$$u=\lambda \sin \lambda x[Be^{-\lambda z}+zDe^{-\lambda z}].$$

The condition that the horizontal displacement be zero on the inextensible layer ($z=0$) is $B=0$.

The vertical displacement at $z=0$ is

$$w=De^{-\lambda z}(1+\lambda z)\cos \lambda x$$

and the normal stress

$$\sigma_z/2G=-D\lambda e^{-\lambda z}(1+\lambda z)\cos \lambda x.$$

The relation between w and σ_z at the surface of the inextensible layer is

$$\sigma_z/2G=-\lambda w.$$

The boundary conditions for the upper soft ground are then

(a) $u=0$ at $z=0$,

(b) $\sigma_z/2G=-\lambda w$, $z=0$,

(c) $\tau_{xz}=0$, $z=-h$.

As in case (c) we may write the relation (13) and introduce these boundary conditions to find the value of $B\ C\ D$ in terms of A.

The value of the normal stress σ_z at the rock surface $z=0$ is found to be

$$\frac{\sigma_z}{2G}=2\lambda^2 A\frac{\cosh \lambda h+\lambda h \sinh \lambda h}{h\lambda e^{h\lambda}}\cdot\cos \lambda x$$

and the value of σ_z at the ground surface is

$$\frac{\sigma_z}{2G}=\frac{2\lambda^2 A}{h\lambda}[h\lambda(h\lambda \cosh h\lambda-h\lambda \sinh h\lambda-\cosh h\lambda)+\cosh h\lambda+h\lambda \sinh h\lambda].$$

From this we conclude that a pressure distribution $q_0 \cos \lambda x$ at the ground surface transmits a pressure on the inextensible layer

$$q=\frac{e^{-h\lambda}}{1+h\lambda[h\lambda/(1+h\lambda \tanh h\lambda)-1]}.$$

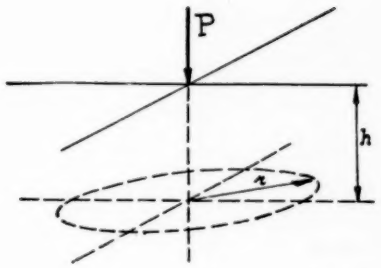

FIG. 4.

By using the Fourier integral as in the previous cases, we find the pressure distribution p transmitted to the inextensible layer when the surface carries a concentrated load P

$$p=\frac{P}{\pi h}\int_0^\infty \frac{e^{-\alpha}}{1-\alpha[1-\alpha/(1+\alpha \tanh \alpha)]}\cos \alpha\frac{x}{h}d\alpha.$$

THE THREE-DIMENSIONAL PROBLEM

The same cases (a) (b) (c) (d) are investigated if the load P is not concentrated on an infinite straight line but concentrated on a point, (Fig. 4). The stress distribution must then be axial-symmetrical around the load. Solutions of the problem may be found by using axial-symmetrical potential functions with cylindrical coordinates r, z.

$$\phi_0=(Ae^{\lambda z}+Be^{-\lambda z})J_0(\lambda r),$$

$$\phi_z=(Ce^{\lambda z}+De^{-\lambda z})J_0(\lambda r),$$

$$\phi_y=0,\quad \phi_x=0.$$

We have a vertical displacement w and a radial displacement u. Eqs. (2) and (3) become

$$u=-(\partial/\partial r)[\phi_0+z\phi_z],$$

$$w=-(\partial/\partial z)[\phi_0+z\phi_z]+4(1-\nu)\phi_z.$$

If we call τ the horizontal shear acting in the radial direction, we have equations entirely similar to Eqs. (4), (4_1).

$$\sigma_z/2G=\partial w/\partial z+\nu\Theta/(1-2\nu),$$

$$\tau/G=\partial w/\partial r+\partial u/\partial z.$$

As before, we shall assume that $\nu=\frac{1}{2}$. These equations show that the problem of determining

the constants $A\ B\ C\ D$ is the same as in the two-dimensional case. For instance, if in the two-dimensional case to a load distribution at the surface $q_0 \cos \lambda x$ corresponded a pressure at depth h

$$q = g(\lambda h) q_0 \cos \lambda x$$

we may conclude that in the corresponding three-dimensional case to a load distribution $q_0 J_0(\lambda r)$ at the surface corresponds a pressure at depth h

$$q = g(\lambda h) q_0 J_0(\lambda r)$$

and we do not have to repeat the above calculations to find the function $g(\lambda h)$.

Case (a)

The case of a concentrated load P acting on an infinitely deep ground is found from the distribution $q_0 J_0(\lambda r)$. At a depth h the vertical pressure p transmitted is found by using the solution of the two-dimensional problem $g(h\lambda) = e^{-\lambda h}(1+h\lambda)$

$$p = e^{-h\lambda}(1+h\lambda) q_0 J_0(\lambda r).$$

An arbitrary load $q(r)$ could be represented by using the identity

$$q(r) = \int_0^\infty d\lambda \int_0^\infty J_0(\lambda\rho) J_0(\lambda r) q(\rho) \lambda \rho d\rho.$$

This shows that the corresponding pressure distribution at depth h is

$$p(r) = \int_0^\infty e^{-\lambda h}(1+\lambda h) J_0(\lambda r) \lambda d\lambda \int_0^\infty J_0(\lambda\rho) q(\rho) \rho d\rho.$$

If the load is concentrated at the origin on a circle of radius ϵ

$$P = 2\pi \int_0^\epsilon q(\rho) \rho d\rho.$$

The corresponding pressure distribution at depth h is

$$p(r) = (P/2\pi) \int_0^\infty \lambda e^{-\lambda h}(1+\lambda h) J_0(\lambda r) d\lambda$$

or

$$p(r) = (P/2\pi h^2) \int_0^\infty \alpha e^{-\alpha}(1+\alpha) J_0(\alpha r/h) d\alpha.$$

The same method may be used for all other cases (b), (c), (d). We find:

Case (b)

$$p(r) = \frac{P}{2\pi h^2} \int_0^\infty 2\alpha \frac{\alpha \cosh \alpha + \sinh \alpha}{\sinh 2\alpha + 2\alpha} J_0\left(\alpha \frac{r}{h}\right) d\alpha.$$

Case (c)

$$p(r) = \frac{P}{2\pi h^2} \int_0^\infty \alpha \frac{\cosh \alpha + \alpha \sinh \alpha}{\cosh^2 \alpha + \alpha^2} J_0\left(\alpha \frac{r}{h}\right) d\alpha.$$

Case (d)

$$p(r) = \frac{P}{2\pi h^2} \int_0^\infty \alpha \frac{e^{-\alpha}}{1 - \alpha[1 - \alpha/(1+\alpha \tanh a)]} \times J_0\left(\alpha \frac{r}{h}\right) d\alpha.$$

Numerical Evaluation of the Infinite Integrals

The problem reduces to the evaluation of either

$$(P/\pi h) \int_0^\infty g(\alpha) \cos(\alpha x/h) d\alpha$$

for the two-dimensional problem, or

$$(P/2\pi h^2) \int_0^\infty \alpha g(\alpha) J_0(\alpha r/h) d\alpha$$

in the three-dimensional problem. The function $g(\alpha)$ has the form

$$g(\alpha) = (1+\alpha) e^{-\alpha} \qquad \text{case (a)},$$

$$g(\alpha) = 2 \frac{\alpha \cosh \alpha + \sinh \alpha}{\sinh 2\alpha + 2\alpha} \qquad \text{case (b)},$$

$$g(\alpha) = \frac{\cosh \alpha + \alpha \sinh \alpha}{\cosh^2 \alpha + \alpha^2} \qquad \text{case (c)},$$

$$g(\alpha) = \frac{e^{-\alpha}}{1 - \alpha[1 - \alpha/(1+\alpha \tanh \alpha)]} \qquad \text{case (d)}.$$

We start from the two identities

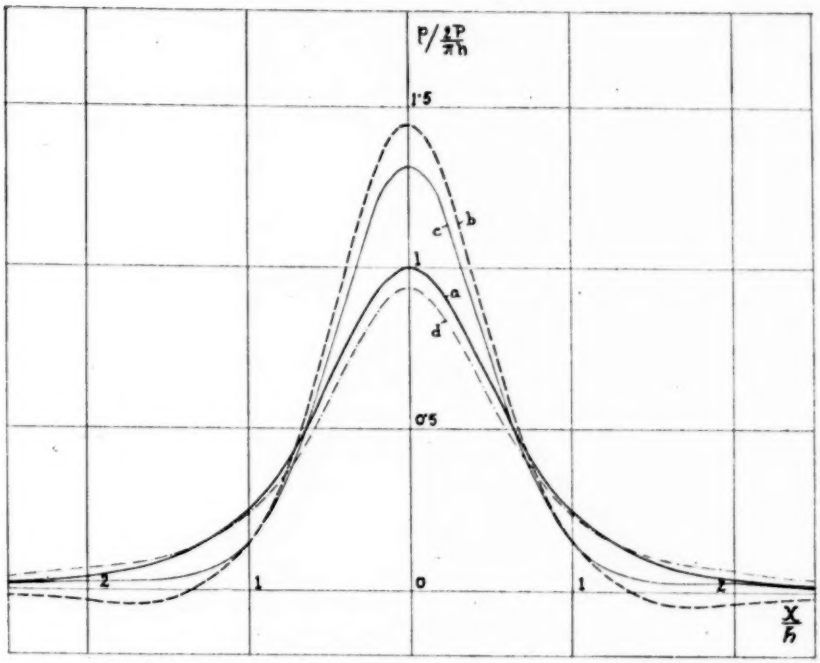

FIG. 5. Pressure distribution $p/(2P/\pi h)$ in the two-dimensional problem.

Case (a) ——— Boussinesq distribution. Maximum value of pressure $p = 2P/\pi h$.
Case (b) — — — Slippery rigid bed. Maximum value of pressure $p = 1.441 \cdot 2P/\pi h$.
Case (c) ——— Rough rigid bed. Maximum value of pressure $p = 1.291 \cdot 2P/\pi h$.
Case (d) —·—·— Inextensible flexible layer. Maximum value of pressure $p = 0.935 \cdot 2P/\pi h$.

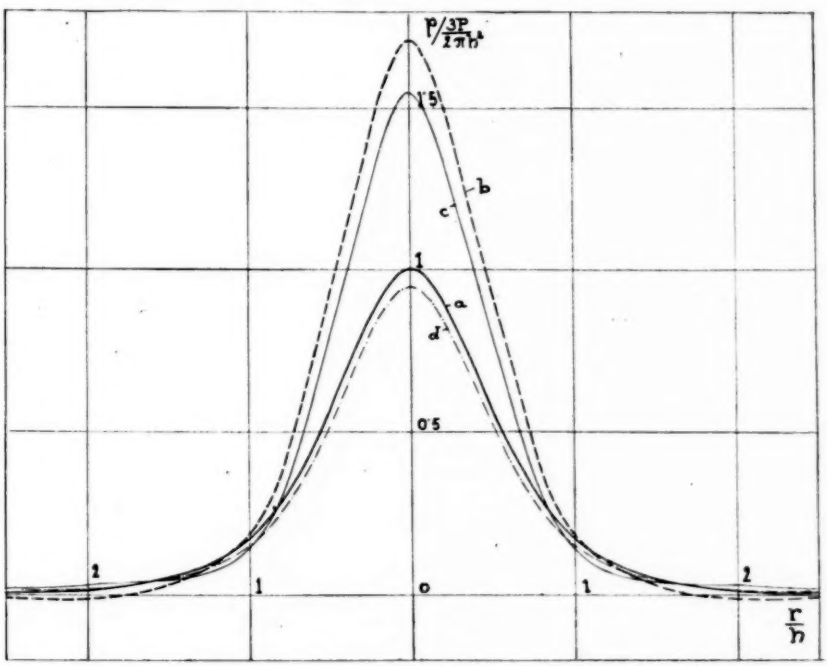

FIG. 6. Pressure distribution $p/(3P/2\pi h^2)$ in the three-dimensional problem.

Case (a) ——— Boussinesq distribution. Maximum value of pressure $p = 3P/2\pi h^2$.
Case (b) — — — Slippery rigid bed. Maximum value of pressure $p = 1.711 \cdot 3P/2\pi h^2$.
Case (c) ——— Rough rigid bed. Maximum value of pressure $p = 1.557 \cdot 3P/2\pi h^2$.
Case (d) —·—·— Inextensible flexible layer. Maximum value of pressure $p = 0.942 \cdot 3P/2\pi h^2$.

$$\int_0^\infty e^{-ax}\cos bx dx = a/(a^2+b^2),$$

$$\int_0^\infty e^{-ax}J_0(bx)dx = (a^2+b^2)^{-\frac{1}{2}}.$$

Taking the derivatives with respect to a, we get

$$\int_0^\infty x^n e^{-ax}\cos bx dx = (-1)^n \frac{d^n}{da^n}\left(\frac{a}{a^2+b^2}\right),$$

$$\int_0^\infty x^n e^{-ax}J_0(bx)dx = (-1)^n \frac{d^n}{da^n}\left(\frac{1}{(a^2+b^2)^{\frac{1}{2}}}\right).$$

This shows that the integrals would be evaluated readily if the functions $g(\alpha)$ where all expressed as a sum of terms of the type $\alpha^n e^{-k\alpha}$, where n is an integer.

Case (a)

In case (a) there is no difficulty in expressing these integrals. For the two-dimensional problem we get

$$p(x) = (P/\pi h)\int_0^\infty (1+\alpha)e^{-\alpha}\cos(\alpha x/h)d\alpha,$$

$$p(x) = (2P/\pi h)(1+x^2/h^2)^{-2}.$$

For the three-dimensional problem

$$p(r) = (P/2\pi h^2)\int_0^\infty \alpha(1+\alpha)e^{-\alpha}J_0(\alpha r/h)d\alpha,$$

$$p(r) = (3P/2\pi h^2)[1+(r/h)^2]^{-5/2}.$$

These are both the well-known Boussinesq solutions.

The two-dimensional distribution

$$p(x)/(2P/\pi h) = (1+x^2/h^2)^{-2}$$

is represented by curve (a) in Fig. 5 and the three-dimensional distribution $p(r)/(3P/2\pi h^2)$ by curve (a) in Fig. 6.

Case (b)

The function $g(\alpha)$ may be represented with an error smaller than 1 percent by

$$(2\alpha\cosh\alpha+\sinh\alpha)/(\sinh 2\alpha+2\alpha) = 2(1+\alpha)e^{-\alpha}-(1+2\alpha)e^{-2\alpha}-5.1\alpha^3e^{-4\alpha}.$$

The pressure distribution for the two-dimensional case is

$$p(x) = \frac{2P}{\pi h}\left[\frac{2}{(1+x^2/h^2)^2}-\frac{0.5}{(1+(x/2h)^2]^2}-0.059\frac{1-6(x/4h)^2+(x/4h)^4}{[1+(x/4h)^2]^4}\right].$$

The dimensionless quantity $p(x)/(2P/\pi h)$ is plotted in Fig. 5 by curve (b).

For the three-dimensional case we have

$$p(r) = \frac{3P}{2\pi h^2}\left[\frac{2}{[1+(r/h)^2]^{5/2}}-\frac{0.25}{[1+(r/2h)^2]^{5/2}}-0.039\frac{1-3(r/4h)^2+\frac{3}{8}(r/4h)^4}{[1+(r/4h)^2]^{9/2}}\right].$$

The ratio $p(r)/(3P/2\pi h^2)$ is represented in Fig. 6 by curve (b).

Case (c)

The function $g(\alpha)$ may be represented with an error smaller than 1 percent by

$$(\cosh\alpha+\alpha\sinh\alpha)/(\cosh^2\alpha+\alpha^2) = (2\alpha\cosh\alpha+\sinh\alpha)/(\sinh 2\alpha+2\alpha)-2.80\alpha^4e^{-3\alpha}-56\alpha^4e^{-8.8\alpha}.$$

The pressure distribution in the two-dimensional case is

$$p(x) = \frac{2P}{\pi h}\left[\frac{2}{[1+x^2/h^2]^2}-\frac{0.5}{[1+(x/2h)^2]^2}-0.059\frac{1-6(x/4h)^2+(x/4h)^4}{[1+(x/4h)^2]^4}-0.138\frac{1-10(x/3h)^2+5(x/3h)^4}{[1+(x/3h)^2]^5}\right.$$
$$\left.-0.012\frac{1-10(x/8.8h)^2+5(x/8.8h)^4}{[1+(x/8.8h)^2]^5}\right].$$

The ratio $p(x)/(2P/\pi h)$ is represented in Fig. 5 by curve (c). The pressure distribution in the three-dimensional case is

$$p(r)=\frac{3P}{2\pi h^2}\left[\frac{2}{[1+(r/h)^2]^{5/2}}-\frac{0.25}{[1+(r/2h)^2]^{5/2}}-0.039\frac{1-3(r/4h)^2+\frac{3}{8}(r/4h)^4}{[1+(r/4h)^2]^{9/2}}\right.$$
$$\left.-0.154\frac{1-5(x/3h)^2+(15/8)(x/3h)^4}{[1+(x/3h)^2]^{11/2}}\right].$$

The ratio $p(r)/(3P/2\pi h^2)$ is represented in Fig. 6, by curve (c).

Case (d)

The function $g(\alpha)$ may be represented with an error less than 1 percent as follows:

$$e^{-\alpha}/\{1-\alpha[1-\alpha/(1+\alpha\tanh\alpha)]\}=(1+\alpha)e^{-\alpha}-1.77\alpha^3e^{-3\alpha}.$$

The pressure distribution in the two-dimensional problem is

$$p(x)=\frac{2P}{\pi h}\left[\frac{1}{(1+x^2/h^2)^2}-0.065\frac{1-6(x/3h)^2+(x/3h)^4}{[1+(x/3h)^3]^4}\right].$$

The ratio $p(x)/(2P/\pi h)$ is represented in Fig. 5 by curve (d).

The pressure distribution in the three-dimensional problem is

$$p(r)=\frac{3P}{2\pi h^2}\left[\frac{1}{(1+r^2/h^2)^{5/2}}-0.058\frac{1-3(r/3h)^2+\frac{3}{8}(r/3h)^4}{[1+(r/3h)^2]^{9/2}}\right].$$

The ratio $p(r)/(3P/2\pi h^2)$ is represented in Fig. 6 by curve (d).

Magnetic Properties and Orientation of Ferromagnetic Particles
II. Pyrrhotite[1]

C. W. DAVIS,[2] *U. S. Bureau of Mines, Pittsburgh, Pennsylvania*

(Received June 21, 1935)

The effect of heat treatment and of particle orientation on the magnetic properties of granular pyrrhotite are discussed and illustrated by curves and data. Heat treatment which causes little or no chemical change alters pyrrhotite so that increased induction and remanence and decreased coercive force result. Particles aligned in a field parallel to that used in their magnetic measurement showed greater induction and remanence but less coercive force than randomly oriented material, while cross-oriented particles showed the lowest induction and remanence but the greatest coercive force.

INTRODUCTION

A CONSIDERATION of recent observations on the effect of orientation on the measured magnetic properties of natural and of heat treated pyrrhotite shows that although the action with respect to coercive force is different from that of magnetites it is nevertheless susceptible to the same explanation that has been given for the behavior of the latter mineral.[3]

EXPERIMENTAL

A massive specimen of magnetic, auriferous pyrrhotite from Haywood County, North Carolina, was crushed to pass a 100-mesh screen and was purified by repeated alternating and unidirectional field magnetic separation. The purified sample was magnetically measured and was then heat treated at 250°C for 40 minutes to increase its magnetic induction so as to form a product better suited to measurement in our apparatus.

The magnetic measurements were conducted as described in the previous article except that very small steps were used in the determination of coercive force and, further, that the sample was demagnetized by the recently described method in which a switch surrounded by a condenser is broken in such a way that a maximum magnetic field inside a solenoid is reduced to zero by a damped oscillatory discharge.[4]

Particle orientation was performed as before except that cross-oriented samples were prepared by agitating and rotating the sample capsule with its axis perpendicular to the direction of the field after each fractional addition of the sample was made. All results have been calculated to a packing density of 2.36 grams per cubic centimeter.

DISCUSSION OF RESULTS

The results show that there are certain characteristic differences between the effect of orientation on the measured magnetic properties of magnetite and those of pyrrhotite. This is in line with the difference in magnetic structure that has been attributed to the minerals by Weiss and his co-workers.[5]

They studied magnetic properties of thin plates cut in various crystallographic directions from crystals of magnetite and pyrrhotite and concluded that a few magnetite crystals approached magnetic isotropism at field strengths of 400 oersteds or more but that most specimens had no greater symmetry than that of the rhombic system. They distinguished between two types of pyrrhotites: The normal, exemplified by crystals from Morro-Velho, Brazil, with a magnetic plane in which magnetization takes place more easily than in a direction perpendicular to it; and the more common abnormal type in which the magnetic properties are poorly defined. They reported further that normal

[1] Published by permission of the Director, U. S. Bureau of Mines. (Not subject to copyright.)
[2] Metallurgical division, U. S. Bureau of Mines.
[3] C. W. Davis, Physics **6**, 96 (1935).
[4] C. W. Davis, Physics **6**, 184 (1935).
[5] P. Weiss, J. de physique **4**, 469 (1905). P. Weiss and J. Kunz, J. de physique **4**, 847 (1905). Max Ziegler, *Magnetic Properties of Pyrrhotite Crystals*, Diss. (Zürich, 1915). V. Quittner, Ann. d. Physik **30**, 289 (1909).

TABLE I. *Analyses of natural and heat treated pyrrhotite.*

SAMPLE DESCRIPTION	ANALYSES, PERCENT Fe	S	NOT DETERMINED	MOLECULAR RATIO Fe	S
Natural, 100 mesh	56.97	36.75	6.28	10	11.23
Heat treated, 100 mesh	57.09	36.05	6.86	10	11.00
Heat treated, 325 mesh	56.95	36.47	6.58	10	11.15

pyrrhotite may require a field of 13,400 oersteds for magnetic saturation.

The heat treatment used to augment the magnetic properties of the North Carolina pyrrhotite caused superficial oxidation, as evidenced by a resultant blue coloration, but produced little chemical alteration, as is shown by the analyses in Table I. The ratio of iron to sulphur corresponds approximately to $Fe_{10}S_{11}$, which falls within the composition range usually allotted to pyrrhotite.

Magnetic properties of minus 100-mesh natural and heat treated samples are given in Figs. 1 and 2. Fig. 1 shows that heating has raised the intensity of magnetization at $H=3340$ from the 138 and 167 gauss of the random and oriented samples of natural mineral to the 286 and 353 gauss of the random and oriented samples of the heat treated material. Fig. 2 shows that a similar change in remanent magnetization has resulted from heating, the increase ranging from 79 to 123 gauss for the random and from 82 to 158 gauss for the oriented samples. The coercive forces, however, have undergone a reversal; the highest coercive force, 210 oersteds, is exhibited by the natural random sample, followed in order by natural oriented with 200 oersteds, heat treated random with 170, and, lowest, heat treated oriented with 135 oersteds (see Fig. 2).

Since the change in chemical composition has been so slight, it would seem that heating must have affected the physical constitution, as discussed by Michel and Chaudron,[6] so that more perfect alignment of magnetic domains is possible. The decrease of coercive force suggests possible crystal growth on heating, inasmuch as Gottschalk[7] has shown that there is a direct linear relation between coercive force and specific surface.

Other tests showed that minus 325-mesh heat treated pyrrhotite gave results well suited for measurement with our equipment and different only in degree—not in kind—from results obtained with natural and with heat treated pyrrhotite samples of other particle size.

Fig. 3 shows that for heat treated minus 325-mesh pyrrhotite the magnetization ($4\pi I$) up to field strengths of 3340 oersteds is highest (404 gauss) for particle orientation parallel to the field, lower (292 gauss) for random orientation, and lowest (266 gauss) for samples cross-oriented during capsule rotation. This 28 percent

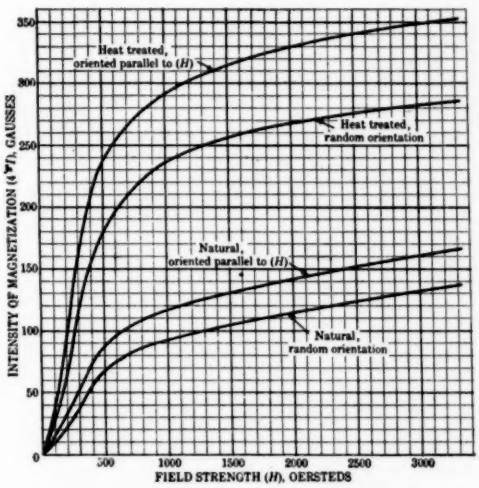

FIG. 1. Magnetization curves for 100-mesh natural and heat treated pyrrhotite, different orientations.

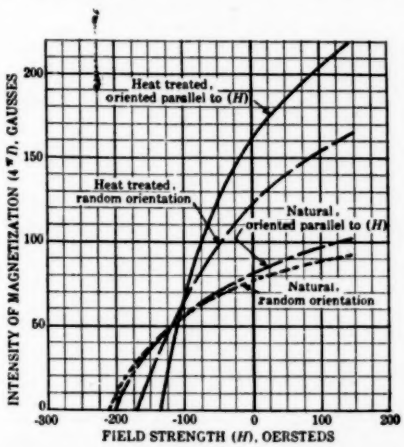

FIG. 2. Hysteresis curves, upper branch near origin, for 100-mesh natural and heat treated pyrrhotite, different orientations.

[6] A. Michel and G. Chaudron, Comptes rendus **198**, 1913 (1934).

[7] V. H. Gottschalk, "The Coercive Force of Magnetite Powders." Report of Investigations 3268, U. S. Bureau of Mines, p. 83 (1935); Physics **6**, 127 (1935).

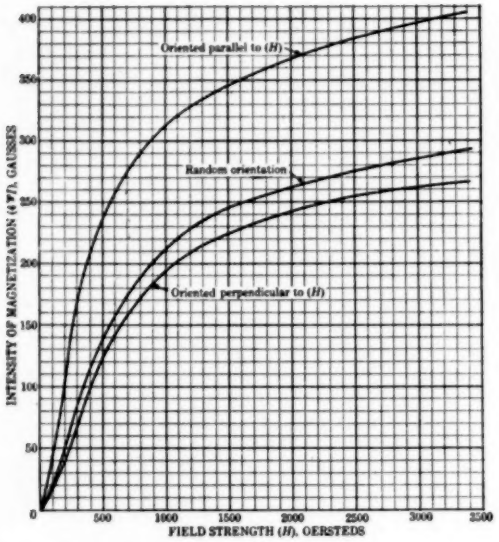

FIG. 3. Magnetization curves for 325-mesh heat treated pyrrhotite, different orientations.

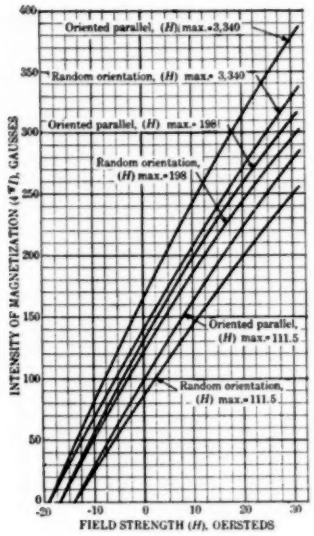
Oriented parallel, (H) max.=3,340
Random orientation, (H) max.= 3,340
Oriented parallel, (H) max.=198
Random orientation, (H) max.=198
Oriented parallel, (H) max.=111.5
Random orientation, (H) max.=111.5
INTENSITY OF MAGNETIZATION (4πI), GAUSSES
FIELD STRENGTH (H), OERSTEDS

FIG. 4. Hysteresis curves, upper branch near origin, for 325-mesh heat treated pyrrhotite, different orientations.

maximum difference in magnetization between the two first cases given above as contrasted with a zero difference at the same field strength in the case of the magnetites reported in a previous paper is matched by the magnetites when a comparison of their magnetization is made at a similar condition of unsaturation, a difference of 27.5 percent in their magnetization being obtained between oriented and random samples at a field strength of 42 oersteds.

As the results for pyrrhotite are given for measurements made at about one-fourth the reported saturation value, it is very probable that in fields of about 13,400 oersteds the effect of orientation on the magnetic induction of pyrrhotite might disappear.

Although the curves shown in Fig. 4 cannot represent absolute hysteresis values since saturation was not attained, the remanence as measured doubtless shows the same relationship between different orientations that would obtain if absolute values were available; at any rate, the remanent magnetization differences follow the same general trend as shown by true hysteresis loops of magnetite samples. The same sample of pyrrhotite showed measured remanent magnetization ($4\pi I$) as follows: Oriented parallel to the field, 208 gauss; oriented random, 136 gauss; and cross-oriented, 126 gauss.

The coercive forces determined from the data used in the construction of the curves in Fig. 4 are also subject to the unfortunate limitation of our measuring equipment with a maximum field strength of 3340 oersteds. The measured value for the sample of pyrrhotite oriented parallel to the field is lowest, 152 oersteds; the random sample is next, 220 oersteds; and the cross-oriented sample highest, 237 oersteds.

These results, which are strikingly different from those obtained with magnetites in which the coercive force was independent of particle orientation, suggested that the coercive forces of random and oriented samples of magnetite as determined at about one-fourth saturation might exhibit a similar difference. Results for different degrees of saturation of magnetite obtained by determinations using many small steps in the region where the hysteresis curves cut the axes are shown in Fig. 5.

The coercive force increases with the degree of magnetic saturation, as would be expected—14 oersteds at $H_{max.}=111.5$, 17.5 oersteds at $H_{max.}=198$, and 19 oersteds at $H_{max.}=3340$. Coercive force, however, is independent of particle orientation in all cases.

The main difference between the action for magnetite and that for pyrrhotite is apparently associated with a greater lag in demagnetization inherent in those particles of the latter mineral oriented other than parallel to the field. The

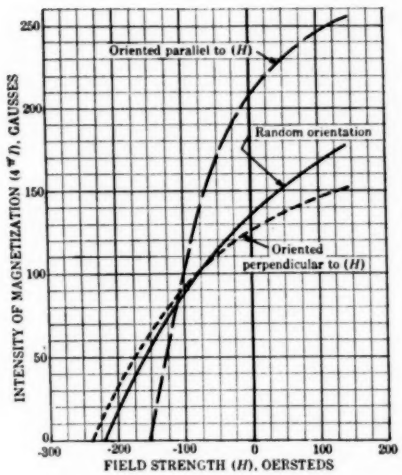

FIG. 5. Hysteresis curves, upper branch near origin, for −65+250 magnetite, different maximum magnetizations.

position of easiest magnetization is also the position of easiest demagnetization for both minerals.

The results for pyrrhotite are in even more perfect accord than those for magnetite with the postulations of Sizoo[8] on the magnetic properties of single crystals in which he predicted that crystal orientation would affect all three properties—induction, remanence, and coercive force.

The results given in this paper conform to the modified Weber domain theory discussed in a previous paper of this series. The difference in action of orientation on the coercive force of magnetite and of pyrrhotite suggests that the study of other samples of these minerals, especially that of normal pyrrhotite from Morro-Velho, Brazil, might prove very instructive.

ACKNOWLEDGMENT

I am very grateful to Dr. V. H. Gottschalk and to Mr. Max Hartenheim for magnetic determinations and to Mr. E. L. Curran for chemical analyses used in this work.

[8] G. J. Sizoo, Physica **10**, 1 (1930).

Space Charge in Liquid Dielectrics

J. B. WHITEHEAD AND E. E. MINOR, *Department of Electrical Engineering, The Johns Hopkins University*

(Received August 15, 1935)

Studies were made of the unequal potential distribution commonly observed in insulating liquids under continuous potential difference. The potential distribution between parallel plates is measured in two insulating oils for over-all voltages between 500 and 1500 volts, and at temperatures between 20 and 60°C. This distribution is produced by an accumulation of space charge near the electrodes which accumulation, however, extends measurably into the volume of the liquid. The amount of space charge as computed from the potential distribution increases with increase of applied voltage and decreases with increase in temperature. On reversal of the applied voltage, the initial over-all conductivity is of approximately the same value as that preceding reversal. The initial current on reversal may remain constant over an appreciable interval, say from 1 to 4 sec. Following the initial constant value, the reverse current rises sharply to a maximum from 2 to 6 times the initial constant value, and at first rapidly and then slowly decreases to the same long-time values as that of the preceding opposite potential. In this condition, a reversal of the foregoing pattern of potential distribution takes place.

It is suggested that two types of ion are involved in the space charge, one of high mobility, and the other of low mobility, due to the accumulation about it of an aggregate of neutral molecules. Oscillographic studies of the variation of current on reversal offer means for approximate computations of the mobility of the ions involved. The mobility of the ions in a given liquid may take a wide range of values. As between different oils and for the same oil at different temperatures, mobilities vary inversely as the viscosity. In a low viscosity insulating oil a high value of 10^{-4} cm/sec./volt/cm has been observed at 22°C.

INTRODUCTION

IN a recent paper Whitehead and Marvin[1] have studied the nonlinear potential distribution between the two parallel plate electrodes of a condenser having insulating oil as dielectric. They attribute the phenomenon to the accumulation of space charges in the volume of the oil near the electrodes. They further showed that if the voltage applied to the condenser is suddenly reversed, the reverse current passes through a pronounced maximum as the original potential pattern is built up in the opposite sense. From the dimensions of the condenser and the time required for the reversal of the potential pattern, they estimated that the mobility of the ions involved was of the order of 10^{-4} cm/sec./volt/cm. Herzfeld,[2,3] using the Whitehead-Marvin curves and the ionization theory of gases as extended to liquids, arrives at the figure 10^{-6} for the mobility. Two different types of ion or perhaps a wide range of type are thereby suggested. Schumann,[4] since the above work, has studied analytically the current variations to be expected in the charge and discharge currents of condensers due to the motions of layers of space charge in the liquid dielectric, and concludes that the maxima of the type reported here are to be expected under certain conditions. This paper reports some further studies of the subject.

SCOPE OF THE WORK

Two high-grade insulating oils were examined with special reference to (1) the distribution and the variation with time, following the initial application of voltage, of the potential gradient within the dielectric; (2) the magnitudes of the space charges involved; (3) the relation between the current and the potential variations following the abrupt reversal of applied voltage; (4) the mobilities of the ions involved, with special reference to the reverse current maximum.

Commercial insulating oils were used. Oil (A) was a clear, highly refined insulating oil, viscosity 0.23 poise at 25°C, average 30-minute conductivity 5×10^{-15} mhos/cm³. Oil (B) was somewhat less highly refined, viscosity 15.0 poises at 25°C, average 30-minute conductivity 6×10^{-14} mhos/cm³. The oils were received in sealed containers and were placed in the test cell without further treatment. Several other materials, principally waxes, were tested with reference to potential distribution only. The

[1] J. B. Whitehead and R. H. Marvin, Trans. A. I. E. E. 49, 647 (1930).
[2] K. F. Herzfeld, Phys. Rev. 37, 287 (1931).
[3] K. F. Herzfeld, Phys. Rev. 34, 791 (1929).
[4] W. O. Schumann, Arch. Elek. (27), p. 241 (1933).

results on only one of these, a commercial paraffin, are reported. Its melting point was approximately 54°C, conductivity at 68°C, 2.6×10^{-11} mhos/cm³.

The principal quantities measured were: current *vs.* time, potential *vs.* time, and distribution of potential gradient in the final steady state. The same observations were made for an abrupt reversal of voltage following a foregoing steady state. The observations were made at each of three voltages, 500, 1000, and 1500 volts, and over the temperature range 20°C to 45°C.

Experimental Method

The variation of the current over the first few seconds following the application or reversal of voltage was observed with an Einthoven[5] string galvanometer and rotating photographic film, operated in conjunction with a rapid charging, short-circuiting, discharging, and reversing switch, as described by Whitehead and Marvin.[6] The arrangement provides for a brief instant of short circuit of the condenser before the application of reverse voltage, for the removal of the geometric charge on the plates. For the values of the current at time intervals greater than one minute, a sensitive D'Arsonval galvanometer was used.

The oil to be tested was placed in a carefully cleaned open container into which were immersed a pair of parallel brass plates, each 311 sq. cm in area, and each completely surrounded in its own plane by a guard ring 3.7 cm wide. The back of each plate and the measuring electrodes were completely shielded. The insulation was equipped with guards maintaining leakage at a negligible level at all exposed points. The plate separation was variable up to a maximum of 1.90 cm.

The potential in any given plane in the oil between the electrodes was measured with a test electrode or probe. The probe potential was determined by a sensitive[1] zero method which avoided the passage of any charging current from the probe to the detecting gold leaf electroscope. The test probe was a thin metallic rectangular frame 6.3 cm² wound zigzag with 0.005 in. Therlo wire forming a grating of wide mesh. It was supported from a carriage moving in a slot attached to the electrode super-structure. The position of the probe was read with a micrometer screw. The test cell was surrounded by an oil bath, the temperature of which was maintained constant by means of immersed electric heaters and thermostatic control. Provision was also made for low temperature studies using carbon dioxide snow. The entire equipment including test cell and temperature bath was placed in a heat insulating container.

Results of Experiments

Potential gradient

In Figs. 1, 2, and 3, curves (a) indicate the characteristic variation with time of the potential at a given point in the oil following the first application of voltage. Plate separation 1.9 cm, temperature 23°C, voltage 500, 1000, and 1500 volts. These curves show that at the instant of application of voltage, the potential at any point in the dielectric is that corresponding to a uni-

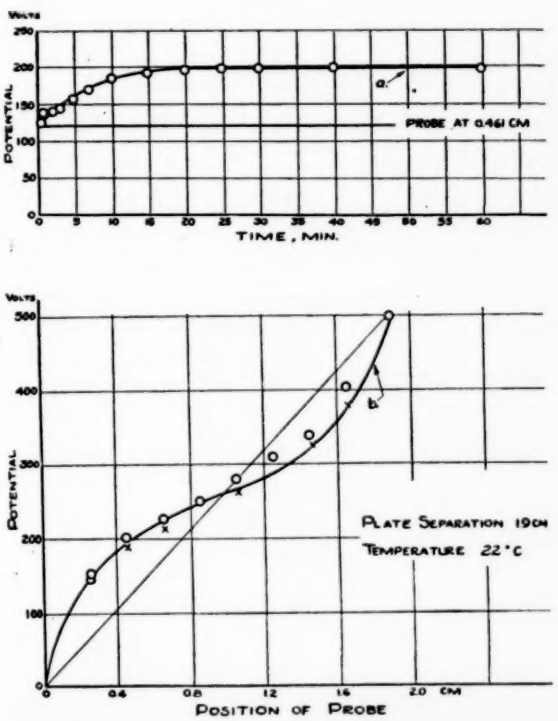

FIG. 1. Potential time curves and potential distribution for 500 volts applied to oil (A).

[5] W. Einthoven, Ann. d. Physik **12**, 1054 (1903).
[6] J. B. Whitehead and R. H. Marvin, Trans. A. I. E. E. **48**, 299 (1929).

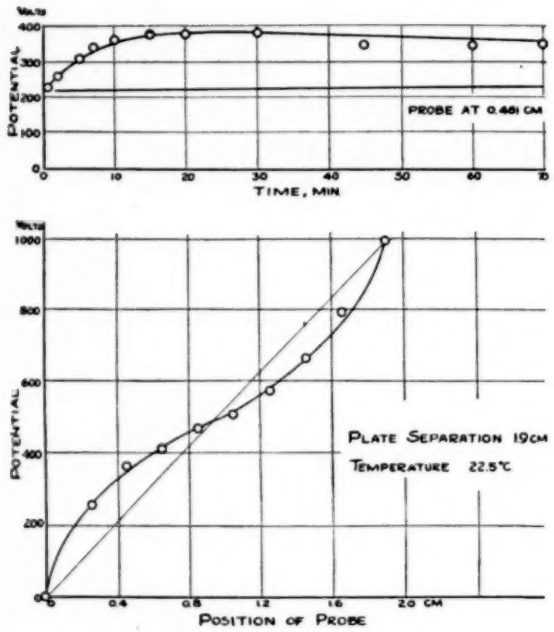

FIG. 2. Potential time curves and potential distribution for 1000 volts applied to oil (A).

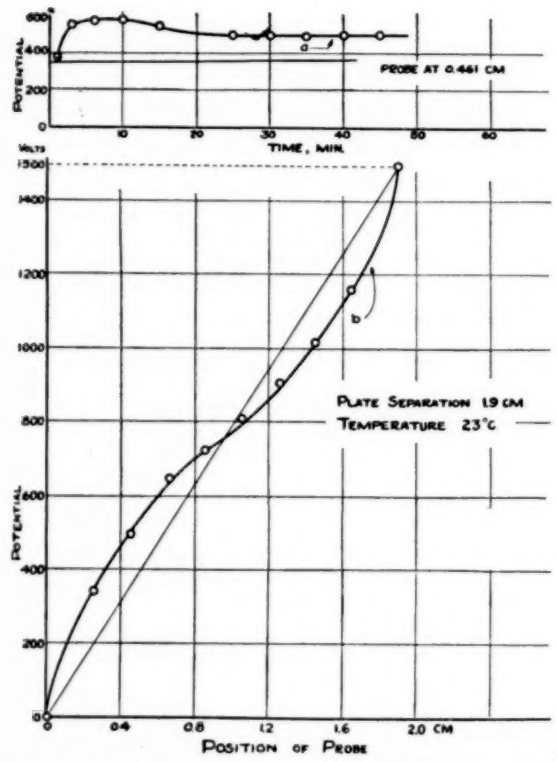

FIG. 3. Potential time curves and potential distribution for 1500 volts applied to oil (A).

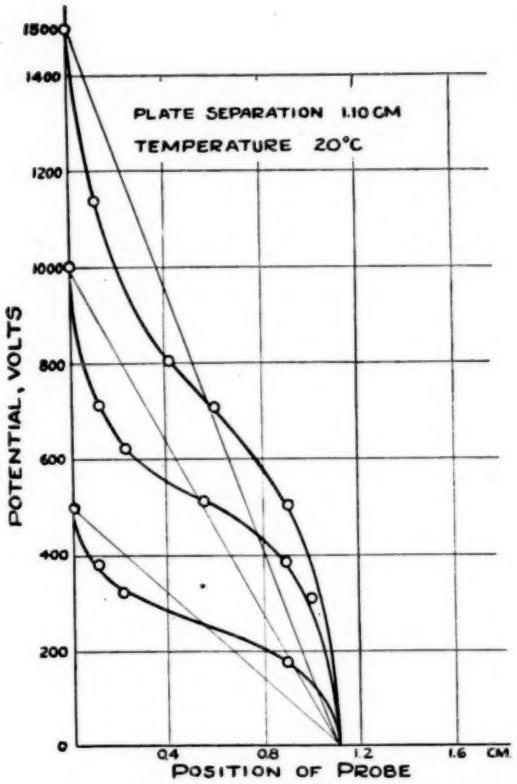

FIG. 4. Potential distribution for 500, 1000 and 1500 volts applied to oil (B).

form gradient between electrodes. The potential then rises (or falls) rapidly from this value and arrives at a steady value only after a period of twenty minutes or more. The shape of these curves and the time intervals involved suggest an accumulation of charges of opposite sign in the neighborhood of each electrode, that the process takes place slowly, and that very sluggish ions of low mobility are involved.

Curves (b) of Figs. 1, 2, and 3 show the final potential distribution in the steady state for each of three values of applied voltage. The curves of Fig. 4 show the potential distribution for oil B. The curves indicate a symmetrical variation about the central plane with relatively high values of gradient in the neighborhood of the electrodes. This electrode gradient is greater the higher the applied voltage. Obviously the gradient at the center of the dielectric is correspondingly less than the initial uniform value. The shapes of these curves also suggest volumetrically and symmetrically distributed space charges near the electrodes and with opposite signs.

Approximate values of potential gradients may be taken directly from the curves, and may be used for a computation of the total amount of space charge accumulating on either side of the central plane.

If F_a and F_b are the measured gradients, in electrostatic units, at one electrode, and in the center of the dielectric respectively, then by Poisson's equation, we have for the total space charge per cm² of plate area between plate and central plane of the dielectric:

$$q=\int_a^b \rho dx=\frac{K}{4\pi}(F_a-F_b) \text{ statcoulombs/sq. cm}$$

or, since F_a and F_b are measured in volts, then the charge expressed in coulombs is:

$$Q=\frac{K}{4\pi}(F_a-F^b)\left(\frac{1}{9\times10^{11}}\right)\frac{\text{coulombs}}{\text{sq. cm of plate}}.$$

Values as measured and computed in this way and corresponding to the data of Figs. 1, 2, and 3 are given in Table I. The values are subject to an error of ±25 percent because of the uncertainty in the evaluation of the potential gradient. The final values of the space charge are based on the mean of the values of the gradient at the two electrodes. It is seen that the total space charge is relatively small. However, it increases with the applied voltage, and, as the over-all average gradient is relatively low in these experiments, at higher values of gradient much greater values of the space charge are to be expected.

If in the steady state of the dielectric, the applied voltage is removed, the potential of the test probe falls more or less slowly. The rate of fall is lower the higher the applied voltage and the lower the temperature. The fall is more rapid if the geometric charge is removed by a brief instant of short circuit. This behavior is in general accord with the behavior indicated by the numerical data, and on the assumption that the space charges are made up of mobile ions.

TABLE I. *Space charge. Oils A and B.*

Specimen	Volts	Temp.	Gradient (volts/cm) Ave. F_a	F_b	Space Charge/cm² Coulombs	Statcoulombs
			Oil (A), Plate Separation 1.9 cm			
A	500	22°C	1000	130	1.55×10^{-10}	0.465
B	1000	22.5	1420	180	2.2×10^{-10}	.662
C	1500	23	3300	380	5.1×10^{-10}	1.55
D	1500	48	2675	510	4.0×10^{-10}	1.22
			Oil (B), Plate Separation 1.1 cm			
E	500	20	2450	180	3.8×10^{-10}	1.15
F	1000	20	4450	300	7.3×10^{-10}	2.21
G	1500	20	4475	550	7×10^{-10}	2.1

If in the steady state under applied voltage, the latter is removed, the electrodes are short-circuited for a brief instant, and then connected through a sensitive galvanometer, no current is observed. In other words, there is no discharge current corresponding to the slowly decaying charging current commonly observed. This type of behavior has been frequently noted. It indicates that the accumulation of space charges near the electrodes is in large measure restrained from recombination by corresponding bound charges on the electrodes. The slow return[7] to the neutral condition through diffusion and slow recombination is by a low value conduction current in the external circuit as the opposite space charges slowly diffuse together. These two are in opposite sense and their difference is so small as to be measured only with high sensitivity equipment.

The sign and volumetric distribution of the space charges was shown by freezing the oil while under stress, with carbon dioxide snow. The frozen oil was then removed from between the electrodes cut in half in a plane normal to the field, and each half placed, successively in a Faraday pail, giving the sign of the charge and approximate value of potential. The experiment is difficult as the oil quickly loses both solid state and stored charge. However, the results indicated clearly substantial charges in each of the halves, corresponding to the potential distribution curves of Figs. 1, 2, 3, and 4. A volumetric distribution of charge rather than a surface layer at the electrodes is thereby indicated.

The potential distribution in paraffin was also measured (see Fig. 5). The paraffin was melted into the condenser, the voltage applied while it was in the liquid state until the steady condition was reached. It was then allowed to solidify, voltage being maintained on the electrodes. After solidification, the potential distribution

[7] J. B. Whitehead and S. H. Shevki, "D-C Clean-up in Insulating Oils," presented Summer Convention, A. I. E. E., June 24–28, 1935.

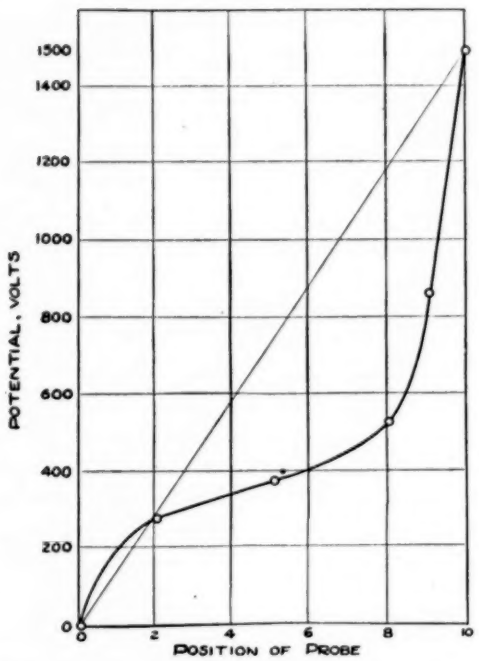

FIG. 5. Potential distribution for paraffin. 1500 volts applied.

as shown in Fig. 5 was measured. The unsymmetrical distribution indicates that the space charge is practically entirely of one sign and suggests that the ions of one sign pass freely to the electrode whereas those of the other sign do not. Following these observations, the solid block of dielectric was removed from the condenser and tests with the Faraday pail indicated a negative charge corresponding to the location and shape of the potential distribution curve. The paraffin was also cut into two pieces in a plane parallel to the plates and the sum of the potentials observed for each half was equal to that of the whole piece before cutting. Experiments of this character must be performed quickly as the paraffin loses its stored charge rapidly unless carefully insulated. These observations also indicate clearly a distribution of the total space charge through the whole volume of the dielectric.

Behavior on reverse potential

If in the steady state under applied voltage, the voltage is suddenly removed, the plates short circuited for a brief instant, and then the same value of potential is applied in the opposite sense, the variation of the current with time may be followed by photographic means, using the string galvanometer or the oscillograph.[8] Photographs of the reverse current show that the current always remains constant for a few seconds after reversal, then rises quickly to a peak value and then falls away at much the same rate, or sometimes very slowly, to a final steady value. A tracing from a typical photographic exposure is shown in Fig. 6. The reverse current curves for oil (A) shown in Figs. 7 and 8 are plotted from the photographs; the upper curves show the corresponding potential variation at a selected point in the dielectric. The curves indicate that the potential on reversal passes through practically its entire variation or has arrived at its full value when the sharp maximum in the current has passed, and that it varies most rapidly while the current is passing through its most rapid variation. Numerical data taken from the curves of Figs. 7 and 8 are given in Table II. They indicate that following reversal, the current remains constant in value for a second or more. This value is usually from 1 to 2 times the value of the long time steady-state current before reversal of voltage, but never

[8] J. B. Whitehead, Trans. Electrochem. Soc. **65**, 83 (1934).

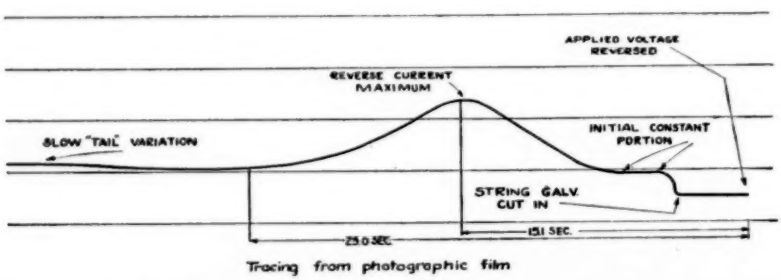

FIG. 6. Current on reversal of applied voltage. Oil (A).

TABLE II. *Ionic mobilities. Oils (A) and (B).*

SPECIMEN	VOLTS	TEMP.. (°C)	CURRENT (amp. $\times 10^{-10}$) before reversal	CURRENT (amp. $\times 10^{-10}$) after reversal *initial*	CURRENT (amp. $\times 10^{-10}$) after reversal *max.*	TIME (Sec. current max.) start	TIME (Sec. current max.) crest	TOTAL SPACE CHARGE (coulombs)	MOBILITY (cm/sec./volts/cm)
				Oil (A), Plate Separation 1.9 cm					
B	1000	22.5	4.9	5.0	20	14.0	31.0	6.8×10^{-8}	1.06×10^{-4}
C	1500	23	7.0	9.0	30	4.5	15.0	15.8×10^{-8}	1.04×10^{-4}
B'	1000	44	10.0	11.5	23	2.6	11.0	5.2×10^{-8}	2.15×10^{-4}
C'	1500	47	13.0	12.5	45	1.1	6.1	11.7×10^{-8}	2.4×10^{-4}
				Oil (B), Plate Separation 1.1 cm					
H	1500	58	102.0	106.0	189.0	35	600	20.7×10^{-8}	2.1×10^{-6}
H'	1500	58	96.5	63.0	130.0	40	600	19.5×10^{-8}	2.1×10^{-6}

greater. The reverse current maximum is from 2 to 6 times that of the earlier steady-state current and following the sharp maximum may decrease slowly over a long time to the final steady value. The maximum increases with the potential gradient and with temperature. The reverse maximum is greatest in magnitude when observed after the space charge has reached equilibrium condition. The higher the temperature and the higher the applied voltage, the shorter the duration of the initial constant current and the sharper the current maximum on reversal. For applied voltages less than 500 volts, the reverse maximum is very low and detected only with difficulty. Values of space charge computed by integrating the area of the reverse current maximum, i.e., the area of above the long time steady (conduction) current, are of the same order of magnitude as those computed from the potential distribution.

Computation of ionic mobility

The potential distribution curves reverse themselves accurately on reversal of applied voltage. The time required for such reversal is clearly indicated by the reverse current and potential time curves of Figs. 7 and 8. Knowing the distance between electrodes, and assuming that the new potential distribution on reversal is caused by the passage of the space charges to the opposite electrodes, we have a simple overall means of determining the average mobility of the ions making up the space charges. Accordingly we have: $k=d/E\cdot t$, in which k=mobility in cm/sec./volt/cm, E=gradient in volts/cm, d=average length of path of ions in cm, t=time in sec. for reversal.

In applying this formula, the most uncertain factor is t for in some cases the approach to the final steady value after reversal is very slow; however, the steep slopes of the current maxima indicate that the greater part of the space charge must change position more or less rapidly. A more accurate determination appears probable in using for the elapsed time, the interval between the initial rise of the current maximum and the maximum itself, and assuming that at the latter instant the space charges have traversed half the distance between the plates. Values of mobility so computed are given in Table II. It is seen that within the range measured, they are independent of the potential gradient, increase with temperature, and are roughly 100 times greater in oil (A) than in oil (B), corresponding to the large difference in viscosity of the two oils. It is to be noted also that the order of magnitude of the mobility in oil (A) is 10^{-4} cm/sec./volt/cm, corresponding to the earlier measurements of Whitehead and Marvin. It may also be noted that at the maximum of reverse current, the reverse potential distribution has been largely established. This means that at this time a portion of the oil at least is subjected to the counter-gradient of the polarization caused by the space charge. This means that the resultant gradient is less than that corresponding to the applied potential and the average mobilities computed above may have somewhat higher values.

The mobility may also be computed from the value of the reverse current maximum and the total volume of space charge, again assuming that in reversal the total space charge reverses its position. Two values of the space charge are

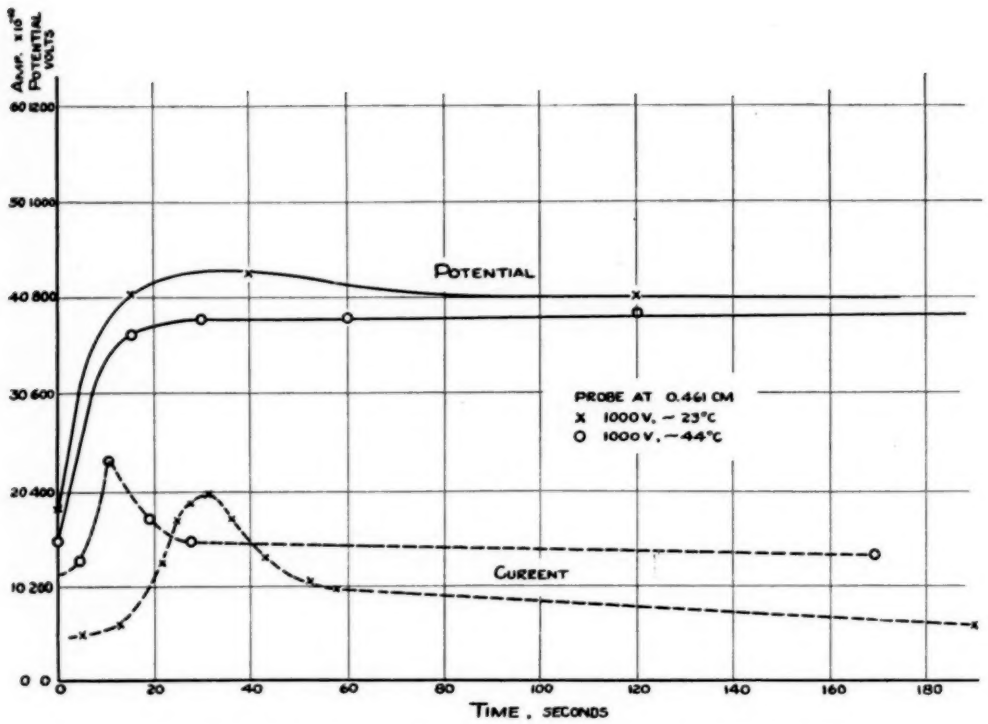

FIG. 7. Variation of potential and current on reversal at 1000 volts.

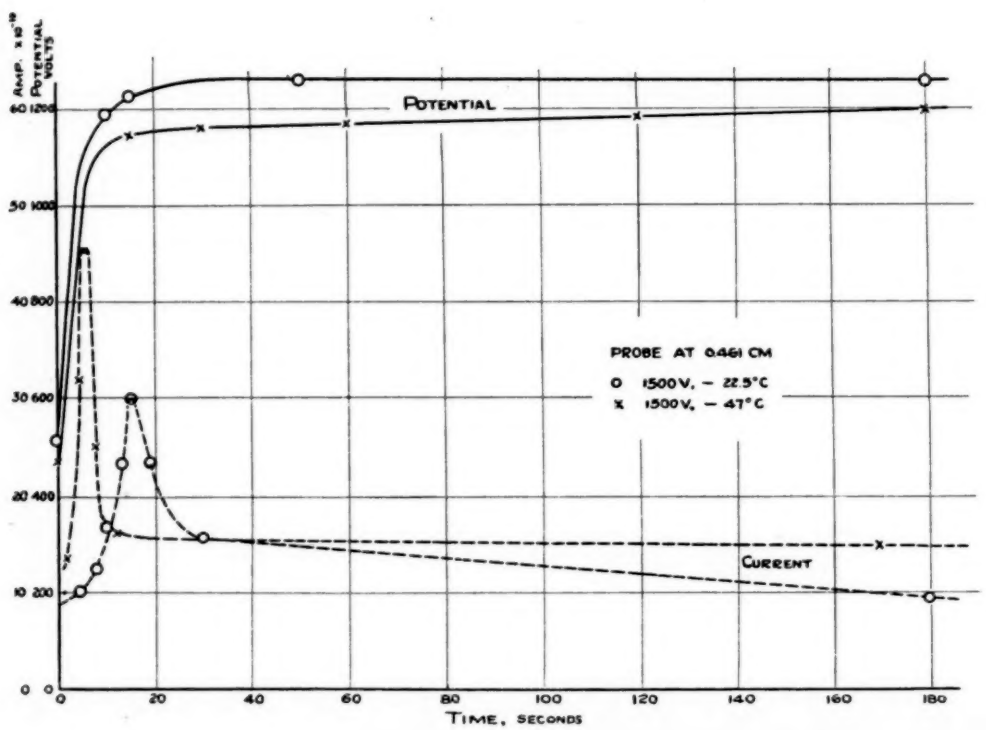

FIG. 8. Variation of potential and current on reversal at 1500 volts.

available, one as taken from the potential distribution curves and the other by integrating the area which lies above the steady state (conduction) current. The two values of space charge so computed are of the same order of magnitude, but do not agree closely. The mobilities so computed for oil (A) are about one-tenth the values computed by the first method and as given in Table II. A possible explanation is the recombination of the ions of opposite sign, as the two space charges must pass each other in moving to the opposite plates.

Discussion

Two features of the foregoing observations stand out as not being in accord with present theories of conduction in liquid dielectrics. They are: (1) the reverse current maximum, and (2) the initial relatively low constant value of current on reversal.

When in the steady state, the current voltage relations in a pure insulating liquid are very similar to those in gases, namely, initial linear relation, followed by saturation, and then rapidly rising current due to secondary ionization. These and other relations indicate strongly that it should be possible to extend the ionization theory as developed for gases also to the phenomena of liquids.[9] Unequal potential distribution and space charges are found in gases and are in accord with gas theory. The space charges are due to space variations in ionic density, but the ions themselves are in uniform motion towards the electrodes. When the applied voltage on parallel plates is reversed, the current after reversal, in accordance with gas theory, should be approximately of the same value as before reversal, and should not vary with time. Consequently, the pronounced maxima found in the reverse current behavior of insulating liquids is apparently not accounted for by the laws explaining space charge and current in gases. The initial constant current on reversal is apparently in accord with the behavior to be expected from gas-laws. Its order of magnitude is the same as the preceding long-time steady state current. Usually it is slightly greater, and this is readily explained by the fact that immediately after reversal, the space charge polarization and the applied voltage are now both in the same direction so that the over-all gradient at the beginning of reversal is somewhat higher than that corresponding to the applied voltage. On the other hand, this initial current, although constant over an appreciable interval, then merges into the rapidly rising reverse current maximum and there appears no obvious reason why the two should be separated in seeking for an explanation.

In the neutral state, even when highly purified, insulating liquids always show some conductivity albeit of very low value, due to traces of impurities, radioactive influence, etc. The total number of ions present rises to equilibrium conditions as related to recombination and diffusion. Some of the free ions attract to themselves clouds of neutral molecules, thus constituting large and sluggish ions. Under normal electric gradients, an ion may carry with it as it moves a part of this surrounding cloud. As the gradient increases, however, it may be expected finally to shed the cloud completely.

When a potential difference is applied, if not too high, there will be motion of both the old heavy ions and newly generated free ions towards the two electrodes. The old heavy ions will move much more slowly and if they are sufficient in number a practically steady initial value of current may result as often observed.[8, 10] As the ions arrive at the electrodes, some of them are discharged, but others of them are not discharged, retaining enough of their neutral envelopes to prevent complete arrival at the electrode surface. Space charges will, therefore, accumulate near the electrodes due partly to the steady withdrawal of freshly formed ions from the central regions in accordance with gas behavior, and also due to the accumulated and more or less stationary heavy ions with their surrounding clouds of neutral molecules. As the space charge increases and the internal gradient decreases, there is a greater and greater tendency for an increase in the number of these heavy ions with relatively wide distribution through the volume of the liquid. Both of these elements of space charge are necessary for a

[9] G. Mie, Ann. d. Physik **26**, 597 (1908).

[10] J. B. Whitehead, Trans. A. I. E. E. **50**, 692 (1931).

complete explanation of the phenomena as observed.

The long-time steady state current is due principally to the constant supply of newly formed more mobile ions. The initial reverse current is due only to the newly generated mobile ions, the conductivity for this brief period being the same as the final conductivity of the preceding opposite period. The reverse current maximum is apparently due principally to the space charge stored up in the large sluggish ions, consisting of molecular aggregates. No such maximum is to be expected from the new more mobile ions. A difficulty in this view exists, however, in the time interval which elapses before the rise to the maximum begins. Considered merely as mobile ions, we would expect them to take up their new direction and velocity immediately on reversal of the field. A possible explanation suggests itself as follows: The heavy ions with their envelopes of neutral ions pack more or less tightly in the region nearest the electrodes. Because of their size, the mobilities of these aggregates must be very low at the start, adding practically nothing to the conduction current. However, under the continued action of the field, particularly in the central region where the density of the heavy ions is less, and under the added influence of the counter-polarization, the ions, as they get into motion, begin to shed their neutral envelopes, thereby assuming a steadily increasing velocity. This process communicates itself in turn to the aggregates lying nearer the plates until finally the whole volume of heavy ions have shed their neutral molecules and assume their maximum possible mobility, thus setting up the reverse current maximum as observed. The accumulation of the opposite space charge then causes a decrease in velocity and a further accumulation of neutral envelopes and a return to the heavy sluggish state.

In connection with the value 10^{-4} cm/sec./volt/cm for the mobility in oil (A), it is to be noted that this figure is of the order of that corresponding to the mobilities of ions in electrolytic solutions. This is in accord with theoretical discussions by Gemant,[11] Nikuradse,[12] and others who ascribe an electrolytic character to the conductivity of insulating liquids. Nikuradse in fact has mentioned even higher mobilities of the order 10^{-3} for certain insulating liquids. Hofmann,[13] using an optical method and cinema camera, has shown recently that the mobility of the ions in a transformer oil immediately following the first application of voltage is of the order 10^{-4} cm/sec./volt/cm. All these figures strongly suggest that the ions involved in the conductivity of insulating liquids in certain cases at least are electrolytic in their origin. However, it is to be noted that for the oils reported in this paper, as well as the others referred to, all have substantially higher values of viscosity than those for the usual electrolytic solutions, which would call for a lower mobility if the ion is of simple electrolytic character. It appears probable therefore that in the case of insulating liquids, other elements may be present than those included in the common theory of electrolytic dissociation and conduction.

[11] A. Gemant, *Elektrophysik die Isolierstoffe* (Julius Springer, Berlin, 1930).
[12] A. Nikuradse, *Das flüssige Dielektrikum* (J. Springer, Berlin).
[13] R. Hofmann, Zeits. f. Physik **92**, 739 (1934).

Dynamical Similarity Laws of the Mercury High Pressure Discharge

G. HELLER, *Natuurkundig Laboratorium der N. V. Philips' Gloeilampenfabrieken, Eindhoven, Holland*

(Received June 17, 1935)

Dynamical similarity laws of the high pressure mercury vapor discharge have been set up. These laws are based on principles which determine characteristics of a high pressure discharge in thermal equilibrium. Characteristics of discharges can be determined by measurements on models if the model contains the same mass of mercury gas per cm and is supplied with the same wattage per cm of length of tube as the main construction. The temperatures of the walls of discharge tube should be the same. In formulating the above requirements self-absorption has been neglected. Experimental tests have shown the validity of the similarity theorems.

§1. INTRODUCTION

FREQUENTLY it occurs that the engineer, though knowing the physical principles which govern the processes in a newly constructed device, is unable to predetermine its characteristics by calculation because of the mathematical difficulties involved in this problem.

In such circumstances he has recourse to experiment, determining the interesting features of his new design by means of models. In order to apply the data yielded by model research to the main construction C the model M should correspond with C in all actual details. It is often impossible, however, to make the dimensions of C and M equal. Thus there arises the problem, how to effect a compromise which will ensure, that the processes of C and M are analogous in such a way that measurements obtained from M are conclusive with respect to C.

A general method of treating this problem may be outlined as follows: If C and M are similar, it should be possible to choose such different units, measuring corresponding quantities in C and M, that the differential equations and boundary conditions determining the process investigated agree numerically in both devices. Then, the results of investigation will also agree numerically and the conversion factor follows from the dimension of the measured quantity. The characteristic quantities of zero dimension, in particular, should have the same value in C and M.

§2. THE PHYSICAL PRINCIPLES OF THE MERCURY HIGH PRESSURE DISCHARGE

From the preceding section it is apparent that similarity considerations are possible only if the physical principles of the process are known. It is necessary therefore, first to give a short treatment of the physical theory. The principles determining the characteristics of the high pressure discharge and the similarity laws obtained therefrom are known from comprehensive investigations of Elenbaas.[1–4]

Contrary to the low pressure discharge the high pressure discharge is in thermal equilibrium. The temperature of the gas determines the velocity distribution of atoms, ions and electrons; it determines the degree of ionization and by this the electric conductivity of the positive column and thus the wattage supplied by a given current. It further determines the wattage dissipated by radiation, heat conduction and heat convection. From the differential equation of the temperature, deduced in the following two sections, the similarity laws of the positive column will be readily found. We confine ourselves to considering 1 cm of an infinitely long column. The following notation will be used:

Significance	*Notation*
Cylinder coordinates	r, z
Inner radius of the tube	r_0
r/r_0	x
Time	t
Absolute temperature	T
Pressure	P
Electric field in the direction of the axis (gradient)	G
Current density	i
Density of the mercury vapor	ρ
Hg mass in 1 cm tube length	m
Thermal conductivity	σ
Mobility of electrons	B

[1] W. Elenbaas, Physica **1**, 211 (1934).
[2] W. Elenbaas, Physica **1**, 673 (1934).
[3] W. Elenbaas, Physica **2**, 45 (1935).
[4] W. Elenbaas, Physica **2**, 169 (1935).

Degree of ionization	α
Ionization energy of the mercury atom	$\epsilon_i = 1.65 \cdot 10^{-11}$ erg $= k \cdot 120{,}000°\mathrm{K}$
Charge of 1 g of Hg ions	$q = 1.445 \cdot 10^{12}$ e.s.u.
Boltzmann constant	$k = 1.37 \cdot 10^{-16}$ erg/grad
Constant of Saha's formula	$K = 0.335$ g cm^{-1} sec^{-2} grad$^{-5/2}$
Constant of Langevin's formula	C

The notation given above refers to M; quantities referring to C are included in brackets.

(a) Ionization and current density

Saha's[5] formula determines the degree of ionization:

$$\alpha^2 P/(1-\alpha^2) = K \cdot T^{5/2} e^{-\epsilon_i/kT}. \tag{1}$$

For all temperatures attainable in practice α is $\ll 1$, because ϵ_i/kT will remain large even at the highest temperatures.

Using the laws of an ideal gas we assume P to be proportional to m/r_0^2. Neglecting α^2 in the denominator of (1) there follows:

$$\alpha^2 m/r_0^2 = S(T), \tag{2}$$

whereby $S(T)$ is a function of the temperature only.

From the mobility B of the electrons the current density:

$$i = \alpha \cdot \rho \cdot q \cdot B \cdot G \tag{3}$$

is obtained, neglecting the mobility of ions.

B is inversely proportional to the concentration ρ. According to Langevin[6] we may assume:

$$B \cdot \rho = C/T^{\frac{1}{2}}. \tag{4}$$

Combining (4) and (2) we obtain from (3):

$$i = (G r_0/m^{\frac{1}{2}}) \cdot C \cdot q [S(T)/T]^{\frac{1}{2}}. \tag{5}$$

(b) Energy balance and differential equation of the temperature

Consider a cylindrical sheet of radius $r = r_0 \cdot x$ and thickness $dr = r_0 dx$. The wattage supplied is according to (5)

$$dL = i \cdot G 2\pi r dr$$
$$= (G^2 r_0^3/m^{\frac{1}{2}})[C \cdot q (S/T)^{\frac{1}{2}} 2\pi x dx]. \tag{6}$$

The same wattage must also be dissipated. Neglecting the contribution of convection, only thermal conduction and radiation will be taken into account. The wattage given off by thermal conduction amounts to:

$$dW_1 = \frac{d}{dr}\left(2\pi r \sigma(T) \frac{dT}{dr}\right) dr = \frac{d}{dx}\left(2\pi x \sigma \frac{dT}{dx}\right) dx. \tag{7}$$

The radiation, when dealing with the phenomenon of self-absorption, is subject to very complicated laws. Fortunately the greater part of energy radiation is coming from transitions between excited states of the atom. As mercury atoms in those excited states exist only in very small concentrations, we may assume that self-absorption is of little influence. Then the radiant energy will be proportional to the number of excited mercury atoms:

$$dW_2 = m 2\pi x dx F(T). \tag{8}$$

In this formula $F(T)$ is a function of the temperature only which actually contains the excitation energy ϵ_a in the Boltzmann factor $e^{-\epsilon_a/kT}$. Combining (6), (7), (8) we obtain from the energy balance:

$$dL = dW_1 + dW_2$$

the differential equation:

$$\frac{d}{dx}\left(x\sigma(T)\frac{dT}{dx}\right) + mF(T)x = \frac{G^2 r_0^3}{m^{\frac{1}{2}}}\left(C \cdot q \left(\frac{S(T)}{T}\right)^{\frac{1}{2}} x\right). \tag{9}$$

This differential equation determines the temperature as a function of x and of the parameters m, G, r_0. Knowing the temperature distribution, we may calculate from (5) the current density, from (6) the wattage supplied, from (7) the heat, transported by conduction, from (8) the energy radiated. We see that the characteristic properties of the column are entirely determined.

§3. The Similarity Principles of the Mercury High Pressure Discharge

As we cannot solve Eq. (9), the characteristics of a model should be experimentally determined. It is the purpose of similarity dynamics to

[5] M. N. Saha, Phil. Mag. **40**, 472 (1920).
[6] Langevin, Ann. d. chim. et phys. **81**, 5, 245 (1905).

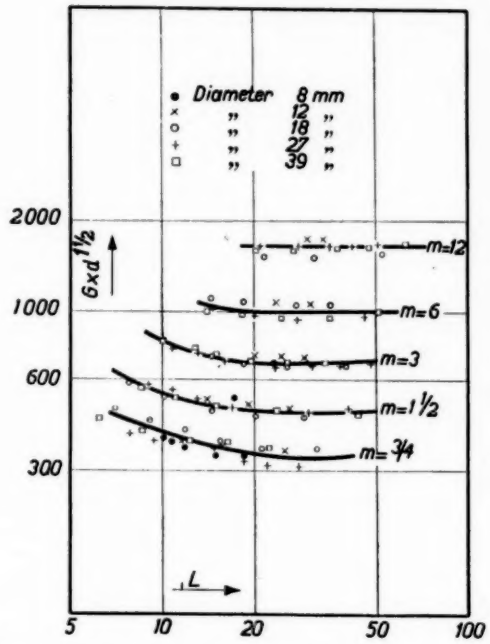

FIG. 1. Product gradient·(diameter)$^{1\frac{1}{2}}$ as a function of the power input, measured with tubes of different diameters d. The similarity laws require this product to be independent of d.

predetermine from model research the particulars of the main construction with other parameters (m), (G) and (r_0). It has been indicated in the introduction how this is effected. The parameters of M should be chosen in such a manner, that Eq. (9) agrees numerically for M and C. It is apparent, that this only holds, when:

$$m=(m) \quad \text{and} \quad G^2r_0^3/m^{1\frac{1}{2}}=(G)^2(r_0)^3/(m)^{1\frac{1}{2}}. \quad (10)$$

Then we obtain from the Eqs. (6), (7), (8):

$$L=(L), \quad W_1=(W_1), \quad W_2=(W_2). \quad (11)$$

Hence we may state the theorem:

High pressure discharges are similar if they agree in the quantity m of mercury gas and in the wattage supplied both per cm of length of the tube. In similar discharges the squares of the gradients are inversely proportional to the third power of the tube radii. Similar discharges dissipate the same wattage (per cm of length of the tube) by conduction as well as by radiation.

To the two requirements for similarity, mentioned above, should be added that the boundary conditions of (9) i.e., the temperature of the bulb, shall agree. To guarantee this, for two discharges of different diameter, the smaller one should be cooled more thoroughly. Fortunately, the gradient of the column has proved to be practically independent of the external temperature. (When heating up to 300°C Elenbaas[4] found an increase of approximately three percent.) The influence of external temperature thus will be neglected in the following considerations.

To test our theorem of similarity it should be proved that $G^2r_0^3$ depends on L and m but not on r_0. This similarity law is well confirmed by experiment as diagrammatically shown in Fig. 1. In the range of diameters between 8 mm and 39 mm the quantity $G\cdot r_0^{3/2}$ appears to be the same function of L and the parameter m within the accuracy of measurements.

§4. Generalization of the Conception of Similarity

Integrating Eqs. (7), (8), (9) over x we obtain:

$$\left.\begin{aligned} &W_1=A, && \text{a}\\ &W_2=B\cdot m, && \text{b}\\ &L=A+Bm=(G^2r_0^3/m^{1\frac{1}{2}})\cdot D. && \text{c}\end{aligned}\right\} (12)$$

Here A, B, D are integrals, depending on the temperature distribution only. They will be considered as functions of the "effective average temperature T_{eff} of the path of discharge, assuming by hypothesis, that the value of these integrals at a given effective temperature does not actually depend on other parameters, in particular on m. Considering the agreement of effective temperatures as similarity in a broader sense, the following similarity laws are obtained.

$$L/(A+Bm)=(L)/[A+B(m)], \quad (13)$$

$$\frac{G^2r_0^3m^{-1\frac{1}{2}}}{A+Bm}=\frac{(G)^2(r_0)^3(m)^{-1\frac{1}{2}}}{A+B(m)}. \quad (14)$$

Thus $$L/G^2r_0^3m^{-1\frac{1}{2}}=(L)/(G)^2(r_0)^3(m)^{-1\frac{1}{2}} \quad (15)$$

and further: $$W_1=(W_1), \quad (16)$$

$$W_2/m=(W_2)/(m). \quad (17)$$

Utilizing these equations we may state the generalized theorem: High pressure dis-

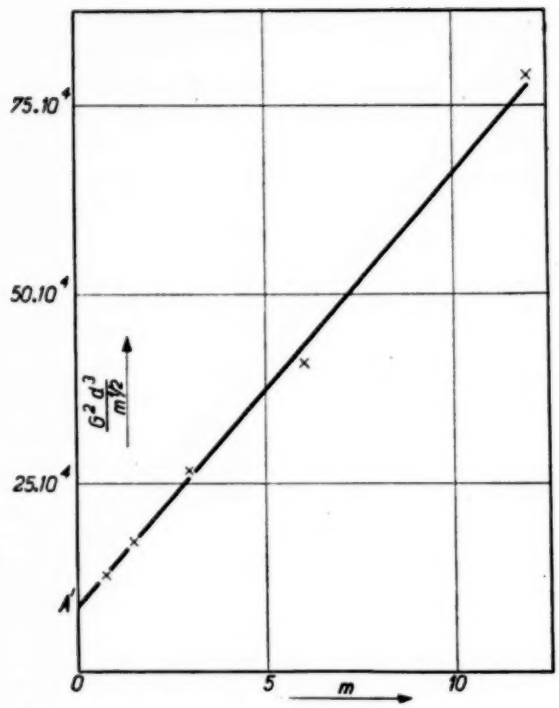

FIG. 2. $G^2d^3/m^{\frac{1}{2}}$ as a function of m. Crosses: measurements with similar discharges, taken from the curves of Fig. 1. Drawn line: the linear function $A'+B'm$ with: $A'=8.5\cdot10^{-4}$, $B'=5.75\cdot10^{-4}$.

charges are similar if they agree in the quantity $L/G^2r_0^3m^{-\frac{1}{2}}$.

In similar discharges the gradient is determined by

$$G^2(2r_0)^3/m^{\frac{1}{2}}=8(A+Bm)/D=A'+B'm. \quad (18)$$

Similar discharges dissipate the same wattage by conduction whilst the radiation will be proportional to the (different) values of m.

This theorem may be tested simultaneously with the determination of A' and B' by representing $G^2(2r_0)^3/m^{\frac{1}{2}}$ as a function of m for similar discharges. Fig. 2 drawn from the same measurements as Fig. 1 indicates that Eq. (18) is fully confirmed. The drawn line corresponds with:

$$A'=8.5\cdot10^4,\ B'=5.75\cdot10^4,\ D=6.25.$$

These values have been proved to hold between the limits:

$$20 \text{ watt/cm} < L < 50 \text{ watt/cm},$$

$$\tfrac{3}{4} \text{ mg/cm} < m < 12 \text{ mg/cm}.$$

§5. Application of the Similarity Theorem to Light Emission

Theory

Eqs. (13), (16), (17) yield the following remarkable conclusions:

(a) From the wattage supplied and radiated, an efficiency factor with respect to the radiation may be defined by

$$\eta = \text{energy radiated/energy supplied.}$$

According to (12) a, b, c one obtains

$$\eta = B'm/(A'+B'm); \quad (19)$$

η is a monotonous increasing function of m. As far as the similarity laws hold exactly, the spectral energy distribution of the radiation should agree for similar discharges. Thus the "economy" defined as the intensity (in a certain spectral frequency) divided by the wattage input should be proportional to η.

(b) Consider similar discharges of equal power input $(L)=L$. Then $(m)=m$, as is apparent from Eq. (13). For such discharges $(W)=W$ by Eq. (17). For similar discharges of equal power input per cm, the energy radiated per cm is the same. The surface brightness of such discharges will be inversely proportional to the radius of the tube. Insofar as the laws of similarity hold, there is no limit to the extent to which the surface brightness may be increased by decreasing the radius of the tube.

Experiment

(a) Fig. 3 illustrates the measured economy compared with those calculated according to (19). Qualitatively the curves agree well. The measured lack of efficiency, increasing with rising values of m may be understood from the neglected influence of self-absorption. Because of the influence of self-absorption the spectral energy distribution of similar discharges may differ considerably. Interesting features concerning the spectrum in the case of extremely high pressures have been investigated by De Groot.[7]

(b) The luminous output of similar discharges should be independent of r_0. Fig. 4 shows that this conclusion is experimentally well confirmed.

[7] W. de Groot, De Ingenieur **50**, E92 (1935).

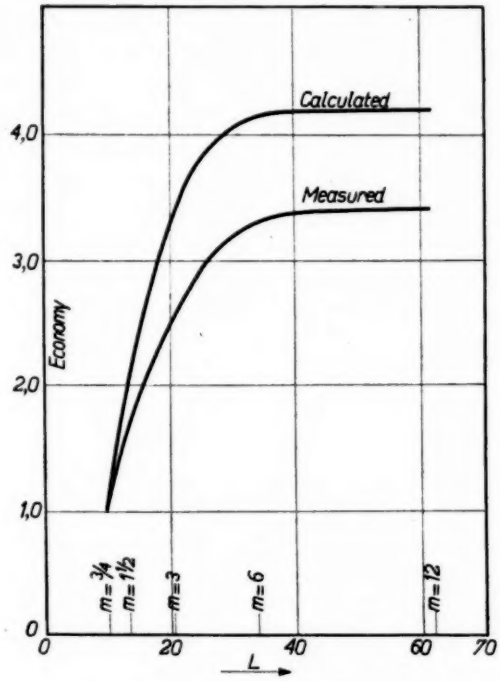

FIG. 3. Economy E (arbitrary units) of the green mercury line $\lambda = 5461$A as a function of the power input. The units are chosen in such a way that for $m = 0.75$ mg/cm $[L = (8/D)(A' + B'm) = 10$ watts/cm$]$ the economy E = const. $\eta = 1$ both theoretically and experimentally. The difference between the measured curve and the calculated function may be ascribed to self-absorption.

The slight decrease of intensity at small radii is again the result of self-absorption.

If a high efficiency, combined with high surface brightness is desired, the preceding considerations direct us (a) to large values of m, (b) to small radii r_0; both arguments point to extremely high pressures. Proceeding in this direction C. Bol designed discharge tubes of 3 mm diameter, bearing a pressure up to 300 atmos. Operating these tubes with a power of 600 watt/cm van Alphen measured a luminous flux of 30,000 lumen/cm.

To prove the applicability of our similarity theorems to such extreme constructions, we will compute the radiation according to (19), using as model a discharge of:

$r_0 = 1$ cm, $L = 40$ watt/cm, $m = 3.1$ mg Hg/cm.

According to Elenbaas[1, 2] this model has a vapor pressure of accurately 1 atmos. and a light output:

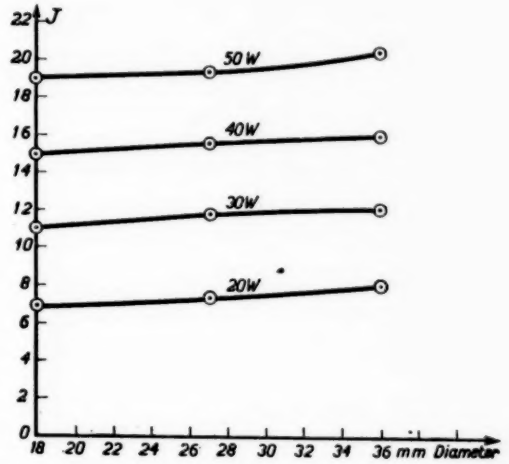

FIG. 4. Intensity of the green mercury line (arbitrary units) for similar discharges ($m = 12$ mg/cm of tube length) as a function of the diameter. The slight increase may be ascribed to self-absorption.

$$W = 1650 \text{ lumen/cm}.$$

Hence the light output of the main construction will be:

$$(W) = W \cdot \frac{(L)}{L} \cdot \frac{(\eta)}{\eta} = W \cdot \frac{(L)}{L} \cdot \frac{B'(m)}{A' + B'(m)} \cdot \frac{A' + B'm}{B'm}.$$

Introducing $(L) = 600$watt/cm, $m = 30$mg,Hg/cm, one obtains:

$$(W) = 34{,}200 \text{ lumen/cm},$$

which is approximately 14 percent higher than the measured output. Estimating the diameter of the contracted discharge to approximately 1 mm, v. Alphen computed an average brightness of 30,000 candles/cm². For comparison the surface brightness of some other sources of light is listed below.

Tungsten filament of an incandescent lamp	200– 3000	candles/cm²
Crater of carbon arc	9000–17,000	" /cm²
High intensity arc	40,000	" /cm²
Sun, as observed from the surface of the earth	165,000	" /cm²

§6. VALIDITY OF THE SIMILARITY THEOREM

In the experiments of Elenbaas the tube diameter varied between $d = 8$ mm and $d = 39$ mm, the mass of mercury varied between $m = \frac{3}{4}$ mg/cm

and $m=12$ mg/cm. The extreme cases, investigated by Elenbaas[4] and Bol,[8] are:

Elenbaas:
$d=39$ mm, $m=\frac{1}{4}$ mg/cm $p=0.045$ atmos. (under operating cond.)
$d=8$ mm, $m=3$ mg/cm $p=4.2$ atmos. (under operating cond.)

Bol:
$d=3$ mm, $m=30$ mg/cm $p=300$ atmos. (under operating cond.)

The operating pressures of Elenbaas are spread in a range of about one hundred-fold. At pressures smaller than a few cm Hg no thermal equilibrium between atoms and electrons will exist. The discharge gradually merges into the low pressure type, for which other similarity principles have been found. On the other hand however, the upper limit does not appear to be reached with 4 atmos.

Two further processes, neglected until now, will become more and more effective at higher concentrations of mercury.

(a) The self-absorption

Figs. 3 and 4 show, that self-absorption plays a noticeable role in all high pressure discharges. Hence the intensity of radiation can only approximately be computed by means of similarity laws. An actual improvement of the theory in this direction seems to be impossible as the laws governing self-absorption are extraordinarily complicated. Experiment shows that the electrical characteristics of the column, especially Eq. (18) for the gradient are hardly influenced by self-absorption.

(2) The heat convection

From the energy dissipating processes, only heat conduction (independent of m) and radiation (proportional to m) have been taken into account. Both processes yield a wattage of long tubes proportional to their length. Estimating the influence of convection, an additional term is found, proportional to m^2 and independent of the length of the tube. This is sufficient reason to neglect its influence on an infinitely long tube. It is however not at all improbable that this effect becomes noticeable on the tubes made in practice. In that case Eq. (12c) should read:

$$A+Bm+Cm^2=(G^2r_0^3/m^{\frac{1}{2}})D$$

and for the gradients the following formula would hold

$$G=m^{\frac{1}{2}}(A'+B'm+C'm^2)^{\frac{1}{2}}/r_0^{\frac{3}{2}}.$$

The measurements of Elenbaas do not exclude the existence of such a quadratic term but certainly it is not of great importance.

Apart from quantitative agreement with respect to the radiation the similarity laws for the gradient have proved to be correct even for the super high pressure discharge of Bol. Probably they will hold in the entire domain of pressure from a few cm up to 300 atmos.

(A brief bibliography is appended.)

[8] C. Bol, De Ingenieur **50**, E91 (1935).

BIBLIOGRAPHY

Similarity laws of the mercury low pressure discharge.
R. Holm, Wiss. Veröff. Siemens K. **3**, 159 (1923).
Thermal ionization of arcs.
L. S. Ornstein, Physik. Zeits. **32**, 517 (1931).
L. S. Ornstein, H. Brinkmann, and A. Beunes, Zeits. f. Physik **77**, 72 (1933).
A. v. Engel and M. Steenbeck, Wiss. Veröff. Siemens K. **10, 2**, 155 (1931).
A. v. Engel and M. Steenbeck, Wiss. Veröff. Siemens K. **12, 1**, 76 (1933).
A. v. Engel and M. Steenbeck, Wiss. Veröff. Siemens K.
A. v. Engel and M. Steenbeck, Naturwiss. **19**, 212 (1931).
R. Mannkopf, Zeits. f. Physik **76**, 39 (1932).
R. Mannkopf, Zeits. f. Physik **86**, 161, (1933).
H. Witte, Zeits. f. Physik **88**, 415 (1934).
Distribution of energy in the radiation of the mercury column.
H. Krefft and M. Pirani, Zeits. f. tech. Physik **14**, 393 (1933).

Electrical Conduction Models for the Solution of Water Seepage Problems

R. D. WYCKOFF AND D. W. REED, *Gulf Research and Development Corporation, Pittsburgh, Pennsylvania*

(Received October 10, 1935)

A method is described for the construction of electrical models with which to solve problems of the flow of liquids through porous media under the action of gravity. With these models the shape of the free surface and the extent of the surface of seepage are determined simultaneously with the potential distribution within the flow system. Four examples are given of the application of the method to the problem of the seepage of water through dams. In two cases the faces of the dams were assumed to be sloping, and in the others they were taken as vertical, the free surface and velocity distributions at the faces of one of the latter cases checking closely with those derived from an analytical solution of the problem. The method of applying these models to the study of more complex gravity flow systems is briefly indicated.

INTRODUCTION

PROBLEMS involving the flow of homogeneous fluids through porous media under the action of gravity in general require very difficult analytical methods for solution.[1] Furthermore the problems may become entirely intractable mathematically when the geometry of the flow system takes on only a reasonable complexity such as is involved in many systems of practical engineering interest. For this reason small scale models duplicating the original in their physical make-up have been used in the study of such problems. In view of the difficulties involved in making such scale models as well as the inherent limitations in the detail and accuracy available, we are presenting here a method based on the electrical analogy of the flow of fluids through porous media which is simple but nevertheless capable of providing reasonably accurate and detailed solutions regardless of the complexity of the problem. While the use of electrical models to obtain potential and streamline distributions in ordinary flow systems is not new, the application of the electrical method to problems of the type discussed here does not appear to have been previously recognized.

THE PROBLEM

The type of problem with which we are concerned is characterized by the presence of at least one boundary of the flow system which is a "free surface" and represents a limiting or boundary streamline over which the pressure is uniform and hence the potential varies linearly with its vertical coordinate. Initially the shape of this free surface is unknown and its intersection with the outflow boundary surface of the system is likewise determined only by the complete solution of the problem. Consideration of a simple two-dimensional system such as shown in Fig. 2 will indicate more clearly the nature of the problem. $AFDE$ represents the cross section of a permeable dam on one side of which water is maintained at height h_e and on the other at height h_w. It is desired to determine the potential and streamline distribution within the system with no *a priori* information regarding the height of the outflow discontinuity or seepage surface BC or the shape of the free surface CD constituting the upper limiting streamline.

THE ELECTRICAL CONDUCTION MODEL

By considering now the construction of an electrical conduction model of the system in question, it is evident that the inflow boundary ED and the outflow surface AB represent equipotential surfaces corresponding to the fluid heights h_e and h_w, respectively. Furthermore the vertical projection of the terminae of all equipotentials on the boundary BCD must be proportional to their potentials, the total potential difference from D to B being proportional to $(h_e - h_w)$.

Fig. 1 shows schematically the electrical equivalent of the two-dimensional gravity flow system already described. Here a rectangular sheet of homogeneous high resistance material $AFDE$ is provided with a highly conducting terminal DE,

[1] M. Muskat, "The Seepage of Water Through Dams with Vertical Faces," this issue.

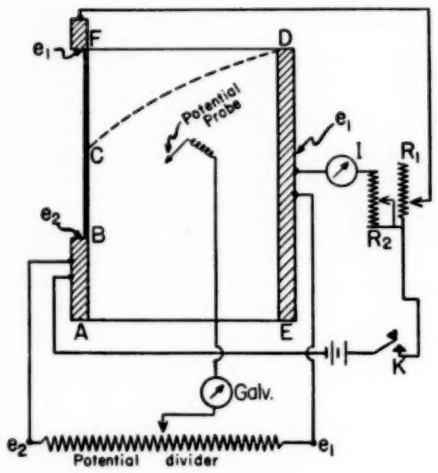

FIG. 1. The electrical circuit for the electrical model of a gravity flow system.

serving to maintain this boundary at a uniform potential e_1. Likewise the outflow boundary is provided with a similar terminal AB at potential e_2 and of height equal to the height of fluid maintained at the outflow boundary. The remainder of the outflow boundary BF is provided with a terminal comprising a resistance strip, the ends of which are maintained at potentials e_1 and e_2 as shown in the figure and having a linear potential distribution along its length BF. Since the maintenance of a uniform potential distribution in this resistance strip, in spite of the lateral influx of current from the conductor $AFDE$, would normally require a nonlinear and unpredictable resistance distribution, the sheet conductor $AFDE$ is made of very high resistance material as compared with the terminal strip BF. In this manner BF may comprise a resistance strip of uniform cross section giving a linear potential distribution on passage of current through it and yet the perturbation in this distribution due to the current feeding into it laterally from the conducting sheet will be negligible. In the models used by the authors the boundary terminal BF comprised a strip having a resistance of 0.0123 ohm per cm while the resistance of the sheet material was of the order of 53.9 ohms per cm (for 1 cm width). This contrast is sufficient to eliminate any detectable departure from linearity in the potential distribution along BF.

The circuit diagram is shown in Fig. 1 and

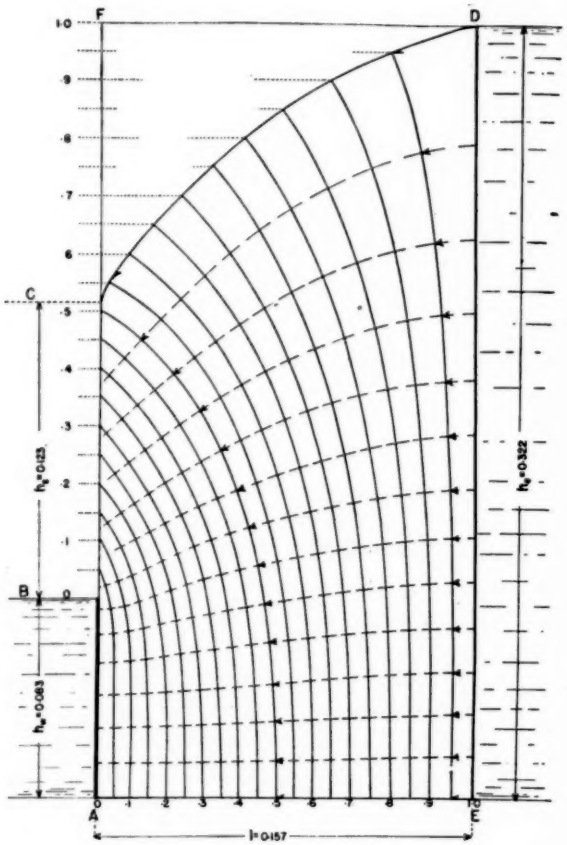

FIG. 2. Potential and streamline distributions in the region of flow of a dam with vertical faces.

requires no discussion except to point out that the rheostats R_1 and R_2 must be adjusted, with the aid of the galvanometer probe circuit and with the potential-divider slider set at e_1, such that the potential at F is exactly the same as the potential of the terminal DE, that is, it must have the value e_1. This equality should be checked periodically during the subsequent work to make certain that no fluctuations occur either through accidental variations in circuit resistance or because of the increase in resistance of the sheet $AFDE$ incident to the cutting operations to be described. A suitable switch or key K is provided so that the battery circuit is closed only during the short interval required in adjusting the position of the probe point for a null reading of the galvanometer. This minimizes troubles caused by heating.

After having set up the electrical system as in Fig. 1 it is clear that the known boundary con-

ditions of the fluid system have been duplicated. Thus is satisfied the requirement that the boundaries DE and AB are each equipotentials, the difference in values of which corresponds to the potential difference between D and B in the fluid system. Furthermore, the potential at F is equal to that at D and the potential distribution along the boundary BCF is linear and proportional to the height. Evidently, however, the shape of the boundary CD, analogous to the free liquid surface or upper limiting stream line in the fluid system, and its intersection C at the outflow face BF is as yet unknown. In fact the determination of this boundary is an important phase of the final solution of the entire problem. In principle, the procedure to be followed in determining this boundary in the electrical model is actually to cut away the conducting material within the area CFD and so to shape the boundary CD that the potential of any point along the boundary CD is proportional to its vertical height above point B. Thus by trial is obtained the simultaneous solution for the free surface and the potential distribution throughout the system. Fig. 2 shows clearly that in the final result all boundary conditions including those for the free surface CD and the "surface of discontinuity" BC are properly fulfilled.

It will now be apparent that proper and easy manipulation of the model dictates certain physical details regarding its construction. Most important is the requirement that the sheet-conductor material may be easily shaped by trial without otherwise disturbing the system. We have found that ordinary Bristol board or other heavy firm paper may be given a coating of graphite which has the desired moderately high resistance, and easily permits the shaping of the boundary CD by gradually cutting away with a sharply pointed knife or other instrument. The use of a moderately sharp needle point in firm contact but not penetrating the graphite surface serves as a satisfactory potential probe. While such graphite material may be available commercially we have been able to make such sheets by spraying onto the Bristol board, twelve to twenty coats of a commercially available graphite colloid.[2] The colloidal solution is made quite dilute by *thoroughly* dispersing the colloid paste in a suitable quantity of distilled water and using it in an ordinary spray gun giving a thoroughly atomized spray. Obviously a very uniform coating of graphite is required and great care is necessary in properly distributing the spray. By applying very thin coats and building up the final thickness by many individual applications, allowing each to dry before further application, a very homogeneous coating is finally obtained. Before using it in a model the homogeneity of the coating should first be tested by applying linear electrodes at each end of the rectangular sheet and tracing 0.1, 0.25, 0.5, 0.75 and 0.9 percent equipotentials which should be straight lines parallel to the electrodes and proportionately distributed along the length of the conductor.

The most satisfactory simple method of making contact with the graphite sheet is to use terminals having very narrow rounded edges clamped firmly to the sheet at numerous points along the length by suitable clamping blocks. The resistance strip used to obtain the linear potential distribution (B–F in Fig. 1) is likewise a strip resistance material clamped edgewise against the graphite sheet. To obtain the necessary rigidity the strip is laid edgewise in a close fitting slot milled in a strip of Bakelite. The strip should project about 1/32 inch along the slot and the Bakelite strip should be chamfered so that when clamped in place the potential probe may be used right up to the terminal and in fact so that the potential distribution along the strip itself may be determined. It is advisable to determine the uniformity of contact before proceeding with the measurements by tracing an equipotential very close to each boundary electrode. Nonuniformity of contact is easily detected by local distortions of the equipotential lines and corrective measures taken by the addition or adjustment of clamps.

Procedure in Obtaining Final Solution

In a simple electrical conduction model where the boundary conditions are completely defined by the statement of the problem and the model constructed accordingly, it is a simple matter to trace 0.1, 0.2–0.9 equipotential lines or to

[2] "Aquadag" (concentrated) manufactured by Acheson Oildag Company, Port Huron, Mich.

decrease the interval between equipotentials if greater detail is desired. Streamlines may then be drawn as orthogonal curves by inspection or more accurately by various mechanical aids. Or, in the simple models, if a more accurate determination of streamline distribution is required, the problem may be inverted so that the observed equipotentials are the streamlines of the real system. This inversion only requires that the *known* boundary streamlines be made equipotentials by applying the terminal electrodes along such limiting streamlines and the normally equipotential boundaries be made insulated or "free" edges. Clearly the system of equipotentials obtained in either case will have the required orthogonal relation to the other and an accurate mapping of both the potential and streamline distribution may be obtained.

In the present case involving flow under the action of gravity, it has already been pointed out that the "free surface" boundary *BCD* (Figs. 1 and 2) is unknown. However, the conditions to be satisfied along this boundary—that the potential at any point is proportional to its vertical height above *B*—is defined in the statement of the problem. Thus the only additional complication introduced in solving the more complex problem is the procedure of cutting away the conducting sheet until, by trial, the free-surface potential distribution requirements have been satisfied. Obviously this should be done in very gradual stages for once cut below the proper point it is impossible to make corrections. It will be found that with a little experience combined with good judgment obtained thereby, it is possible rapidly to approach the final solution. It is quite impossible, however, to outline in detail more specific directions for this procedure. Unfortunately the gravity-flow model is not readily "inverted" as described above so that the streamlines must be drawn as orthogonal curves rather than determined by direct observation.

Typical Solutions

Since the numerical results are available for certain cases of rather simple geometry in the analytical paper[1] already cited, we have selected for reproduction in the model, Case I, of that paper. Thus in Fig. 2 which is a direct copy of the model itself, dimensions h_e, h_w and l correspond, respectively, to dimensions h_e/c, h_w/c, and L/c of Muskat's example and constitute the given boundary dimensions. The final solution obtained from the model is shown by the free surface *CD* and the potential distribution obtained in the manner already outlined. The streamlines shown are drawn in as orthogonal curves and are only approximate.

Table I. *Comparison of analytical and solutions from model.*

	Dimension	Analytical Solution	Experimental Solution
Given Boundaries	h_e/c	0.3223	0.322
	h_w/c	0.0842	0.083
	L/c	0.1619	0.157
	h_s/c	0.1225	0.123

In order to permit a direct comparison between the experimental and analytical results, Fig. 3 was prepared from the data of Fig. 2, the plots being directly comparable with those of Fig. 6 in M. Muskat's paper.[1] It should be mentioned that the curves showing velocity distributions (Fig. 3) are necessarily only approximate since they were obtained by measuring the potential gradient (reciprocal of the distance between equipotentials) at the points in question from Fig. 2 and it is clear that the true gradient at a given point is not obtainable in this simple manner. However, by using the reciprocal of the distance between equipotentials at the points in question as representing the potential gradient and after having established the proper numerical coefficient to make the velocity at the inflow point $E=1.36$ (the value obtained analytically), the other points on the several velocity distribution curves of Fig. 3 were calculated by using this same coefficient.

For convenience Table I shows a comparison of the results obtained analytically and those from the model where again Muskat's notation is used. While less convincing than a detailed comparison of the curves of Fig. 3 and Fig. 6 of the reference, h_s/c which gives the height of the outflow surface is a critical point of the solution and the agreement with the calculated value is excellent.

Thus it is evident that the electrical conduction models of the type described are capable of

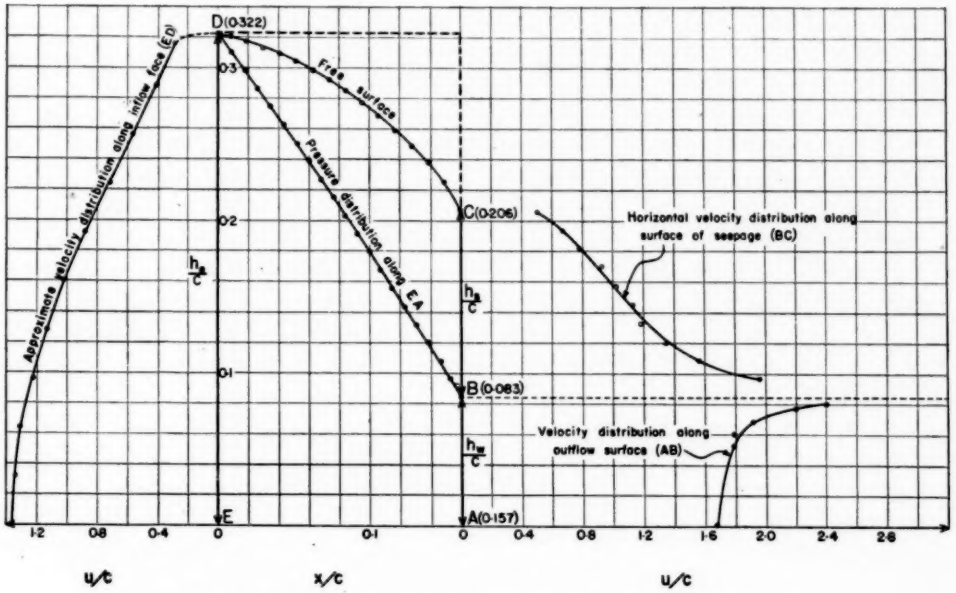

FIG. 3. Velocity and pressure distributions for the dam of Fig. 2.

solving two dimensional problems involving the flow of liquids through porous media under the action of gravity with an accuracy quite sufficient for practical purposes.

In addition to the information disclosed here it is also possible to determine the total flux through the liquid system by merely measuring the total current through meter I, Fig. 1, with the potential divider circuit open, and the maximum potential drop $e_1 - e_2$ across the electrical model, after the solution is complete. From these data the effective over-all conductance of the system may be obtained and since the specific conductance of the material used in the model is easily measured, the over-all conductance of the model may be expressed in terms of the specific conductance of the medium. This coefficient evidently will give the effective permeability of the gravity flow system in terms of the specific permeability of the porous medium, and the liquid flux through the system may be calculated.

As an illustration of such use of the electrical models some interesting results for the case shown in Fig. 2 are given. The effective resistance of the system was measured first with the faces AF and ED as uniform potential electrodes analogous to a simple linear flow system. Next the resistance was measured under conditions corresponding to the case of gravity flow (Fig. 1) but before section CFD was cut away, this being a system which can be solved rigorously by analytical methods. Finally the resistance was determined for the case wherein the free surface CD was cut away and the model had the proper potential distribution (Fig. 2) to simulate exactly the gravity flow system.

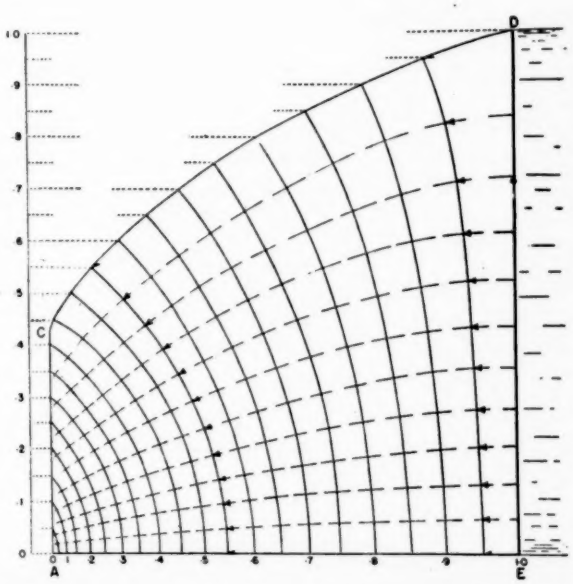

FIG. 4. Potential and streamline distributions in a dam with vertical faces and zero outflow fluid level.

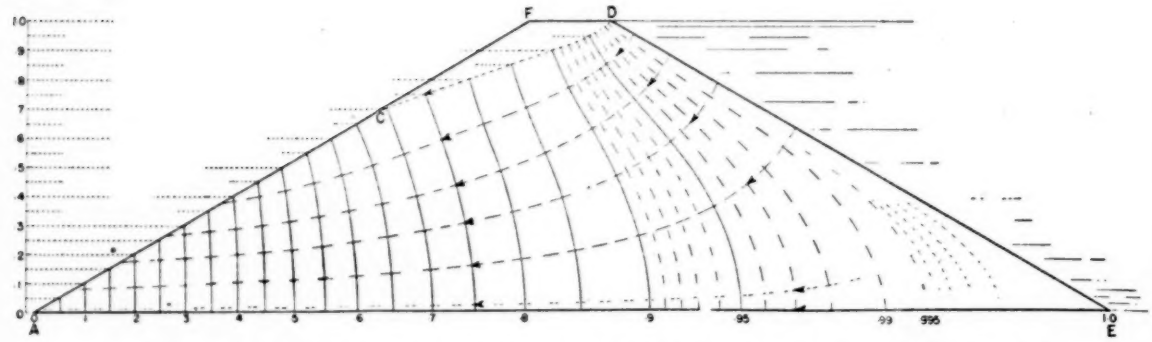

FIG. 5. Potential and streamline distributions in a dam whose faces have inclinations of 30°.

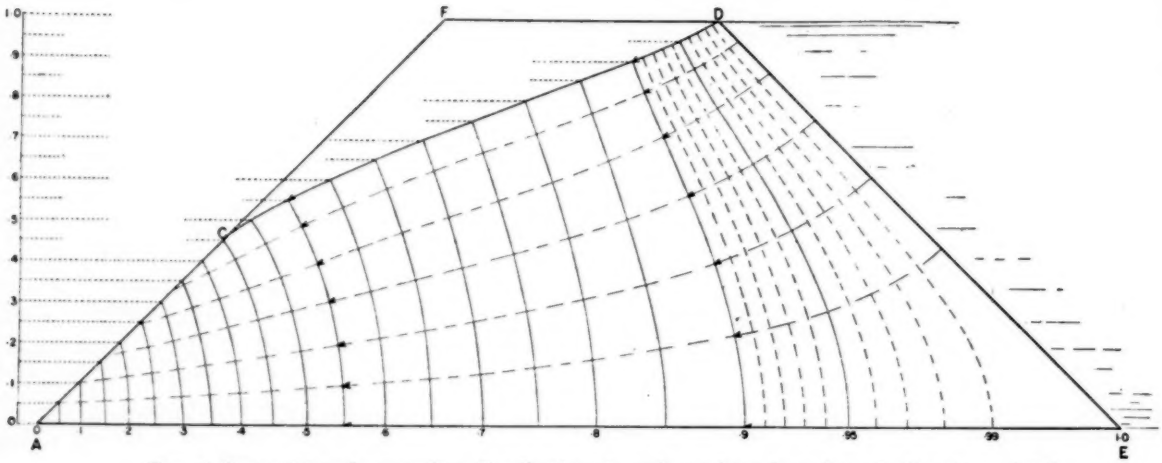

FIG. 6. Potential and streamline distributions in a dam whose faces have inclinations of 45°.

Effective Resistance (ohms)		
Linear System	*Gravity System (No Free Surface)*	*Ratio Linear/Gravity*
27.73	43.78	0.633
27.96	43.56	0.642

These results show that for the system in Fig. 2 having the proper potentials at the boundaries AF and ED but without the free surface CD cut away, the over-all conductivity is 63.7 percent of the conductivity of a linear flow system of identical dimensions. Within experimental error this is in agreement with the theoretical ratio 0.631 obtained by Muskat.

A comparison of the gravity system with and without the free surface has also been made for the above case. The results obtained with two different models are:

Effective Resistance (ohms) *Gravity System*	
Without Free Surface	*With Free Surface*
44.1	44.2
43.5	43.5

It is apparent that the cutting away of the section CFD has a negligible effect upon the over-all conductivity and that within the experimental error of about 0.25 percent, the total flux through the true gravity flow system may be assumed to be the same as in the special case which may be treated analytically.

Fig. 4 shows the solution for the case of a rectangular dam of permeable material where the water level on one side is at D while at the outflow face the water level is at A or zero height.

Figs. 5 and 6 are for the case of a permeable structure of trapezoidal cross section $AFDE$ supporting a water level at D on the inflow face but with a zero water level (A) on the downstream side AF. The free surface CD and the surface of seepage or discontinuity at the outflow face AD and the potential distribution at the base AE are of particular interest.

We wish to emphasize that the particular

examples given here are not intended to illustrate practical problems but rather were selected merely to show the possibilities of the method. Evidently a permeable or earth-fill dam would not be constructed upon an impermeable base as is the case in the present example. For such conditions concrete dams are feasible. Furthermore an earthen dam constructed on permeable foundation strata would be provided with an impermeable central core as, for example, a puddled clay wall extending some distance into the permeable substratum. In addition the toe or heel of the dam or both might be provided with impermeable sheet piling or wall driven into the substratum or with aprons extending outward from the base of the dam. It is evident, however, that such specific conditions may be duplicated in the model even to the extent of introducing variations in permeability by suitable preparation of the conducting sheet. Thus the conductivity of any portion of the model may be made to simulate varying permeabilities in the actual case by using suitable masks and spraying additional coats of graphite upon those portions representing more permeable sections. Almost any degree of complexity could be reproduced in such models and determinations made of the surface of seepage, pressure and streamline distribution and important details derived therefrom. Sand models have been used extensively for such purposes but the electrical conduction models are more easily constructed, permit higher accuracy, and greater detail in the measurements.

The authors are indebted to Dr. M. Muskat for important contributions in this work and to Dr. P. D. Foote for permission to publish this paper.

The Seepage of Water Through Dams with Vertical Faces

MORRIS MUSKAT, *Gulf Research and Development Corporation, Pittsburgh, Pennsylvania*

(Received October 10, 1935)

The method of hodographs, recently developed by Hamel for the analysis of ground-water flow systems containing free surfaces, is applied numerically to six cases of the seepage of water through dams in which the ratio of the inflow fluid head to the width of the dam at the base varied from 2.04 to 1.08. In one case the velocity distribution was computed both along the inflow and outflow faces, as well as along the base of the dam. The pressure and velocity distributions along the bases and the velocity distribution along the inflow faces were found for 5 other cases, in 4 of which the outflow fluid head was zero. The heights of the surfaces of seepage and the total fluxes were calculated for all six cases. These calculations show that the Dupuit-Forchheimer theory of the free surface and velocity distributions in gravity flow systems is definitely wrong, and that the extension of the empirical results of Wyckoff, Botset and Muskat, obtained with radial gravity flow systems, to linear systems is unjustified. The fluxes, however, given by this extension or the Dupuit-Forchheimer theory turn out to be in close agreement with those calculated by the exact theory. The evaluation of the fundamental integral over the argument of the modular elliptic function involved in the calculations is extended beyond the range given by Hamel and Gunther so as to include all real values of the modular elliptic function.

INTRODUCTION

ONE of the major outstanding problems yet requiring explicit solution in the subject of the flow of homogeneous fluids through porous media is that of the flow of liquids through such media under the action of gravity. This type of problem is characterized by the fact that at least one segment of the boundary of the region of flow is a "free surface," the shape of which is not known *a priori*. All that is known about it is that it is a streamline surface over which the pressure is uniform. However, in contrast to the analogous problem of discontinuous motion—as in jets—in the ordinary hydrodynamics where the uniformity of the pressure implies a uniformity in the velocity, the only immediate consequence following here from the constancy of the pressure is that the potential along the free surface varies linearly with its vertical height above a zero plane. Although the analytical problem is that of solving Laplace's equation for the velocity potential Φ:

$$\nabla^2\Phi=0; \quad \Phi=(k/\mu)(p+\gamma g y), \tag{1}$$

k being the permeability[1] of the porous medium, μ the viscosity of the fluid (an effectively incompressible liquid), γ its density, p the fluid pressure, g the acceleration of gravity, and y the vertical coordinate, the difficulties of finding solutions satisfying all the boundary conditions are still very formidable.

The first attempt to treat such problems analytically was that of Dupuit[2] who assumed, in the case of the radial gravity flow into a well, that the liquid moved in towards the wells in vertical shells with a velocity proportional to the slope of the free surface, the square of which being neglected in comparison to its first power. Other approximate theories, as those of Bose[3] and Kozeny,[4] did treat the gravity flow problems from the point of view of Laplace's equation, but no attempt was made in these to find the free surfaces. Rather they were chosen as streamlines, found in the solution, of "reasonable" shape, without imposing on them the requirement of the uniformity of the pressure. The first rigorous treatment was that of Hopf and Trefftz[5] who solved the problem of the drainage of a sloping terrain by a ditch dug at the top of the sand. Here, however, an indirect method of solution was used, the shape of the ditch being determined only after assuming a simple form for the arbitrary function in the

[1] The permeability is defined as the volume of a fluid of unit viscosity passing through a unit cross section of the porous medium in unit time under the action of a unit pressure gradient. For the system of units: cc, cm, sec., atmos., centipoise, the unit has been named the "darcy."

[2] J. Dupuit, *Études theorique et pratiques sur le mouvement des eaux* (1863).

[3] N. K. Bose, Punjab Irrigation Research Institute **2**, No. 1 (1929).

[4] J. Kozeny, Wasserkraft u. Wasserwirtschaft **22**, 120 (1927).

[5] L. Hopf and E. Trefftz, Zeits. f. angew. Math. u. Mech. **1**, 290 (1921).

generalized Schwarz-Christoffel integral for the conjugate function transformation.

Among the experimental studies of the problem of gravity flow through porous media, the most recent is that of Wyckoff, Botset and Muskat.[6] The essential conclusion of these authors, working with radial sand models, was that while the Dupuit formula for the free surface in gravity flow systems was incorrect, it was formally accurate if the heights of the free surface in that formula were interpreted as the *fluid heads* at the *base* (horizontal) of the flow system. Furthermore, with this interpretation, the fluxes through such systems were also correctly given by the equation following from the Dupuit assumptions, namely:

$$Q=\pi k\gamma g(h_e^2-h_w^2)/\mu \log r_e/r_w, \qquad (2)$$

where h_e, h_w were the fluid heads at the external and internal circular boundaries of radii r_e, r_w.

These results were also found to apply to composite flow systems in which a nongravity pressure differential was superposed on that due to gravity, this added differential, however, not being great enough to force the fluid to fill out completely the sand and thus eliminate the gravity component of the flow; that is, when the fluid height at r_e exceeded the sand thickness, while that at r_w was less than the sand thickness, the resultant flux through the system and pressure distribution at the base were shown empirically to be given simply by the sum of the gravity and nongravity components. These results were then generalized—by postulation—so as to give Laplace's equation:

$$\nabla^2 y^2=0, \qquad (3)$$

for the fluid head distribution[7] at the base (horizontal) of every gravity flow system, and a general procedure was given for obtaining the flow rate through any such system, and also for those having both gravity and nongravity components.

The greatest advance, however, yet made in the study of gravity flow systems is that recently made by Hamel.[8] Here, by the use of the method of hodographs in conjunction with the theory of conjugate function transformations, including those defined by the modular elliptic functions, a rigorous treatment was given of two-dimensional systems in which there are not only elements of free surface but also of "surfaces of seepage," as will be described below. It is in this latter respect that Hamel's theory makes a particular advance over that of Hopf and Trefftz, where this additional type of surface element was disregarded, in addition to its provision for taking into account directly the shape of the outflow surface.[9]

Unfortunately, however, the numerical calculations required to get specific results from Hamel's theory are quite tedius and lengthy. The only calculations thus far carried out are those of Hamel and Gunther[10] in which the shape of the free surface for a single case of a problem corresponding to the seepage through a dam with vertical faces was computed. No results are available for the total flow through the system, which is probably of greatest physical interest. In this paper the results are given of the computation of this quantity not only for the particular case of Hamel and Gunther, but also for one other in which the fluid head at the outflow face is nonvanishing, as well as for 4 cases with vanishing outflow fluid head. In addition, the velocity and pressure distributions have been found along the inflow face and base for each case, and also those at the outflow face for that of Hamel and Gunther. These are compared with those which would be implied by the generalization of the results of Wyckoff, Botset and Muskat already mentioned. Finally, some additional analytical and numerical details are given which will considerably lessen the work of studying still other cases.

In order to make clear the principle of the computations, a brief outline of Hamel's theory

[6] R. D. Wyckoff, H. G. Botset and M. Muskat, Physics **3**, 90 (1932).

[7] This equation had also been proposed and used previously by Forchheimer, with, however, the interpretation of y as the height of the free surface above the horizontal impermeable base.

[8] G. Hamel, Zeits. f. angew. Math. u. Mech. **14**, 129 (1934).

[9] Classes of complex variable functions corresponding to free surfaces had already been found by Kozeny (Wasserkraft u. Wasserwirtschaft **26**, 28 (1931)), but no procedure was given for finding the free surface corresponding to any preassigned physical system.

[10] The author is very much indebted to Dr. Hamel for sending him before publication the manuscript giving the detailed calculations for this case.

will be given first, as applied to the specific problem of the seepage through a dam with vertical faces.[11]

Résumé of Hamel's Theory

Hamel's method is essentially that of first mapping the original geometrical outline of the flow system—the z plane—onto a "hodograph plane," in which the independent variables are the velocity components, and then mapping this hodograph plane onto an upper half of a new plane, the λ plane, the boundary of the flow system in the former being transformed into the real axis of the latter. The construction of the figure in the hodograph plane is obtained by the following transformations of the various types of boundary segments.

(*a*) *Impermeable boundary of inclination α to the x axis.* In the notation of Eq. (1), the velocity components (u, v) will be given by:

$$u=-\frac{\partial\Phi}{\partial s}\cos\alpha;\quad v=-\frac{\partial\Phi}{\partial s}\sin\alpha;\quad \frac{v}{u}=\tan\alpha, \tag{4}$$

where ds is a boundary element. Hence for a rectilinear impermeable boundary, the hodograph is a parallel line passing through the origin.

(*b*) *Constant potential surface—stationary body of liquid.* Here by definition $\Phi=$constant, and the velocity components at the surface are:

$$u=-\frac{\partial\Phi}{\partial n}\sin\alpha;\quad v=+\frac{\partial\Phi}{\partial n}\cos\alpha;\quad \frac{v}{u}=-\operatorname{ctn}\alpha, \tag{5}$$

where n is the normal to the surface, so that a rectilinear constant potential boundary gives a line through the origin in the (u, v) plane *normal* to the real boundary.

(*c*) *Free surfaces.* As by definition the pressure is constant along the free surface, Φ is given by:

$$\Phi-cy=C;\quad c=k\gamma g/\mu, \tag{6}$$

where the vertical coordinate, directed upwards, has been taken as y. After noting that the free surface must also be a streamline of the system, it readily follows that along it:

$$v^2+u^2+cv=0, \tag{7}$$

[11] It is assumed throughout that the dam has a length that is large compared to its breadth, so that the problem is essentially two dimensional.

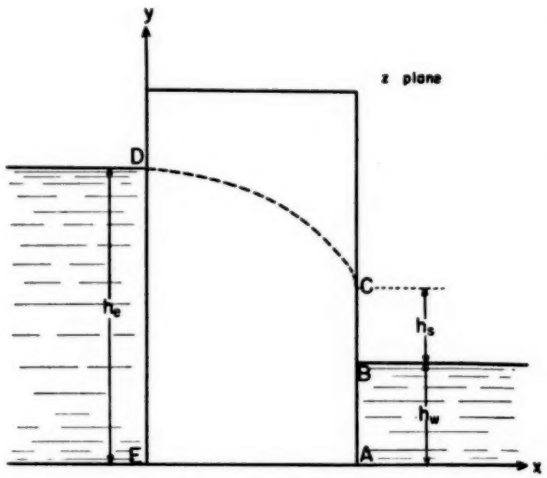

FIG. 1. The z plane representation of a dam with vertical faces.

which is a circle passing through the origin, of radius $c/2$ and center at $(0, -c/2)$. It may be noted that c is the vertical free fall velocity due to gravity.

(*d*) *Surface of seepage.* At a "surface of seepage,"[12] through which a liquid passes and enters a region free of both porous medium and liquid, the pressure is constant, although the surface is not a streamline surface. From this it may be shown that:

$$c\sin\alpha+u\cos\alpha+v\sin\alpha=0, \tag{8}$$

so that if the surface is plane, its hodograph is a straight line normal to the surface and passing through the point $(0, -c)$ which is the lowest point of the circle of Eq. (7) representing the free surface.

By applying these results to the problem of the seepage through a dam, indicated diagrammatically in Fig. 1, it is readily found that its representation in the hodograph plane is as shown in Fig. 2. It is to be noted that whereas in the z plane the exact form of the boundary segment DC, and hence also the terminus of BC, is in principle unknown until the problem as a whole as been solved, the boundaries of the system in the (u, v) plane are all known except for the numerical values of the abscissae of E', A'.

The next step is that of finding another function of (u, v) whose actual values on the boundary

[12] The literal translation of the German "*hangquelle*" hardly seems as expressive as the term "surface of seepage."

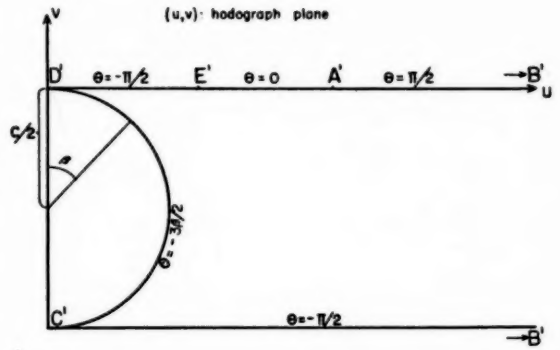

FIG. 2. The hodograph plane representation of Fig. 1.

segments can be preassigned. Such a function can be obtained as follows: Introducing first the complex potential,

$$f(z)=\Phi+i\Psi, \tag{9}$$

where Φ is the velocity potential and Ψ is the stream function, one proceeds to the intermediate potentials τ, θ defined by:

$$\tau+i\theta=-\log\{-f''(z)\}, \tag{10}$$

where since:

$$-f''(z)=\frac{(-d(f'(z))/dt}{dz/dt}=\frac{\dot{u}-i\dot{v}}{u+iv}=\frac{be^{-i\chi}}{ne^{i\omega}}, \tag{11}$$

$$\tau=\log n/b; \quad \theta=\omega+\chi, \tag{12}$$

where n, b are the absolute values of the velocity and acceleration and χ, ω are the inclinations of their directions. On the basis of these definitions it may be shown that the distribution of θ on the boundaries is that given in Fig. 2, where the angle β relating to the free surface has been defined by the relation:

$$u=c\sin\beta/2\cos\beta/2; \quad v=-c\sin^2\beta/2. \tag{13}$$

Before mapping the hodograph in the (u, v) plane on the infinite half-plane it is convenient to transform it first into the standard form of Fig. 3 obtained by applying the transformation function

$$q=1+(i/c)(u-iv), \tag{14}$$

giving the representation of Fig. 3.

The region B'' C'' D'' E'' A'' B'' in the q plane can now be mapped onto the upper half

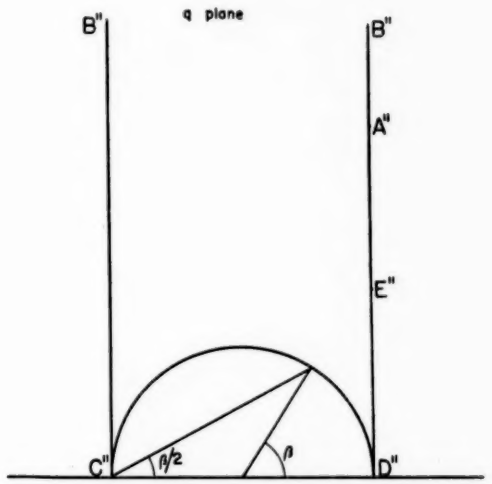

FIG. 3. The q plane diagram corresponding to Fig. 2.

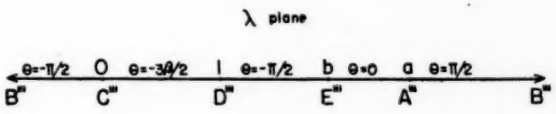

FIG. 4. The λ plane map of Fig. 3.

of the λ plane by means of the modular elliptic function $\lambda(q)$, this function being so chosen that:

$$\lambda(0)=0; \quad \lambda(1)=1; \quad \lambda(i\infty)=-\infty; \quad \lambda(1+i\infty)=+\infty, \tag{15}$$

giving the representation in Fig. 4.

As θ is known on the real axis of the λ plane, the complex function $\theta-i\tau$ may be expressed in the whole upper λ plane by the generalized Poisson integral:

$$\theta-i\tau=-i\tau_0+\frac{1}{\pi i}\int_{-\infty}^{+\infty}\frac{\theta(t)(\lambda t+1)dt}{(t-\lambda)(1+t^2)}, \tag{16}$$

where τ_0 is an arbitrary constant. Denoting now the values of λ corresponding to E''' and A''' by b and a, evaluating the integral of Eq. (16), and combining with Eq. (10), one finds:

$$f''(z)=-\left[\frac{(\lambda-b)(a-\lambda)\lambda}{\lambda-1}\right]^{\frac{1}{2}} \exp\left[-\tau_0+\frac{3}{2\pi}\int_0^1\frac{\beta(t)}{t-\lambda}dt\right]. \tag{17}$$

As $\lambda=\lambda(q)$ is a known function of $u-iv=-f'(z)$, it follows that $f''(z)=F(f'(z))$, and:

$$z=-\int\frac{d(u-iv)}{F(u-iv)}=\int e^{\tau+i\theta}d(u-iv)$$

$$=C\int\left[\frac{\lambda-1}{\lambda(a-\lambda)(\lambda-b)}\right]^{\frac{1}{2}}$$

$$\exp\left[-\frac{3}{2\pi}\int_0^1\frac{\beta(t)}{t-\lambda}dt\right]d(u-iv), \quad (18)$$

where $C=e^{\tau_0}$, and the sign of the radical for real λ is to be taken as that of $e^{-i\theta}$. Thus, in principle, the problem is solved, as by Eq. (18), z is given as the function of $u-iv$, and hence the velocity components as functions of z.

Specific Calculations

The physical content of the analytical solution contained in Eq. (18) may be obtained by the evaluation of the geometrical dimensions of the flow system as implied by the constants a and b, the determination of the shape of the free surface, the computation of the velocity distributions along the boundaries, the calculation of the total flux through the system, and the mapping of the potential and streamline distributions in the system. The specific expressions giving these results are readily seen to be the following equations, taking note of the values of θ indicated in Fig. 2, and setting the constant C equal to unity:

(a) Velocity distribution ($x=x(u)$) along EA, its length L, and the fluid head distribution head $h(x)$:

$$x(EA)=\int_{u(E)}^{u}e^{\tau}du; \quad L=\int_{u(E)}^{u(A)}e^{\tau}du, \quad (19)$$

$$h(x)=h_e-\int_0^x udx=h_e-\int_{u(E)}^{u}ue^{\tau}du. \quad (20)$$

(b) Velocity distribution ($y_w=y_w(u)$) along the outlet face AB, and the outlet fluid height h_w:

$$y_w=\int_{u(A)}^{u}e^{\tau}du; \quad h_w=\int_{u(A)}^{\infty}e^{\tau}du. \quad (21)$$

(c) Velocity distribution ($y_s=y_s(u)$) along the surface of seepage BC, and the length h_s of BC:

$$y_s=-\int_{u(B)}^{u}e^{\tau}du; \quad h_s=-\int_{\infty}^{0}e^{\tau}du. \quad (22)$$

(c) The shape of and velocity distribution ($x=x(u, v)$), ($y=y(u, v)$) along the free surface CD:

$$z-z_c=x-L+i(y-h_w-h_s)$$

$$=\int e^{\tau-3i\beta/2}d(u-iv)=\frac{C}{2}\int_{\pi}^{\beta}e^{\tau-i\beta/2}d\beta. \quad (23)$$

(e) Velocity distribution ($y_e=y_e(u)$) along the inflow surface, and the inflow fluid height h_e:

$$y_e=-\int_{u(E)}^{u}e^{\tau}du; \quad h_e=-\int_{u(E)}^{0}e^{\tau}du. \quad (24)$$

A convenient check between the computation of h_e and h_w is obtained from Eq. (20) in the relation:

$$h_e-h_w=\int_0^L udx=\int_{u(E)}^{u(A)}ue^{\tau}du. \quad (25)$$

(f) Total flux, Q, through the system:

$$Q=\int_0^{h_e}udy_e=-\int_{u(E)}^{0}ue^{\tau}du=\int_0^{h_w}udy_w$$

$$+\int_0^{h_s}udy_s=\int_{u(A)}^{\infty}ue^{\tau}du-\int_{\infty}^{0}ue^{\tau}du. \quad (26)$$

(g) To find analytically the potential and streamline distributions in the interior of the system would require the general evaluation of the integral of Eq. (18) so as to first get the internal velocity distribution and then $\Phi(x, y)$ by integration. However, the most rapid and convenient procedure would probably be to find $\Phi(x, y)$ by standard numerical or graphical methods for solving Laplace's equation after having determined the shape of the free surface by Eq. (23) and the values of Φ along EA by Eq. (20).[13]

[13] A still more rapid empirical method of finding the shape of the free surface and the internal potential distribution, and one applicable to systems for which the analysis would be quite intractable, is that based on the electrical analogy of the fluid flow through a porous medium (cf. R. D. Wyckoff and D. W. Reed, this issue).

On the other hand, from a practical point of view, the most important feature of the solution is the relation of the total flux, Q, through the dam to the inlet and outflow heads h_e, h_w. We shall, therefore, stress mainly this phase of the solution, and present the other results as they are derived incidentally to the calculation of Q.

In order, however, to get any numerical results at all, it is necessary to determine the value of the integrand in Eq. (18). Here, it must first be noticed that whereas the modular elliptic function $\lambda(q)$ has been defined by Eq. (15), its properties are usually given in terms of the function $\bar{k}^2=\theta(q)$ defined by the conditions:

$$\Theta(0)=1; \quad \Theta(1)=\infty;$$
$$\Theta(i\infty)=0; \quad \Theta(1+i\infty)=0, \quad (27)$$

from which it is seen that

$$\lambda(q)=1-1/\Theta(q)=\Theta(1-1/q), \quad (28)$$

which can be expanded by the rules already established for the function Θ. This relation affords the link between the variable λ, entering in the integrand e^{τ} of Eq. (18) and the variable of integration $u-iv=-ci(q-1)$, and thus also permits changing the variable of integration from $u-iv$ to λ.

Finally, one must evaluate the integral:

$$\alpha(\lambda)=-\frac{3}{2\pi}\int_0^1 \frac{\beta(t)}{t-\lambda}dt. \quad (29)$$

This may be done by noting that the variable t in Eq. (16) really represents the real axis of the λ plane on which the q plane of Fig. 3 is mapped by the function $\lambda(q)$. Hence:

$$t=\lambda(q)=\lambda(\tfrac{1}{2}+e^{i\beta}/2)=\Theta(1-1/q)$$
$$=\Theta(i\tan\beta/2)=\bar{k}^2, \quad (30)$$

from which β can be computed as a function of t.

The evaluation of $\alpha(\lambda)$ for $1.05\leq\lambda\leq 20$ and $-20\leq\lambda\leq -0.01$ has been carried out by Gunther,[14] using direct graphical integration. However, in evaluating the height h_e by Eq. (24) and the flux Q by the first of Eq. (26)—the simplest methods if one is to avoid computing in detail the shape of the free surface—it is necessary to know the values of α for λ much closer to 1, as in the variable of integration u, $\lambda=1.05$ corresponds to $u/c=0.5423$ whereas the integration has to be extended to $u=0$ (cf. Eq. (24)). Since $\lambda=1$ is a singularity of $\alpha(\lambda)$,—$\alpha(\lambda\sim 1)\sim 3\log\log(\lambda-1)$—graphical methods are inaccurate. An analytic expansion for very small $\eta=\lambda-1$, was, therefore, derived as follows: From the definition of α it is seen that:

$$\frac{-2\pi}{3}\alpha=\int_0^1\frac{\beta(t)dt}{t-\lambda}=\pi\log\frac{\eta}{\eta+1}+\int_{0.01}^1\frac{\beta(t)dt}{t}+\int_0^{0.01}\frac{\beta(t)}{t+\eta}dt+0\left(\frac{\eta}{0.01}\right), \quad (31)$$

use being made of the relation:

$$\beta(t)=\pi-\beta(1-t), \quad (32)$$

and the expansion of $(t+\eta)^{-1}$ in the first integral being replaced by t^{-1}. A graphical integration of this integral gave the value 8.926. In the remaining integral, $\beta(t)$ was expanded as:

$$\frac{\beta(t)}{2}=\tan^{-1}\frac{1}{\pi}\left(\log\frac{16}{t}-\frac{t}{2}\right)=\frac{\pi}{2}-\frac{\pi}{\log 16-t/2-\log t}+\frac{\pi^3}{3(\log 16-t/2-\log t)^3}-\cdots, \quad (33)$$

the argument of the arctangent being accurate to terms in t^2. By replacing $\log 16-t/2$ by: $\log 16-0.0025\equiv\log\delta$, the integral in question reduced to a series involving the integral:

$$I=-\int_0^{0.01/\delta}\frac{dz}{(z+\eta/\delta)\log z}, \quad (34)$$

and its derivatives with respect to $\log\delta$.

[14] In the manuscript already cited, reference 10.

I was then evaluated by dividing into the ranges $0\rightarrow\eta/\delta$ and $\eta/\delta\rightarrow 0.01/\delta$, and expanding the factors $(z+\eta/\delta)^{-1}$. The final result was found to be:

$$\frac{-2\pi}{3}\alpha=\pi\log(\eta+0.01)+\int_{0.01}^{1}\frac{\beta(z)}{z}dz+2\pi\log\log\frac{0.01}{\delta}+\frac{\pi^3}{3(\log 100\delta)^2}-\frac{\pi^5}{10(\log 100\delta)^4}-2\pi\log\log\frac{\eta}{\delta}$$

$$+0(100\eta)+0\left(\frac{1}{\log^6\eta/\delta}\right)=7.1927-2\pi\log\{\log 1/\eta+2.7701\},\quad(35)$$

which is accurate to about 10^{-4} up to $\eta=10^{-6}$.

Fig. 5 gives a plot of e^{α} as a function of $-\log(\lambda-1)$, the scale and coordinates being chosen so as to permit a representation of e^{α} to reasonably small values of u, the value of $-\log(\lambda-1)=27.63$ corresponding to $u/c=0.1033$, although $\lambda-1=10^{-12}$. The scale becomes quite unsatisfactory for $\lambda>2$; but for such values, e^{α} is listed by Hamel and Gunther.

For large values of λ, e^{α} is most conveniently obtained by expanding $(t-\lambda)$ in the integrand of α and evaluating the resultant integrals graphically. In this way it is found that:

$$e^{\alpha}=e^{3/4\lambda+0.3286/\lambda^2+0.2029/\lambda^3+\cdots}.\quad(36)$$

Finally, the values of e^{α} for $\lambda<0$ can be obtained from those for $\lambda>0$ by the formula:

$$e^{\alpha}(\lambda)=[-\lambda/(1-\lambda)]^{\frac{1}{2}}e^{\alpha}(1-\lambda),\quad(37)$$

as may be readily shown by changing the variable in the integral for α and then applying Eq. (32).

The connection between λ, the argument of e^{α} and hence of e^{τ}, and the variable of integration u occurring in Eqs. (19) to (26), may be made as follows: From the theory of the modular elliptic functions $\Theta(\xi)=\bar{k}^2$, it has been shown[15] that Θ may be inverted as:

$$\pi i\xi=-\frac{\pi K'}{K}\equiv G(\bar{k}^2)$$

$$=2\log\frac{\bar{k}}{4}+\frac{\bar{k}^2}{2}+\frac{13\bar{k}^4}{64}+\frac{32}{192}\bar{k}^6+\cdots,\quad(38)$$

where K, K' are the complete elliptic integrals of the first kind, with modulus $\bar{k}$[16] and $\bar{k}'$, respectively, the individual values as well as their ratio being listed in complete form by Hayashi.[17] Noting now the relation between λ and Θ as given by Eqs. (28) and (30), and the transformation formulas between the function $\Theta[(m'+n'\xi)/(m+n\xi)]$, m, m', n, n' being integers of mod. 2, and $\Theta(\xi)$,[18] we readily find that for:

$$-\infty<\lambda\leq 0,$$

$$\bar{k}^2=\Theta(q)=\frac{1}{1-\lambda};\quad \pi iq=-\frac{\pi K'}{K}=G\left(\frac{1}{1-\lambda}\right),\quad(39)$$

so that, noting that for $\lambda<0$, $v=-c$, $q=iu/c$,

$$u/c=K'/K=(-1/\pi)G(1/(1-\lambda));$$

or:

$$\bar{k}^2=\Theta\left(\frac{1}{-q}\right)=\frac{\lambda}{\lambda-1};$$

$$\frac{c}{u}=\frac{K'}{K}=\frac{-1}{\pi}G\left(\frac{\lambda}{\lambda-1}\right).\quad(40)$$

Similarly, for: $0\leq\lambda\leq 1$, $\bar{k}^2$ may be taken as $1-\lambda$ or λ, so that:

$$\frac{\pi iq}{1-q}=-\frac{\pi K'}{K}=G(1-\lambda);$$

$$\text{or}\qquad \pi i\frac{(q-1)}{q}=-\frac{\pi K'}{K}=G(\lambda);\quad(41)$$

[15] Cf. H. A. Schwarz, *Formeln und Lehrsatze zum Gebrauche der Elliptichen Functionen*, §40.

[16] The modulus of the elliptic integral K is here taken as $\bar{k}$ in order to avoid confusion with the symbol k already used to denote the permeability of the porous medium (cf. Eq. (1)).

[17] K. Hayashi, *Tafeln der Besselschen, Theta-, Kugel-, und anderer Functionen*, 1930.

[18] Schwarz, reference 15, §§33, 54.

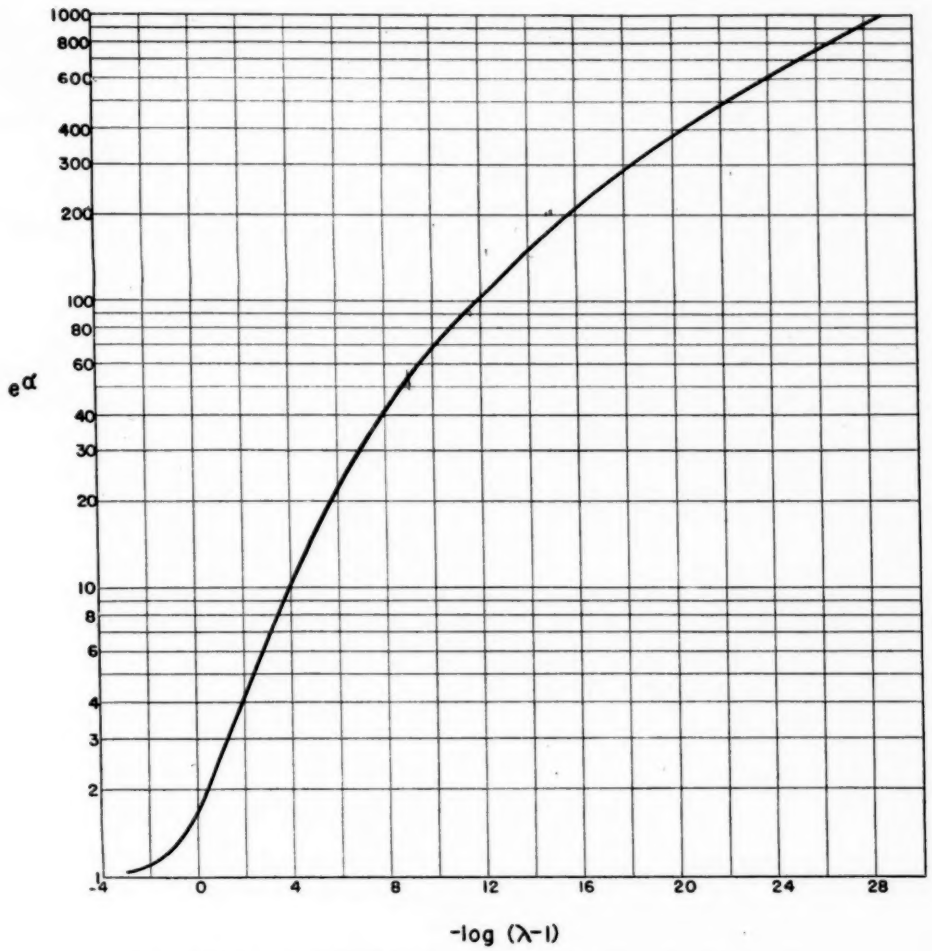

FIG. 5. Plot of e^{α}, defined by Eq. (29), as a function of $-\log(\lambda-1)$.

and, for: $1 \leqq \lambda \leqq \infty$, $\bar{k}^2$ may be taken as $1/\lambda$ or $(\lambda-1)/\lambda$, so that:

$$\frac{u}{c}=\frac{K'}{K}=\frac{-1}{\pi}G\left(\frac{1}{\lambda}\right);$$

or

$$\frac{c}{u}=\frac{K'}{K}=\frac{-1}{\pi}G\left(\frac{\lambda-1}{\lambda}\right). \qquad (42)$$

With the aid of these relations the actual integrations in Eqs. (19) to (26) may be most readily carried out for finite values of λ and for values not too close to singular points of e^{τ} by plotting e^{τ} as a function of u/c and integrating graphically. In evaluating the integrals for infinite values of u or λ, the integration in u beyond 2.8604 $c(\lambda=500)$ was carried out analytically in the variable λ with the aid of the approximations:

$$e^{\tau}=[(\lambda-1)/\lambda(\lambda-a)(\lambda-b)]^{\frac{1}{2}}e^{\alpha} \leqq 1.001/\lambda,$$
$$u \leqq (c/\pi)\{-1/2\lambda+\log 16\lambda\}; \quad du/d\lambda \leqq c/\pi\lambda, \qquad (43)^{19}$$

the latter two equations following from the first of Eqs. (42). For the integrations at the singular points, as $\lambda=b$, the evaluations were again carried out analytically from $\lambda=b$ to $\lambda=b$ plus 0.01 or 0.05 by replacing everything in the integrand except $(\lambda-b)^{-\frac{1}{2}}$ by its average over the interval of integration. In spite of the graphical and numerical character of the work

[19] These approximations are the same as those used by Hamel and Gunther.

it is felt that the errors in the final results should not exceed 1 percent.

For the four cases computed with vanishing outflow fluid level, which correspond to $a=\infty$, the factor $(a-\lambda)$ in the above expressions was omitted. That this is necessary may be readily shown by repeating the analysis leading to Eq. (18). Eqs. (19) to (26) remain unchanged except that $u(A)$ must be replaced by $\infty = u(B)$.

Results

The calculations were carried out in the manner described above for the six cases defined by the values of a and b, given in the second and third rows of Table I. The results are listed in the succeeding rows. The values of Q in this table have been computed by means of the first of Eq. (26). An indication of the accuracy of the calculation of this quantity is given by the fact that for case I, Q/c^2 was found to be 0.2988 by the 3rd and 0.2979 by the last of Eq. (26). The values of h_e/c or $(h_e-h_w)/c$ were also checked by means of Eq. (25) in all cases except II, where Eq. (25) was used to obtain h_w/c, the difference between the values given by Eq. (24) and Eq. (25) always being less than 1 percent. The value of $\bar{Q}/c^2$ are those computed by the formula analogous to Eq. (2), applying to linear flow, namely:

$$\bar{Q}=(k\gamma g/\mu)(h_e^2-h_w^2)/2L, \qquad (44)$$

which follows both from the Dupuit assumptions and the generalized interpretation of Eq. (3) as given by Wyckoff, Botset and Muskat.

The shape of the free surface (calculated by Hamel and Gunther) and the velocity distributions along the inflow and outflow surfaces as well as along the base are shown for case I in Fig. 6. For cases II–VI, neither the shape of the free surfaces nor velocity distribution along the outlet faces were computed. However, the heights at C of the surface of seepage were calculated, and at least a rough idea of the actual free surface should be given by the free surfaces arbitrarily drawn in the Figs. 7, 8 and 9 for cases II, III, and VI, following the general features indicated by that for case I. The velocity distributions along the inflow faces and the bases for these other cases are given in Figs. 7 to 9.[20] These figures also contain the pressure distribution (calculated by Eq. (20)) along the base, and for comparison those, $\bar{p}$, implied by the solution of Eq. (3), namely:

$$\bar{p}^2=-(h_e^2-h_w^2)x/L+h_e^2. \qquad (45)$$

Table I.

Case	I	II	III	IV	V	VI
b	5	2	10	5	2	1.2
a	10	5	∞	∞	∞	∞
h_e/c	0.3223	0.6695	0.67204	0.8715	1.2857	1.8234
h_w/c	0.0842	0.1579	0	0	0	0
h_s/c	0.1225	0.2019	0.4300	0.5192	0.6455	0.7185
L/c	0.1619	0.4439	0.3293	0.4843	0.9063	1.6923
Q/c^2	0.3015	0.4802	0.6871	0.7828	0.9129	0.9830
$\bar{Q}/c^2$	0.2989	0.4768	0.6865	0.7841	0.9120	0.9823

Discussion

Although the above results are essentially numerical and include only six cases of a single type of gravity flow problem, they nevertheless imply some important consequences which should be of significance with respect to other gravity flow systems. First, however, one may note some of the features of the free surface, for case I, shown in Fig. 6. Thus, on noting from Eq. (13) that the inclination of the free surface is simply $\beta/2$, it follows from Eq. (23) that the slope of the free surface decreases monatonically from zero at the inflow face at D to a negatively infinite[21] value at the surface of seepage at C. Furthermore, Fig. 6 shows that the actual heights of the free surface may be very much different from those computed by Eq. (3) with y interpreted as the fluid height—which would be

[20] The same data as indicated in Figs. 7 to 9 were also computed for cases IV and V, but their similarity to those shown makes their reproduction unnecessary. The discrepancy between the dimensions shown in Fig. 9 and those given in Table I is due to an error in the calculations discovered after the figure was drawn and sent in.

[21] The statement by Wyckoff, Botset and Muskat (reference 6) that the slope can never exceed 45° was based on the erroneous assumption that the horizontal velocity component at the free surface would increase monatonically in approaching the outflow surface. However, this does not invalidate their conclusion that the horizontal velocity component at the free surface can never exceed half of the vertical free fall velocity, c. It may also be noted that the free surface will always become tangential to the outflow face as it joins the surface of seepage, as long as the inclination of the outflow face equals or exceeds 90°.

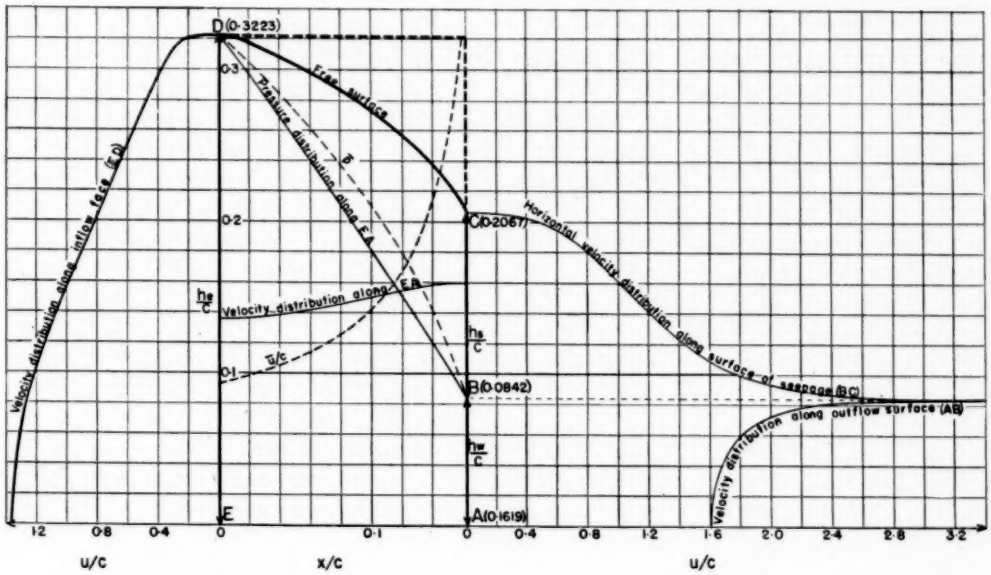

FIG. 6. Free surface, velocity, and pressure distribution for a dam defined by: $b=5$, $a=10$, case I. $\bar{u}/c$ and $\bar{p}$ are the pressure and velocity distributions implied by Eq. (45). The velocities along EA have been reduced by a factor of 10.

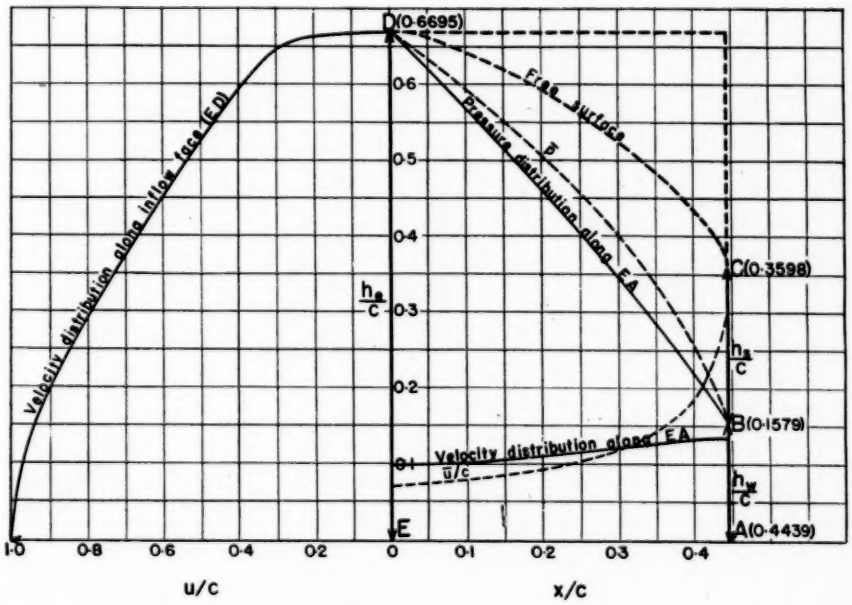

FIG. 7. Velocity and pressure distributions for a dam defined by: $b=2$, $a=5$, case II. $\bar{u}/c$, and $\bar{p}$ are those implied by Eq. (45). The free surface was drawn in, without calculation, so as to terminate at C. The velocity distributions along EA have been reduced by a factor of 10.

given by the curve marked $\bar{p}$—as originally suggested by Dupuit and used at length by Forchheimer. Especially in such cases as III–VI where the outflow fluid head is zero, Eq. (3) would also give vanishing fluid *heights* near the outflow surface, whereas the actual outflow heights as given by h_s may become quite large fractions of h_e (for III, $h_s/h_e=0.64$). Although these discrepancies rapidly decrease as one recedes from the outflow surface, and should also be smaller at distant points in radial systems than in linear systems, it does seem difficult to

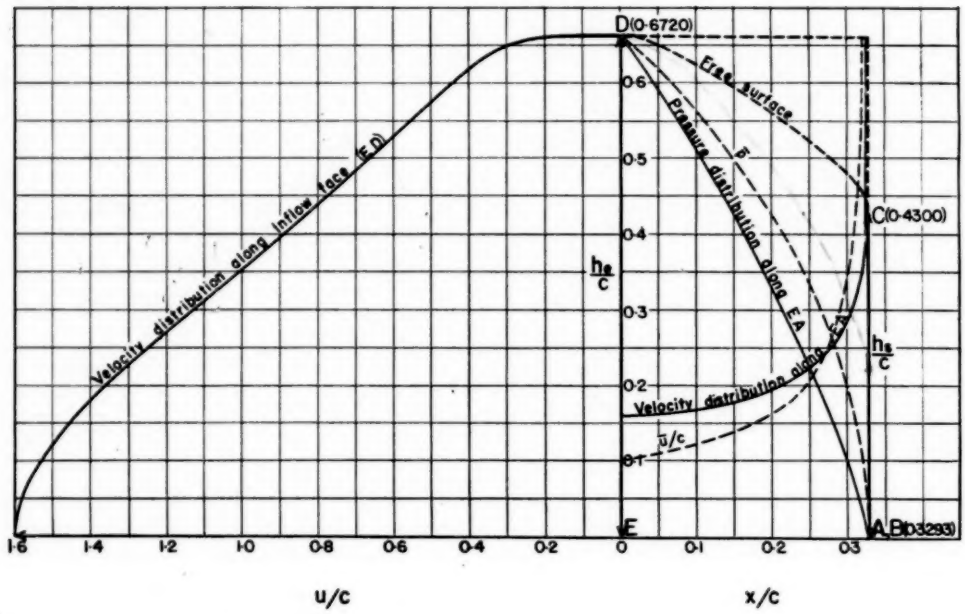

FIG. 8. Same as Fig. 7, with $b=10$, $a=\infty$, case III.

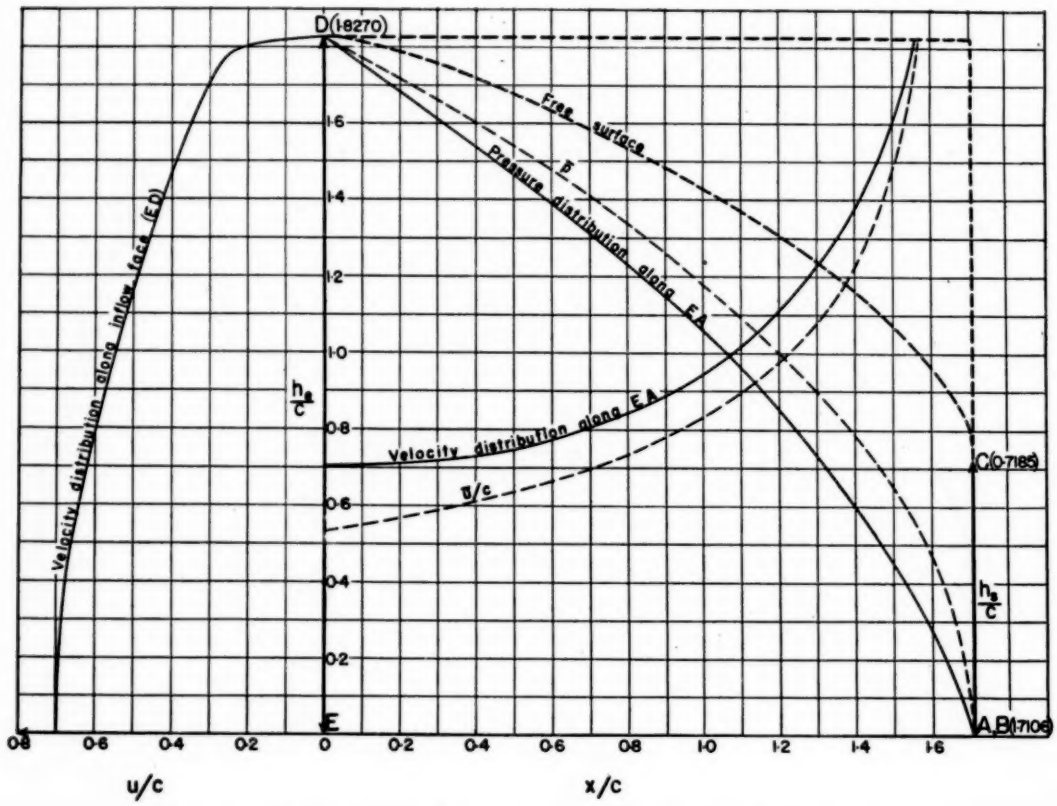

FIG. 9. Same as Fig. 7, with $b=1.2$, $a=\infty$, case VI.

maintain that the Dupuit-Forchheimer predictions of the shapes of free surfaces are more reliable than reasonable guesses, except at points where the slopes of the free surfaces are definitely known to be small.

These serious discrepancies must evidently result from erroneous assumptions. That the Dupuit assumption of "shell flow"—uniformity with depth of the horizontal velocity—is fallacious, is clearly shown by the velocity distribution curves of Figs. 6 to 9. Obviously the velocity variation from 0 at D to the maxima at E can be put poorly approximated by a uniform velocity distribution.[22] Similarly, the variation of u/c along AB in Fig. 6 from a minimum at A to ∞ at B is hardly suggestive of any essential uniformity, even though the region of indefinitely large growth of the velocity is quite limited. Finally, the surface of seepage BC, which is entirely neglected in the Dupuit-Forchheimer theory, also possesses a range of infinitely high velocities. In fact, in case I, the flow through BC happens to be almost exactly equal to that through AB, and in such cases as III–VI where $h_w=0$, the total flow must, of course, pass through BC. It is, therefore, clear that the Dupuit-Forchheimer basic assumptions and interpretation of Eq. (3) as a differential equation for the free surfaces of gravity flow systems must be used with great caution if entirely erroneous results are to be avoided.

The interpretation of Wyckoff, Botset and Muskat[6] of Eq. (3) as a differential equation for the pressure distribution at the base (horizontal) of a gravity flow system also seems to be subject to considerable error. For, as will be seen from Figs. 6 to 9, the pressure distributions, $\bar{p}$, implied by this interpretation, differ quite appreciably from that given by the rigorous theory. The discrepancies are particularly marked near the outflow faces if $h_w=0$ (Figs. 8 and 9), where Eq. (45) leads to a velocity that becomes infinite as $x^{-\frac{1}{2}}$, x being the distance from the outflow end, whereas the exact analysis requires a logarithmic infinity for u. As a whole, it will be noted that the actual pressure distributions at the base are much more linear than is implied by Eq. (45).

While this result may appear surprising in view of the close agreement found by Wyckoff, Botset and Muskat between the predictions of Eq. (3) and the pressure distributions obtained from actual sand model experiments of radial flow systems, the reason undoubtedly lies in the differences in geometry of the systems. Thus in the radial system, where the effective resistance is largely concentrated near the outflow surface, a distortion of the geometry in this region, such as is caused by the shrinkage of the actual height of sand through which liquid is flowing due to the depression of the free surface,[23] might well result in a marked modification of the pressure or fluid head distribution (even at the base) from that in a strictly nongravity radial system, namely:

$$h=\frac{(h_e-h_w)\log r/r_w}{\log r_e/r_w}+h_w. \qquad (46)$$

And indeed, it was found there that the observed pressure distribution could be expressed by:

$$h^2=\frac{(h_e^2-h_w^2)\log r/r}{\log r_e/r_w}+h_w^2. \qquad (47)$$

However, in the case of the linear flow system, the region near the outflow surface is no more sensitive to distortions in geometry than any other part of the sand, and is moreover not at all as sensitive as that in a radial flow system. Hence the effect on the pressure distribution of the depression of the free surface will necessarily be smaller, and it will be only slightly modified from that in the strictly linear system, except where $h_w=0$ and infinitely high velocities are thus necessarily induced. It is, therefore, not unreasonable that Eq. (45), which is based upon the extrapolation of the effect of gravity observed for radial flow—the change from Eq. (46) to Eq. (47)—should be found to give too large a modification in the case of linear flow.

[22] In fact, if the Dupuit method is followed to its logical conclusion, and one uses for the average horizontal velocity along the vertical section its actual value at the free surface, the absurd value of zero flux would be obtained when this procedure is applied to either the inflow or outflow surface.

[23] The shrinkage of the cross-sectional area due to the depression of the free surface has the same *type* of effect as decreasing the permeability of the sand.

Although these considerations seem to leave Eq. (3), even with the interpretation of y as a fluid head, restricted essentially to radial systems, it, strangely enough, retains its significance in providing a satisfactory method for computing the *flux* in gravity flow systems, a knowledge of which is of even greater practical importance in the discussion of gravity flow systems than the shape of the free surface. For not only was Eq. (2), which is a consequence of Eq. (3) for radial flow, verified directly and empirically in the course of the establishment of Eq. (47), but a comparison of the last two rows in Table I shows that the linear flow implication of Eq. (3) also checks satisfactorily, for practical purposes, the correct values (Q/c^2). Thus, while the calculations carried out here definitely disprove the validity of Eq. (3) for giving either the fluid height distributions or the fluid head distributions (at the horizontal lower boundaries) in general gravity flow systems, they at the same time give strong support to the equation when used simply as a means of computing the flux through such systems, although it is difficult to find any rational explanation for the apparent cancelation of all the obvious errors in the solutions for the y's in such a way as to nevertheless give close approximations to the resultant fluxes. (See, however, the "note added in proof.")

The method for finding the flux from the solutions of Eq. (3) is simply contained in the equation:

$$Q=\frac{k\gamma g}{\mu}\int y\frac{\partial y}{\partial n}ds=\frac{k\gamma g}{2\mu}\int\frac{\partial y^2}{\partial n}ds, \qquad (48)$$

where the integral is extended over either the external or internal boundary of the system, with normal n, the solution y^2 of Eq. (3) being that which assumes the given values of h_w^2 and h_e^2, the squares of the fluid heads, at the outflow and inflow surfaces. This procedure will give the same numerical results as that of Dupuit,[24] although its only justification is that it gives values of Q which agree quite closely with those found either by direct experiments in the radial flow case or exact calculation in the simple case of linear flow.[25]

Summarizing, then, it appears that the calculations carried out here not only show the nature of the correct solution of two-dimensional gravity flow problems, but moreover they for the first time conclusively prove the inadequacy of previous approximate treatments and empirical generalizations with respect to the shapes of the free surfaces or pressure distributions within the gravity flow systems. Finally, they show at the same time that these earlier formal approximations do lead to predictions of the flux through gravity flow systems—at least for radial and linear systems—which are accurate to within one percent.

Note added in proof: A closer examination, made since this paper was submitted, of the physical significance of the second method, mentioned in footnote 25, of deriving Eqs. (2) and (44), has revealed the real reason for their success in giving a very close approximation to the flux through gravity flow systems. Thus if we replace the linear gravity flow system of Fig. 1 by one with exactly the same boundary conditions along the faces but without an upper free surface boundary, i.e., with the conditions: $y=0$, h_e : $\partial\Phi/\partial y=0$; $x=L$, $0\leq y\leq h_e$: $\Phi=ch_e$; $x=0$, $0\leq y\leq h_w$: $\Phi=ch_w$, and $h_w\leq y\leq h_e$: $\Phi=cy$, $(c=k\gamma g/\mu)$, it is readily found that:

$$\Phi=\frac{c}{2h_e}(h_e+h_w^2)+\frac{c}{2h_eL}(h_e^2-h_w^2)x$$
$$+\frac{2ch_e}{\pi^2}\sum_1^\infty\frac{\{(-1)^n-\cos(n\pi h_w/h_e)\}}{n^2\sinh(n\pi L/h_e)}\cdot\cos\frac{n\pi y}{h_e}\sinh\frac{n\pi(L-x)}{h_3}. \qquad (49)$$

[24] It is to be observed that derivations of Eqs. (2) and (43) by the Dupuit-Forchheimer theory involves the assumption, in addition to those mentioned in the introduction, that there is no surface of seepage. A consistent application of that theory would require that h_w in these equations should be replaced by h_w+h_s, and hence lead to results which do not agree either with the empirical or rigorously calculated values for the fluxes Q.

[25] It may be noted that both Eqs. (2) and (44) which follow from Eq. (48) might be intuitively constructed as rough approximations on the basis that they are equivalent to the values of Q that would be obtained from non-gravity flow systems of fluid head differential (h_e-h_w) and "average thickness" $(h_e+h_w)/2$, although the latter gross approximation would become immediately questionable when the existence of the surface of seepage, and hence outflow height of h_w+h_s, is recognized. A somewhat more satisfactory mode of intuitive approximation could be based on the observation that the actual average potential over an outflow surface, of total height h_e, which is faced by a free liquid reservoir to the height h_w, is $\bar{\Phi}_w=k\gamma g(h_e^2+h_w^2)/2h_e\mu$. Hence assuming a strictly nongravity flow through the total sand thickness h_e, but with an effective potential difference of $\Phi_e-\bar{\Phi}_w=k\gamma g(h_e^2-h_w^2)/2h_e\mu$, the same Eqs. (2) and (44) will again be obtained.

The flux corresponding to this Φ, or: $\int_0^{h_e}(\partial\Phi/\partial x)dy$ is evidently given by Eq. (44). Now as the real gravity flow system differs from that represented by the above Φ only in the corner near $x=0$, $y=h_e$, which lies above the actual free surface, but which is obviously a region of very small flux density, it is clear that one may justifiably expect that the flux in the approximation system (without the free surface), i.e., Eq. (44), should differ but slightly from that in the physical gravity flow system. And indeed this is verified by reference to the last two rows of Table I. Of course, it is evident from this rigorous derivation of Eq. (44) from the approximation system, that it should give values for the flux that are somewhat higher than those passing through the gravity flow system with its free surface. That the difference is, however, extremely small is shown by the fact that within the accuracy of the calculations (one percent) there appears to be no difference at all between the last two rows of Table I (the excess of Q/c^2 by one percent for case I must be due to numerical errors in the use of the first of Eqs. (26) for this case, as the last two of Eqs. (26) gave an average value even *less* than $\bar{Q}/c^2$). In fact, this is conclusively verified by the direct electrical model measurements of Wyckoff and Reed (cf. preceding paper) which showed, for case I, that the conductivity of the approximation system exceeds that of the real gravity flow system by no more than 1/4 percent. That the Dupuit-Forchheimer theory gives Eq. (44) must, therefore, be considered as entirely fortuitous, while its success as an approximation formula is to be attributed to the fact that it is the correct value of the flux through a system which, from *a priori* considerations, could really have been expected to give a very close approximation to that in the physical flow system.

Exactly the same type of approximation system for the case of radial flow (with circular boundaries: $r=r_w$, r_e) gives for the internal potential distribution:

$$\Phi = ch_e + \frac{c(h_e^2-h_w^2)}{2h_e \log(r_e/r_w)} \log\frac{r}{r_e} + \frac{2ch_e}{\pi^2}\sum_1^\infty \frac{|(-1)^n - \cos(n\pi h_w/h_e)|\, U(\alpha_n r)\cos(n\pi y/h_e)}{n^2 U(\alpha_n r_w)}, \quad (50)$$

where: $U(\alpha_n r) = I_0(n\pi r/h_e)K_0(n\pi r_e/h_e) - I_0(n\pi r_e/h_e)K_0(n\pi r/h_e)$,

and a flux identically the same as Eq. (2). Here, too, the error involved in retaining in the flow system the region above the actual free surface should be very slight, as was indeed found to be the case in the original sand model radial flow experiments (cf. reference 6), the fluxes in which were reproduced by Eq. (2) with an accuracy well within the experimental errors.

Finally, it may be noted that the above approximation systems not only give very close approximations to the flux in the physical gravity flow systems, but the pressure distributions at the bases have been found to be also satisfactorily reproduced by Eqs. (49) and (50). This is, of course, to be expected, as the mere presence of the free surface should not appreciably affect the potential distributions in parts of the flow system that are distant from it. This method of replacing the physical gravity flow system by those having the same boundary conditions, without the free surfaces, thus affords a relatively simple and fairly accurate means of studying all the significant features of the type of gravity flow system considered here excepting those directly related to the free surfaces themselves.

The author is indebted to Mr. R. D. Wyckoff for helpful discussions of this paper, to Mr. M. Meres for assistance with the calculations, and to Dr. P. D. Foote for permission to publish the paper. He also again wishes to thank Dr. Hamel for permitting him to see the calculations of Mr. E. Gunther before their publication.

Dielectric Properties of Anodic Layers in Aluminum Electrolytic Condensers

J. E. LILIENFELD, L. CHANDLER, JR. AND S. GOLDMAN, *Ergon Research Laboratories, Inc., Malden, Massachusetts*

(Received January 29, 1935)

With a new type of especially stable electrolytic capacitor, the dielectric properties of anodic layers are measured. The investigation shows that variations of the dielectric properties may be divided into two classes: lagging and nonlagging variations. Lagging variations, which include variations of the capacity and power factor with the operating voltages, are especially characteristic of anodic layers. They arise from the fact that the structure (organization) of layers adjusts itself with changes of the operating conditions to a new dynamic equilibrium, within a short transition period. On the other hand, in regard to variations of the capacity and power factor with frequency, which are nonlagging variations, anodic layers are similar to other composite dielectrics. An oscillographic study of harmonics is made which verifies the lagging nature of the changes of capacity with the operating voltages (a.c. and d.c.) and demonstrates for the first time the existence of a nonlagging variation of the a.c. conductivity with voltage.

INTRODUCTION

HIGHLY insulating anodic layers formed by an electrolytic process on aluminum are the dielectrics in the usual electrolytic condensers. Although these layers find extensive application in practice, the information which appears in the literature regarding their dielectric properties has many inconsistencies and contradictions. This is due partly to the type of experimental measuring methods which have been employed in earlier investigations, and partly to the lack of uniformity and stability of the specimens used. However, work done at this laboratory[1] has shown that anodic layers of a strictly defined and stable character can be made. Subsequently, by using such layers in conjunction with proper electrolytes and adopting new measuring methods, it has been possible to make a satisfactory study of their dielectric properties. This study is the subject matter of the present paper.

An anodic layer is fundamentally of a dynamic nature, and it is therefore important in a systematic classification of its dielectric properties to differentiate carefully between those effects which are instantaneous and those which occur only after an appreciable time lag. A lack of this distinction is responsible for much of the confusion which exists in the literature on the a.c. properties of anodic layers, and the way in which they are correlated with the d.c. properties. For example, if a d.c. potential is applied across an anodic layer, a current will flow which gradually decreases with time. However, the curve of current against time depends not only on the applied potential and on the formation voltage of the layer, but also on the past history of the layer. Thus the conductivity of an anodic layer is subject to continual change, depending on the conditions under which the layer is operated. (Deterioration effects.[2]) Such changes in conductivity are examples of what we call lagging effects. They occur gradually with time and indicate permanent changes in the anodic layer. On the other hand, if we measure the capacity of an anodic layer at 60 cycles and then at 1000 cycles, we find a difference in the two capacitance values. This, however, does not indicate a change in the layer, because if the capacity is immediately thereafter measured at 60 cycles, it will be substantially the same as before. The variation of capacity with frequency is an example of a nonlagging effect.

The properties of dielectrics as usually measured are of a nonlagging character. Lagging changes are, for the most part, peculiar to anodic layers, being due to their dynamic nature. Now, in order to obtain a coherent series of data on the dielectric properties of anodic layers, it is imperative to reduce all lagging changes to the utmost attainable minimum. Previous work of this laboratory has shown that lagging changes become more prominent as the concentration and mobility of the active OH^- ions in the electrolyte increase. This is true for both the electrolyte of formation and the electrolyte of operation of the layer. Therefore, the bulk of the experiments

[1] J. E. Lilienfeld, L. W. Appleton, W. M. Smith and J. K. Nieh, "Studies of Fully Organized Layers on Aluminum," Trans. Am. Electrochem. Soc. **61**, 531 (1932).

[2] J. E. Lilienfeld, L. W. Appleton and W. M. Smith, "The High Voltage Anodic Layer on Aluminum," Trans. Am. Electrochem. Soc. **58**, 225 (1930).

here presented have been conducted with layers formed in electrolytes of low OH^- concentration and operated in extremely viscous electrolytes of high specific resistance and low active OH^- concentration. These latter electrolytes will, in what follows, be termed "superviscous electrolytes." Their specific resistance is greater than 100,000 ohms/cm[3]. In order to keep down the effect of this high specific resistance in the power factor of the condenser as a whole,[3] extremely thin coatings of electrolyte have been used, according to a technique developed at this laboratory for practical condensers, U. S. Patent No. 1,986,779. With the use of such specimens, the dielectric properties of anodic layers have been investigated. In addition to the usual capacity and power factor measurements, a study has been made of the harmonics generated, to yield a clue to the law of variation with voltage, where such variation exists, of nonlagging changes of the capacity, power factor, and a.c. conductivity.

In experiments where a large percentage of harmonics has been desired, anodes formed and operated in decidedly alkaline aqueous electrolytes have been used, because they accentuate harmonics. As already mentioned, in such anodes lagging changes are also accentuated.

Although this paper is concerned with the purely physical investigation of anodic layers, the superviscous specimens used in it are also of interest because of the application of the principles embodied in their design to commercial electrolytic condensers in order to secure a high degree of stability and a relatively low power loss. This is desirable for a number of purposes, e.g., for continuous operation on a.c. circuits or on d.c. voltages which vary within very wide limits; inasmuch as less stable electrolytic condensers will be subject to a progressive deterioration if operated under these conditions.

Electrolyte Potential

An anodic layer can be studied by the usual methods designed for the investigation of good dielectrics only so long as it does not conduct appreciable current in either direction. This happens so long as the potential of the "formed" electrode with respect to the electrolyte does not exceed the formation voltage on the positive side or from 10 to 20 percent (depending on the specific manner in which the layer has been formed and treated) of the formation voltage on the negative side. If the potential exceeds either threshold there is a considerable passage of current. If the positive threshold is exceeded the layer may form to a higher voltage or may break down completely, while if the negative threshold is exceeded the layer will become highly conducting. Therefore, if an electrolytic condenser is made up of a formed anode and a nonpolarizable cathode and is operated on an alternating potential whose peak value is near that of the formation voltage, it will act as a rectifier. To prevent this, two formed anodes have to be used as shown in Fig. 1(A). This arrangement automatically biases the electrolyte at a negative value with respect to the average potential of the anodes and constitutes an a.c. electrolytic condenser whose capacitance is equal to the series capacitance of the two anodes. The potentials which exist in this case are shown in the oscillogram tracing of Fig. 1(A). From the picture it can be seen that just enough self-rectification has occurred so that the potential of the anode with respect to the electrolyte just about reaches its negative threshold value. This is the equilibrium condition, because if the threshold were exceeded, more rectification would take place.

A superior operating arrangement for many purposes, especially those of measurement, is shown in Fig. 1(B). This was first proposed by I. Moscicki.[4] In this arrangement a potential is imparted to the electrolyte by separate rectifiers and not by the self-rectifying action of the anodes. Assuming that the rectifiers (4) and (5) rectify at zero voltage, and assuming that the anodes (1) and (2) have identical capacity and power factor, the potential of the electrolyte with respect to the anodes will contain a d.c. component of half the peak value of the alternating voltage impressed across the anodes. This is the minimum value of the d.c. component. If either capacity or power factor or both are different for the two anodes, the direct component of the

[3] The power factor of an electrolytic condenser is due to the resistance of the electrolyte as well as the loss in the anodic layer. It is therefore desirable to keep the loss due to the resistance of the electrolyte as low as possible.

[4] U. S. Patent No. 926,128.

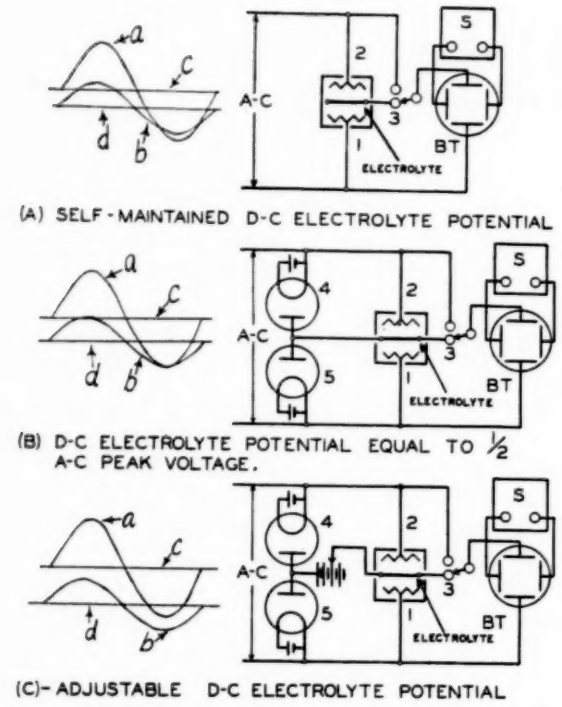

FIG. 1. Tracings of oscillograms of electrode potentials as observed in a circuit (110 v, 60 cycles) with various methods of operation. Oscillograms: (a) e_{12}, potential of anode 2 with respect to anode 1; (b) e_{13} equals potential of electrolyte with respect to anode 1. This is made up of $\frac{1}{2}e_{12}$ superimposed on the d.c. component of the electrolyte potential; (c) potential of anode 1; (d) d.c. component of electrolyte potential with respect to either anode. Circuit diagram: 1 and 2, formed anodes; 3, cathode; 4 and 5, vacuum tube rectifiers; *S*, sweep circuit; *BT*, Braun tube.

electrolyte potential will be higher than the half peak value, and will increase to the full peak value in the extreme case when the system is completely unbalanced.[5] In the present investigation, well-balanced (identical) anodes have been used in the positions (1) and (2) of Fig. 1(A), 1(B), and 1(C). In certain special cases where interaction between the two formed anodes is suspected, critical tests have been made in which one anode is replaced (in the electrical circuit) by a mica condenser and a series resistance.

Moscicki also suggested the introduction of an additional e.m.f. into his circuit which allows adjustment of the electrolyte potential to any desired level (Fig. 1(C)). Such an arrangement was used in part of the present investigation, in order to observe the effect of the bias of the electrolyte on the properties of anodes.

[5] It is interesting to note that the minimum setting of the electrolyte bias in the circuit of Fig. 1(B) can be used for accurate capacity and power factor measurements of electrolytic condensers. Compare J. E. Lilienfeld, U. S. Patent No. 1,931,460. An analytical treatment of this "rectifier bridge" is outside of the scope of the present paper, since the rectifier bridge was not used in any of the measurements reported in it.

TEST SPECIMENS

1. Superviscous specimens

Each test specimen representing one complete condenser consisted of two identical separate cells, made in accordance with the ideas described in U. S. Patent No. 1,986,779. The anode of each cell was made of a piece of aluminum foil $1\frac{3}{4}$ in. $\times 1\frac{3}{4}$ in. and 10 mils thick and provided with a tab. The anode was formed with a direct current to 200 volts in all the experiments here described, and was inserted between two slightly larger copper plates with a thin coating of superviscous electrolyte in between. The two copper plates of each condenser were interconnected to serve as its cathode. Two such identical condensers were operated in a circuit as shown in Fig. 1(A) in case no definite potential was imparted to the electrolyte, and otherwise in circuits as shown in Fig. 1(B) or Fig. 1(C).

2. Aqueous specimens

These consisted of two aluminum anodes $1\frac{3}{8}$ in. $\times 1\frac{7}{8}$ in. and 10 mils thick and a copper cathode of similar shape in between. All three electrodes were mounted on a Bakelite strip that was supported on the edge of a container and were immersed in an aqueous, decidedly alkaline, electrolyte. The direct formation voltage of these samples was 155 volts.

MEASUREMENTS

1. General method

We were concerned not only with capacity and power factor measurements, but also with a study of the current harmonics introduced by a condenser. In most of our work these current harmonics were so small as to be indiscernible in an oscillogram of the total current wave of the condenser; but, as we shall show later, important information could, nevertheless, be learned from them.

The arrangement sketched in Fig. 2 allowed us to obtain all the data presented in this paper

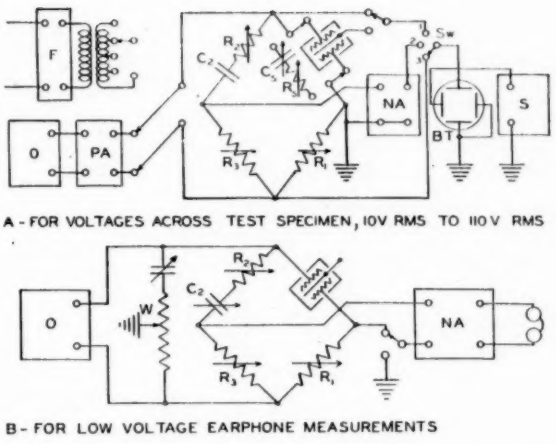

FIG. 2. Schematic diagram of measuring circuits. *F*, low pass 60-cycle filter; *O*, beat frequency audio oscillator; *PA*, 250-watt, audiofrequency power amplifier; *NA*, null arm amplifier; *BT*, Braun tube; *W*, Wagner ground; C_s, substitution resistance.

within limits of precision adequate for our requirements. The equipment consisted chiefly of a Wien bridge whose null arm voltage was amplified and observed on a General Electric Braun tube equipped with a linear sweep circuit, and of oscillators covering the range from 60 to 6000 cycles. Any harmonics present in the supply voltage were removed by filters. Consequently, all the harmonic voltages which were observed across the null arm of the bridge were due to nonlinear impedances.[6] The null arm amplifier had three resistance-capacity-coupled stages, having a voltage amplification adjustable from 0 to 450. As its amplification was uniform throughout the range of frequencies used, the magnitudes of small unknown input voltages were determined by substituting measured 60-cycle voltages adjusted to give the same deflection as the unknown voltage. The phase shift of the null-arm amplifier was constant and equal to 180 degrees from 150 to 8000 cycles. This was calibrated by means of Lissajous figures on the Braun tube. Since only the null arm voltage is amplified in each case, there is no amplifier phase shift correction to be applied to 60-cycle voltages appearing on oscillograms.

A great deal of the investigation was done by bridging over the capacity to be measured in Fig. 2 with a rectifier arrangement as shown in Figs. 1(B) and 1(C), in order to control the potential of the electrolyte. For obvious reasons, in the range of the capacities measured (>0.1 mf), the rectifiers should have had a negligible effect on the readings. This was confirmed by experiment. Critical tests made with good paper condensers, with and without the rectifier bridge, showed no difference in the readings to the first two digits even when the measured capacity was as small as 0.02 mf. No measurable effect was produced on paper condensers by varying the tap of the biasing battery between 0 and 149 v d.c. Variations of the r.m.s. a.c. voltage between 0 and 110 v produced no changes in the case of paper condensers, although distinct variations were obtained with electrolytic condensers.

2. Capacity and power factor measurements

To balance the bridge, when using the Braun tube, the circuit elements were varied until the fundamental disappeared on the oscillograph. Then, leaving the bridge settings unchanged, a decade mica condenser and a decade resistance were substituted for the test specimen and were adjusted until balance was again reached. The readings on the decade boxes then gave the effective capacitance and resistance of the test specimen.

When using the headphones, the capacity and power factor of the test specimen were determined from the bridge settings.

3. Harmonics

When the bridge was balanced for a sinusoidal voltage, harmonics—chiefly the third—were introduced by the electrolytic condenser and appeared across the null arm.[7] This null arm voltage, which was produced by the harmonic current through the condenser, amplified and viewed on the screen of the Braun tube, was photographed together with the voltage across the condenser and the total current through it, which was proportional to the drop across R_1 (Fig. 2(A)). Since the sweep frequency was synchronized with that of the voltage impressed

[6] A. Gemant, "Oszillographie der Ströme in Isolierstoffen," Archiv f. Electrotechnik **23**, 683.

[7] No such harmonics appear with the amplification used if the electrolytic condenser is replaced by a good mica condenser.

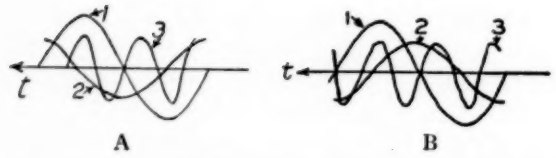

FIG. 3. Phase relation of current, voltage and third harmonic in a superviscous condenser. *A*, tracing of oscillograms as taken on the circuit shown in Fig. 2. *B*, oscillograms *A* redrawn with waves in correct phase relation. 1, voltage applied across condenser; 2, total current through condenser; 3, third harmonic null arm voltage.

on the bridge, photographs successively taken on the same film of voltage waves across the various circuit branches were shown in the same phase relation as if they were all taken simultaneously. On these photos, it had to be taken into account that the phase of the current through the condenser was shifted by 180°.

The impedance of the supply circuit was small in comparison with that of the $R_3C_2R_2$ branch. Therefore the third harmonic null-arm voltage was in phase with the voltage drop occasioned by the harmonic current through R_1, which was in phase with the harmonic current through the test specimen. The shifting of the switch, *Sw*, from position 1 to position 2 reverses the apparent phase of this harmonic voltage by 180°; but, since the null-arm amplifier has also shifted it by 180°, the picture of the third harmonic null-arm voltage shown in the photograph was in the same phase relation to the applied voltage across the condenser as the third harmonic current through the condenser. Thus oscillogram tracings such as shown in Fig. 3, reproduced within the limits of precision of the Braun tube, the correct phase relation between the applied voltage, the total condenser current, and the third harmonic condenser current, except that the total condenser current had to be shifted by 180°.

EXPERIMENTAL RESULTS

In Figs. 4 and 8 is shown the way in which the capacity and power factor of superviscous specimens vary with frequency. These variations are much larger than those observed in good mica condensers, but they are of the same order of magnitude and of the same general type as those observed in condensers with composite dielectrics, such as impregnated paper. For the

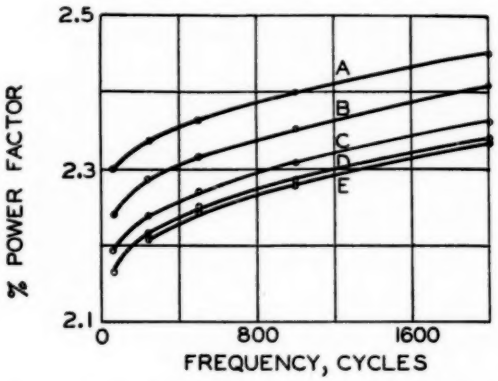

FIG. 4. Power factor of a superviscous condenser *vs.* frequency for a constant d.c. electrolyte potential of 80 v and variable a.c. voltages from 0.05 to 70 v r.m.s. (at 25°C). 80 v d.c. electrolyte potential; *A*, 70 v r.m.s.; *B*, 50 v r.m.s.; *C*, 30 v r.m.s.; *D*, 10 v r.m.s.; *E*, 0.05 v r.m.s.

convenience of practical calculations, it may be mentioned that variations of capacity with frequency over the range in question are closely approximated by the formula

$$C = C_0 + C_1 e^{-af}$$

as demonstrated in Fig. 9.

In the case of Fig. 4, it is more than likely that the part of the power loss which varies with frequency above 200 cycles is just that due to the resistance of the electrolyte. This is indicated by the parallelity of the curves, and the fact that they are practically straight lines in this region. The smallness of this variable part of the power factor indicates that the total resistance of the electrolyte is very low.

Figs. 5 and 10 show the variation of the capacity and power factor of superviscous condensers with the d.c. component of the electrolyte potential. Frequency and r.m.s. values of the a.c. voltage are parameters in these figures. The results show that the power factor varies but little with the biasing voltage of the electrolyte.[8] On the other hand, the capacity does vary by a few percent in the permissible range of the electrolyte potential. All these curves appear

[8] The biasing voltage can under no circumstances be allowed to exceed the formation voltage of 200 volts, because if it did, either the condenser would break down or additional layer would form and we would no longer be dealing with a 200-volt layer. In fact, the upper limit of the biasing voltage is little more than 200 volts minus one-half the peak of the a.c. voltage, because the layer becomes unstable when the formation voltage is substantially exceeded even in pulses.

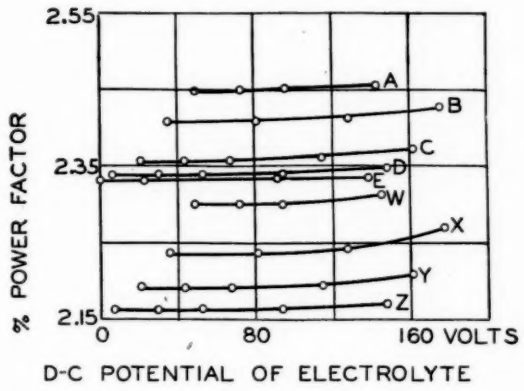

FIG. 5. Power factor of a superviscous condenser *vs.* d.c. potential of electrolyte with respect to anodes. Frequency and a.c. voltage are parameters (at 25°C). *A*, 2000 cycles, 70 v r.m.s.; *B*, 2000 cycles, 50 v r.m.s.; *C*, 2000 cycles, 30 v r.m.s.; *D*, 2000 cycles, 10 v r.m.s.; *E*, 2000 cycles, 0.05 v r.m.s.; *W*, 60 cycles, 70 v r.m.s.; *X*, 60 cycles, 50 v r.m.s.; *Y*, 60 cycles, 30 v r.m.s.; *Z*, 60 cycles, 10 v r.m.s.

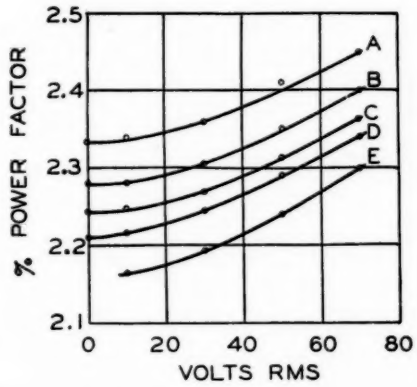

FIG. 6. Power factor of a superviscous condenser *vs.* a.c. voltage for a d.c. electrolyte potential of 80 v and frequencies from 60 to 2000 cycles (at 25°C). 80 v d.c. electrolyte potential; *A*, 2000 cycles; *B*, 1000 cycles; *C*, 500 cycles; *D*, 240 cycles; *E*, 60 cycles.

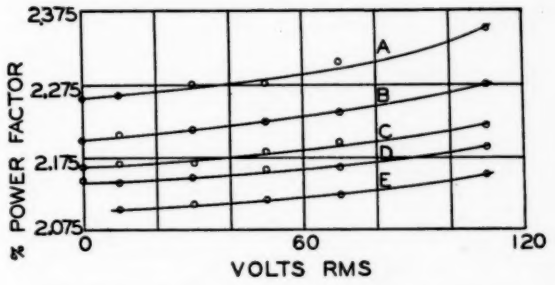

FIG. 7. Power factor of a superviscous condenser *vs.* a.c. voltage for frequencies from 60 to 2000 cycles with self-established electrolyte potential (at 25°C). *A*, 2000 cycles; *B*, 1000 cycles; *C*, 500 cycles; *D*, 240 cycles; *E*, 60 cycles.

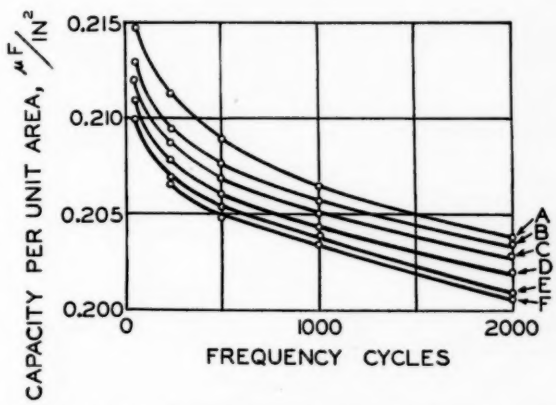

FIG. 8. Capacity of a superviscous condenser *vs.* frequency at fixed d.c. electrolyte potentials with a.c. voltage as parameter (at 25°C). *A*, 110 v r.m.s., 77.5 v d.c. electrolyte potential (½ a.c. peak voltage); *B*, 70 v r.m.s., 80 v d.c. electrolyte potential; *C*, 60 v r.m.s., 80 v d.c. electrolyte potential; *D*, 40 v r.m.s., 80 v d.c. electrolyte potential; *E*, 20 v r.m.s., 80 v d.c. electrolyte potential; *F*, 0.05 v r.m.s., 80 v d.c. electrolyte potential.

to have a characteristic minimum between 10 and 30 percent of the formation voltage. To the right of these minima, the variations are approximately controlled by a square law relation.

Figs. 6 and 11 show how the capacity and power factor of a layer vary with the r.m.s. a.c. voltage for a constant electrolyte potential. Frequency is the parameter in these figures. A rising characteristic with voltage is shown in each case. Figs. 7 and 12 are similar to Figs. 6 and 11, except that in obtaining the former the electrolyte has been allowed to establish its own bias. These curves are important because they picture the conditions under which practical condensers are usually operated.

It should be mentioned that the variations of the capacity and power factor with frequency are of a nonlagging type, but the variations of these with the electrolyte potential and the r.m.s. a.c. voltage are of a lagging character.

In Figs. 13–15 and Fig. 3, a study is made of the harmonics generated in electrolytic condensers. In Fig. 13 are shown oscillogram tracings at different frequencies, each showing the applied potential, the total condenser current and the amplified null-arm voltage. The latter gives a picture of the harmonics generated by the condenser. At 60 cycles there is practically a pure third harmonic. The third harmonic remains the preponderant component at all the frequencies

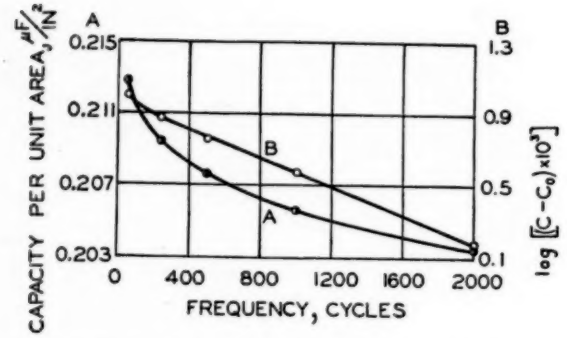

FIG. 9. Plot showing that the capacity per unit area, C, varies with the frequency, f, according to the relation, $C=C_0+C_1e^{-af}$. A, capacity per unit area *vs.* frequency; B, log $(C-C_0)\times10^3$ *vs.* frequency. C=capacity per unit area as a function of frequency. C_0=capacity at infinite frequency.

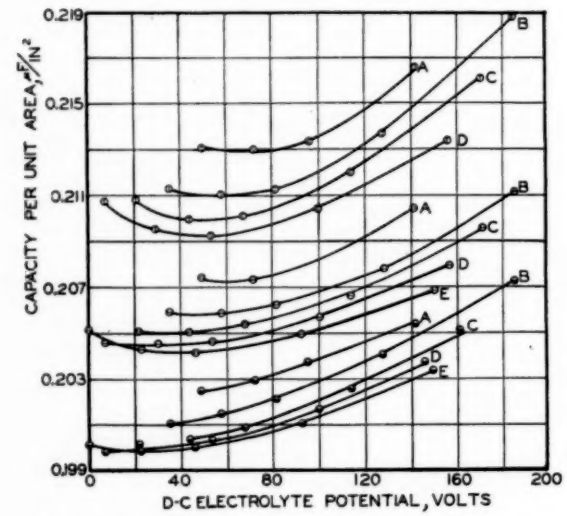

FIG. 10. Capacity per unit area of a superviscous condenser *vs.* d.c. electrolyte potential, with frequency and a.c. voltage as parameters (at 25°C). A, 70 v r.m.s.; B, 50 v r.m.s.; C, 30 v r.m.s.; D, 10 v r.m.s.; E, 0.05 v r.m.s. Circles with vertical line, 60 cycles; circles with horizontal line, 500 cycles; circles with lower half solid, 2000 cycles.

photographed, but other harmonics become more and more in evidence as the frequency is increased. By taking into account the amplification of the amplifier, measurements show that the amplitude of the harmonic current is roughly the same at all the frequencies in question. The curves of the total condenser current show that the harmonic current is very small in absolute magnitude, in fact of the same order as that observed in good impregnated paper condensers.

In Fig. 14 is shown that the amplitude of the third harmonic current is proportional to the

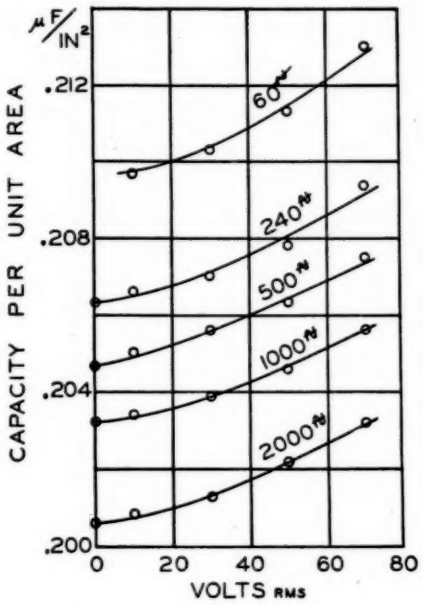

FIG. 11. Capacity of a superviscous condenser *vs.* a.c. voltage, for a d.c. electrolyte potential of 80 v with frequency as parameter (at 25°C).

cube of the applied voltage at 60 cycles. A similar relation holds at 240 cycles, and seems to hold even at higher frequencies, to the limited extent to which measurements can be made.

The percentage of harmonics varies with the electrolyte in which the layer is formed and operated. By using aqueous specimens with a wide range of OH^- concentrations, Fig. 15 is obtained. It shows that the percentage of harmonics is roughly proportional to the minimum formation current of the electrolyte.[9]

In Fig. 3 (A and B) are shown the phase relations between the voltage, total condenser current, and harmonic current in a superviscous specimen at 60 cycles. To a close approximation, the corrected curves of Fig. 3(B) indicate that

$$e=E\sin\omega t,$$
$$i=I_1\cos\omega t-I_3\sin 3\omega t,$$

where e and i are the total voltage and current,

[9] In a report to be published in Trans. Electrochem. Soc. October (1935), it is shown that for any "forming" electrolyte in which an aluminum anode is immersed, there is a critical current density at the $A1$ anode above which formation of the anode takes place. The value of this critical current density, which is called the *minimum formation current*, is independent of the voltage to which the anode has already been formed. The minimum formation current is approximately proportional to the OH^- concentration of the electrolyte.

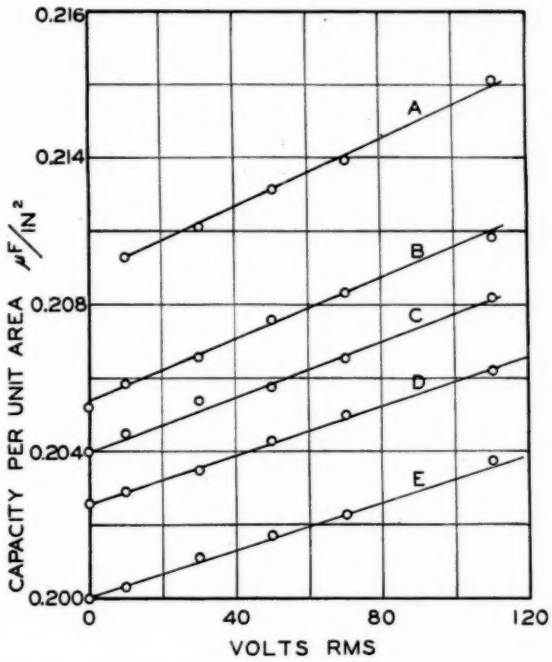

FIG. 12. Capacity *vs.* a.c. voltage for frequencies with self-maintained electrolyte potential (at 25°C). *A*, 60 cycles; *B*, 240 cycles; *C*, 500 cycles; *D*, 1000 cycles; *E*, 2000 cycles.

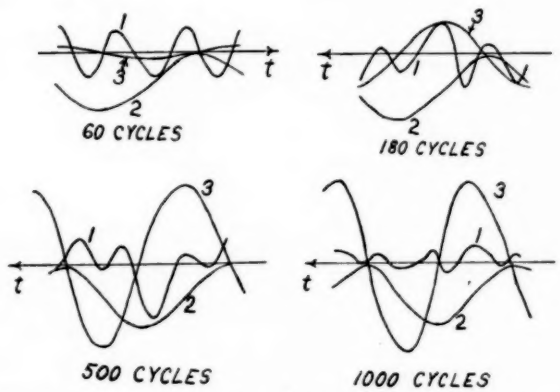

FIG. 13. Tracings of photographs showing the properties of the harmonic current through the condensers from 60 to 1000 cycles. 1, amplified null arm voltage (representing harmonic current); 2, voltage of electrolyte with respect to anodes; 3, total current through the condenser.

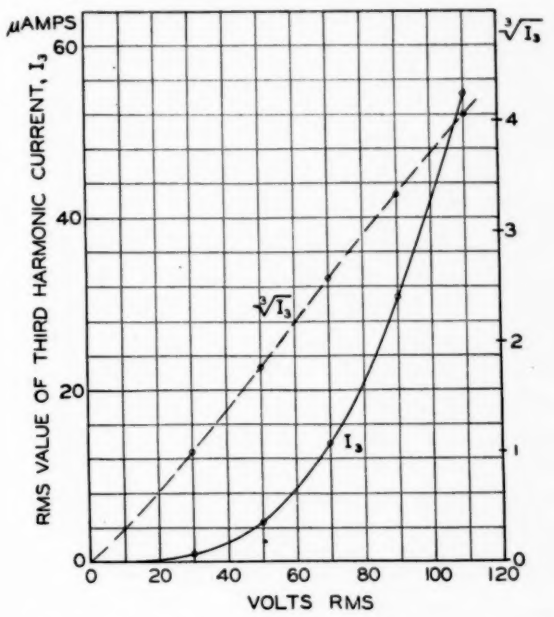

FIG. 14. Variation of third harmonic current and its cube root *vs.* applied voltage at 60 cycles for a superviscous condenser.

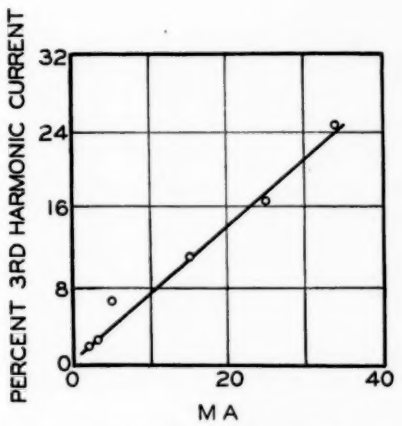

FIG. 15. Variation of the percentage of harmonics with the minimum formation current of the electrolyte (110 v r.m.s. at 60 cycles across the condenser).

respectively. Similar relations hold at higher frequencies, except for the increasing evidence of other harmonics.

THEORETICAL CONSIDERATIONS

Nonlagging effects

The frequency characteristics of capacity and power factor indicate that the dielectric of an anodic layer is similar in properties to other composite dielectrics.[10] Its characteristics fit in quite well with Maxwell's absorption theory as extended by K. W. Wagner.[11] The composite nature of the dielectric of an anodic layer is probably due to the occlusion of small amounts

[10] Compare F. W. Grover, Bull. Bur. Standards **7**, 495 (1911).

[11] J. B. Whitehead, *Lectures on Dielectric Theory and Insulation* (McGraw Hill, New York, 1927)—Lectures 6 and 7.

of aluminum hydroxide in the matrix of aluminum oxide.

In the section on harmonics, it will be shown that there is a nonlagging variation with voltage of the a.c. conductivity.

Lagging effects

The characteristics of anodic layers also present a class of phenomena peculiar to these layers and caused by their dynamic nature. These phenomena are lagging effects and indicate changes in the organization of the layer. They include the variation with a.c. and with d.c. voltage of the capacity and power factor. A detailed interpretation of these effects would be very difficult, pending a better knowledge of the ultimate factors which govern the capacity and power factor of anodic layers.

Harmonics

A diagram of a network equivalent to an anodic layer in a.c. operation is shown in Fig. 16, where C represents the capacity; R, the power factor; and G, the a.c. leakage conductance. Now, the presence of a preponderantly third harmonic in the harmonic current must be accounted for by a quadratic variation with voltage in one of these elements. A comparison of the experimental results with the results to be obtained by a variation of each of these factors separately, indicates that the quadratic variation occurs in the a.c. leakage conductance.

Let $$e=E\sin\omega t \qquad (1)$$

be the variable part of the e.m.f. impressed on the circuit of Fig. 16. Assume

$$G=G_0(1+ke^2), \qquad (2)$$

where G_0 may be a function of the biasing voltage.[12] Then

$$i=\frac{E\omega C}{1+R^2\omega^2C^2}\cos\omega t+\frac{ER\omega^2C^2}{1+R^2\omega^2C^2}\sin\omega t$$
$$+G_0E(1+\tfrac{3}{4}kE^2)\sin\omega t-G_0E\frac{3k}{4}\sin 3\omega t. \qquad (3)$$

Then, realizing that the second and third terms of the expression on the right are small in comparison with the first, we see that the above gives the correct phase relation between the harmonic current and total current. (Compare Fig. 3.) It likewise shows that the amplitude of the harmonic current should vary as the cube of the impressed a.c. voltage (compare Fig. 14) and accounts for the fact that the amplitude of the third harmonic current varies little, if at all, with frequency (Fig. 13).

A corresponding analysis with a quadratic variation of the capacity, instead of the a.c. leakage conductance, gives the wrong phase for the harmonic current; and also requires that it increase with frequency, which is likewise not observed. The analysis with a quadratic variation of the power factor, while giving the correct phase relations, requires that the amplitude of the harmonic current rise with frequency, in contradiction to the experimental results. We are thus led to the conclusion that the third harmonic current is due to a quadratic variation in the a.c. leakage conductance. This conclusion receives additional support from Fig. 15, where it is shown that the percentage of harmonics is directly proportional to the minimum formation

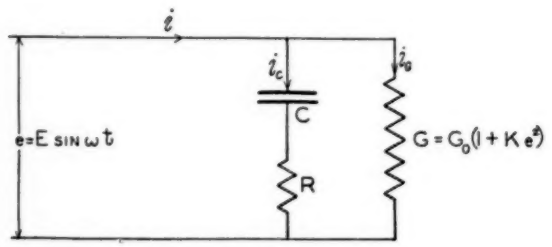

FIG. 16. Equivalent circuit of an electrolytic condenser when operated on an a.c. circuit. C, equivalent capacity of electrolytic condenser; R, equivalent series resistance representing power factor; G, equivalent leakage conductance to alternating current; G_0, limiting value of G for small a.c. voltages; K, proportionality constant; i, total current through condenser; i_C, current through equivalent capacity; i_G, current through equivalent a.c. leakage conductance.

[12] This expression, $G=G_0(1+ke^2)$, means that the total conductivity is of the form

$$g=G_0(e_1)\{1+k(e'-e_1)^2\}+f(e_1) \qquad (A)$$

where e' is the total potential drop across the layer and e_1 is the biasing voltage of the electrolyte. Some experiments which we have performed indicate that k is directly proportional to the biasing voltage. This variation of k with the biasing voltage is, however, a lagging effect, so it is not possible to express it explicitly in Eq. (A). The significance of Eq. (A) is that with each new biasing voltage, the anodic layer passes into a new equilibrium condition for which a current-voltage relation of the form, Eq. (2), holds.

current.[13] The agreement of the calculations with the results observed in Figs. 3 and 13 indicates that the time lag, if any, between the change of voltage and the change of conductance is less than 10^{-3} second.

It is not to be expected that the relation between leakage current and voltage derived from the presence of the third harmonic can be confirmed by reading the d.c. leak at consecutive voltages with a d.c. instrument. In the latter procedure, lagging changes of leak are superimposed upon the nonlagging changes and each point is unavoidably taken with the layer in a changed condition. The result of such a slow observation will vary according to the procedure of the experiment, i.e., how fast it is done, whether voltages are increased or decreased, and other arbitrary factors. Therefore, d.c. current *vs.* voltage curves have very limited significance for anodic layers. On the other hand, the results of our experiments on harmonics show that (in carefully made-up superviscous condensers and in such aqueous condensers as are not too alkaline and do not contain detrimental ions) for instantaneous variations of current with voltage, the relation $i=G_0(1+ke^2)$ holds.

The absence of harmonics of such magnitude as would correspond to the variations of capacity with voltage shown in Figs. 10 and 11, is additional evidence that these variations are lagging effects. It should be mentioned that a number of investigators have looked for capacity changes that could be correlated with the compressibility of the layer under the mechanical pressure on it caused by the electrostatic field. This pressure reaches in the neighborhood of 1000 kg/cm². Now, capacity changes due to pressure would be of a "nonlagging" character, and the oscillographic investigation of harmonics used here should bring them to light. Therefore, the absence of evidence of such changes of capacity indicates that the compressibility of the layer is very small. From this we may conclude that the layer cannot be of a gaseous nature, as has been assumed by some earlier investigators.

The authors wish to mention that Mr. Alfred Herzenberg was connected with this work during its initial period.

[13] Although it is not possible to get a direct measurement of the leakage current of an anodic layer in a.c. operation, it is known that the d.c. leak is about proportional to the minimum formation current, and it is therefore reasonable to suppose that in a general way a similar rule holds for the a.c. leak.

Author Index to Volume 6

References with (L) are to Letters to the Editor.

Alcock, E. D. and C. L. Sadron. Optical method for measuring the distribution of velocity gradients in a two-dimensional flow—92
Austin, J. B. and R. H. H. Pierce, Jr. Determination of the refractive index of vitreous silica and the calibration of silica refraction thermometers between 18° and −200°C —43

Bingham, Eugene C. and James E. Hatfield. Association by the fluidity method of substances which are solid at ordinary temperatures—64
Biot, M. A. Effect of certain discontinuities on the pressure distribution in a loaded soil—367
Björnståhl, Yngve. Influence of an electric field on the viscosity of aeolotropic liquids—257
Bozorth, Richard M. (see Dillinger, Joy F.)—279
——— **and Joy F. Dillinger.** Heat treatment of magnetic materials in a magnetic field. II. Experiments with two alloys—285
Burns, F. B. (see Traxler, R. N.)—58

Cady, W. G. Potential distribution between parallel plates and concentric cylinders due to any arbitrary distribution of space charge—10
Campbell, E. M. (see Macdonald, P. A.)—211
Chandler, L. (see Lilienfeld, J. E.)—416
Churchill, R. V. Comparison of the temperatures in a solid and its scaled model—100
Cleeton, Claud E. Grating theory and study of the magnetostatic oscillator frequency—207
Cookson, John W. (see Osterberg, Harold)—234, 246
Cravath, A. M. and L. B. Loeb. Mechanism of the high velocity of propagation of lightning discharges—125

Davis, C. W. Magnetic properties and orientation of ferromagnetic particles—96; Part II. Pyrrhotite—376
——— Some observations on the movement and demagnetization of ferromagnetic particles in alternating magnetic fields—184
Dillinger, Joy F. (see Bozorth, Richard M.)—285
——— **and Richard M. Bozorth.** Heat treatment of magnetic materials in a magnetic field. I. Survey of iron-cobalt-nickel alloys—279
Dillon, J. H. and P. M. Torrance. Method for measuring the pressure in a rubber extruding machine—53
Dow, R. B. Note on viscosity as a function of volume and temperature of oils—270
——— Viscosity of mixtures of liquids at high pressures—71

Ellwood, W. B. Magnetic hysteresis at low flux densities—215

Ferry, John D. and George S. Parks. Viscous properties of polyisobutylene—356
Frosch, C. J. V. Correlation of distillation range with the viscosity of creosote—165
——— VI. Correlation of the distillation range with the surface tension of creosote—171
——— VII. Correlation of distillation range with the interfacial tension of creosote against water—174

Gemant, A. Compressional waves in media with complex viscosity—363
Goldman, S. (see Lilienfeld, J. E.)—416
Gottschalk, V. H. Coercive force of magnetite powders—127
Gunder, Dwight F. Flexure problem for rectangular beams with slits—38; Erratum—256

Haskell, N. A. Motion of a viscous fluid under a surface load—265
Hatfield, James E. (see Bingham, Eugene C.)—64
Hayner, Lucy J. Shot effects of secondary electron currents —323
Heller, G. Dynamical similarity laws of the mercury high pressure discharge—389
Hestenes, Arnold D. and Harold Osterberg. General solution for the displacements of piezoelectric media which are subjected to constant electric fields—291

Kiehl, H. R. Erratum: Electrical conductivity of glass. Part I. The formation of highly resistant layers. Part II. Current increase phenomena with highly resistant layers—158
King, Ronold. Telegraphist's equations at ultra-high frequencies—121
Kunz, Jacob. Flow through submerged orifices—351

Lilienfeld, J. E., L. Chandler, Jr. and S. Goldman. Dielectric properties of anodic layers in aluminum electrolytic condensers—416
Loeb, L. B. (see Cravath, A. M.)—125

Macdonald, P. A. and E. M. Campbell. Floating grid direct-current amplifier—211
——— **and W. E. Turnbull.** Operating characteristics of the FP54 thermionic direct-current amplifying tube—304
Marchant, J. H., Jr. Temperature variation of the photoelectric emission from thorium oxide—202
Merkel, Wilhelm. Errata: Flow characteristics of sewage sludge and other thick materials—80
Minor, E. E. (see Whitehead, J. B.)—380
Mueller, Hans. Theory of photoelasticity in amorphous solids—179
Muskat, Morris. Note on mixed boundary value problems in logarithmic potential theory—27
——— Potential distributions about an infinitely extended line electrode on the surface of a horizontally stratified earth. II—14

——— Seepage of water through dams with vertical faces—402

Osterberg, Harold (see Hestenes, Arnold D.)—291
——— **and John W. Cookson.** Longitudinal, shear and transverse modes of vibration in quartz and tourmaline —246
——— **and John W. Cookson.** Theory of two-dimensional longitudinal and flexural vibrations in rectangular isotropic plates—234

Parks, George S. (see Ferry, John D.)—356
——— **and Monroe E. Spaght.** Some viscosity data for boron trioxide—69
Partlo, F. L. and Jerry H. Service. Instantaneous speeds in air of explosion reports at short distances from the source—1
Pearson, G. L. Shot effect and thermal agitation in an electron current limited by space charge—6
Pekeris, Chaim L. Propagation of Rayleigh waves in heterogeneous media—133; Addition—178(L)
Pierce, R. H. H., Jr. (see Austin, J. B.)—43
Pittman, C. U. (see Traxler, R. N.)—58
Poritsky, Hillel and Chauncey Guy Suits. Determination of arc temperature from sound velocity measurements. II—196

Rashevsky, N. On electric charges of disperse systems which are the seats of physico-chemical reactions—33
——— Further studies on mathematical physics of metabolizing systems with reference to living cells—343
——— Mathematical physics of metabolizing systems with reference to living cells—117
——— Mechanism of division of small liquid systems which are the seats of physico-chemical reactions. II. Instability of two-phase systems—35
——— Some physico-mathematical aspects of nerve conduction. II—308
Reed, D. W. (see Wyckoff, R. D.)—395
Reiner, Markus. Errata: Theory of non-Newtonian liquids—177
——— Errata: Viscometric studies of rubber solutions—177
Richardson, E. G. Volocity-gradient methods in rheology—273
Roberds, W. M. High frequency conductance of Pyrex glass in the presence of vapors—227

Sadron, C. L. (see Alcock, E. D.)—92
Schilling, Harold K. Growth of crystals of zinc containing cadmium by the Czochralski-Gomperz method—111
Seifriz, William. Effects of acids and alkalies on the viscous and structural properties of protoplasm—159
Serex, Paul (see Spooner, Laurence W.)—162
Service, Jerry H. (see Partlo, F. L.)—1
Sixtus, K. J. Magnetic anisotropy in silicon steel—105
Smith, Cyril Stanley. Magnetic susceptibility of some alloys of "gamma-brass" structure—47
Snoddy, L. B. Note on a problem in conduction—139
Spaght, Monroe E. (see Parks, George S.)—69
Spooner, Laurence W. and Paul Serex. New feature in the calibration of a capillary-tube viscometer—162
Stamm, Alfred J. Effect of changes in the equilibrium relative vapor pressure upon the capillary structure of wood—334
Suits, Chauncey Guy. Determination of arc temperature from sound velocity measurements. I—190
——— Study of arc temperatures by an optical method—315
——— (see Poritsky, Hillel)—196

Thatcher, Everett W. Multiple space charge effect—81
Tonks, Lewi. On anchoring the mercury pool cathode spot —294
Torrance, P. M. (see Dillon, J. H.)—53
Traxler, R. N., C. U. Pittman and F. B. Burns. Rheological properties of asphalt. II. Discussion of penetration-viscosity relationships—58
Turnbull, W. E. (see Macdonald, P. A.)—304

Walther, H. (see Wegel, R. L.)—141
Wegel, R. L. and H. Walther. Internal dissipation in solids for small cyclic strains—141
Whitehead, J. B. and E. E. Minor. Space charge in liquid dielectrics—380
Wikstrom, A. Some electrical properties of ceresin wax—86
Willihnganz, Eugene. Ostwald viscometers for petroleum oils—61
Wyckoff, R. D. and D. W. Reed. Electrical conduction models for the solution of water seepage problems—395

Analytic Subject Index to Volume 6

References with (L) are to Letters to the Editor.

Acoustics
Sound velocity in arc, C. G. Suits—190; H. Poritsky, C. G. Suits—196
Speeds in air of explosion reports, F. L. Partlo, J. H. Service—1
Arcs (see **Discharge of electricity in gases**)
Atmospheric electricity (see **Meterology**)

Biophysics
Acids and alkalies on protoplasm, W. Seifriz—159
Capillary structure of wood, A. J. Stamm—334
Division of small liquid systems, physico-chemical reactions, N. Rashevsky—35
Electric charges, physico-chemical reactions, N. Rashevsky—33
Metabolizing systems, living cells, physics of, N. Rashevsky—117, 343
Nerve conduction, N. Rashevsky—308

Capillary action (see also **Surface tension**)
Capillary structure of wood, equilibrium vapor pressure, A. J. Stamm—334
Crystalline state
Dissipation in solids for small cyclic strains, R. L. Wegel, H. Walther—141
Growth of single crystals of Zn containing Cd, H. K. Schilling—111
Heat treatment of ferromagnetic materials, R. M. Bozorth, J. F. Dillinger—285
Heat treatment of Fe-Co-Ni alloys in a magnetic field, J. F. Dillinger, R. M. Bozorth—279
Magnetic anisotropy in Si steel, K. J. Sixtus—105
Magnetic susceptibility of Cu and Ag alloys, C. S. Smith—47

Dielectrics and dielectric properties
Anodic layers in Al electrolytic condensers, J. E. Lilienfeld, L. Chandler, Jr., S. Goldman—416
Of ceresin wax, A. Wikstrom—86
Space charge in liquid dielectrics, J. B. Whitehead, E. E. Minor—380
Discharge of electricity in gases (see also **Spark discharge**)
Arc temperature, etc. from sound velocity, C. G. Suits—190; H. Poritsky, C. G. Suits—196
Arc temperatures by optical method, C. G. Suits—315
Hg pool cathode spot anchoring, L. Tonks—294
Similarity laws of Hg high pressure discharge, G. Heller—389
Discharge of electricity in high vacua
Multiple space charge effect, E. W. Thatcher—81
Shot effect and thermal agitation in space charge limited current, G. L. Pearson—6

Elasticity
Flexure problem for rectangular beams with slits, D. F. Gunder—38; Erratum—256
Modes of vibration in quartz and tourmaline, H. Osterberg, J. Cookson—246
Pressure distribution in a loaded soil; discontinuities, M. A. Biot—367
Rayleigh waves in heterogeneous media, C. L. Pekeris—133, 178(L)
Two-dimensional longitudinal and flexural vibrations in rectangular plates, H. Osterberg, J. W. Cookson—234
Waves in media with complex viscosity, A. Gemant—363
Electrical circuits
Telegraphist's equations at ultra-high frequencies, R. King—121
Electrical conductivity and resistance
Of ceresin wax, A. Wikstrom—86
High frequency conductance of Pyrex, W. M. Roberds—227
Electromagnetic waves
Grating and magnetostatic oscillator, C. E. Cleeton—207
Electron tubes
Commercial tubes in direct-current amplifiers, P. A. Macdonald, E. M. Campbell—211
FP54 direct-current amplifying tube, characteristics of, P. A. Macdonald, W. E. Turnbull—304
Multiple space charge effect, E. W. Thatcher—81
Electrons, secondary
And shot effects, L. J. Hayner—323
Electrostatics
Mixed boundary value problems in logarithmic potential, M. Muskat—27
Potential distribution due to space charge, W. G. Cady—10
Potential distributions about an extended line electrode, M. Muskat—14
Errata
Electrical conductivity of glass, H. R. Kiehl—158
Flexure problem for rectangular beams with slits, D. F. Gunder—38, 256
Flow characteristics of sewage sludge and other thick materials, W. Merkel—80
Theory of non-Newtonian liquids, M. Reiner—177
Viscometric studies of rubber solutions, M. Reiner—177

Fluidity (see **Viscosity**)

Geophysics
Plastic recoil of earth, N. A. Haskell—265
Potential distributions about an extended line electrode on horizontally stratified earth, M. Muskat—14
Pressure distribution in a loaded soil; discontinuities, M. A. Biot—367
Rayleigh waves in heterogeneous media, C. L. Pekeris—133, 178(L)
Seepage through dams with vertical faces, M. Muskat—402

Hydrodynamics
Electrical models for solution of seepage problems, R. D. Wyckoff, D. W. Reed—395

Flow through submerged orifices, J. Kunz—351
Gradients in a two-dimensional flow, C. L. Sadron, E. D. Alcock—92
Motion of viscous fluid under surface load, N. A. Haskell—265
Seepage through dams with vertical faces, M. Muskat—402
Velocity-gradient in viscous fluids, E. G. Richardson—273

Ions, mobility
In liquid dielectrics, J. B. Whitehead, E. E. Minor—380

Magnetic properties
Coercive force of magnetite powders, V. H. Gottschalk—127
Ferromagnetic particles in alternating fields, C. W. Davis—184
Heat treatment of Fe-Co-Ni in a magnetic field, J. F. Dillinger, R. M. Bozorth—279
Hysteresis at low flux densities, W. B. Ellwood—215
And orientation of ferromagnetic particles, C. W. Davis—96, 376
Of Si steel, anisotropy, K. J. Sixtus—105
Susceptibility of Cu and Ag alloys, C. S. Smith—47

Metals (see **Crystalline state**)

Meteorology
Propagation of lightning discharges, A. M. Cravath, L. B. Loeb—125

Methods and instruments
Capillary-tube viscometer, L. W. Spooner, P. Serex—162
Demagnetization of ferromagnetic particles, C. W. Davis—184
Direct-current amplifier, P. A. Macdonald, E. M. Campbell—211
Echelette for 1–10 cm electromagnetic waves, C. E. Cleeton—207
Electrical models for solution of seepage problems, R. D. Wyckoff, D. W. Reed—395
FP54 direct-current amplifying tube, characteristics of, P. A. Macdonald, W. E. Turnbull—304
Growth of single crystals of Zn containing Cd, H. K. Schilling—111
Magnetic hysteresis, W. B. Ellwood—215
Mixed boundary value problems, M. Muskat—27
Pressure in a rubber extruding machine, J. H. Dillon, P. M. Torrance—53
Silica refraction thermometers between 18° and −200°C, J. B. Austin, R. H. H. Pierce, Jr.—43
Similarity laws of Hg high pressure discharge, G. Heller—389
Temperatures in a solid and its scaled model, R. V. Churchill—100
Velocity gradients; optical method, E. D. Alcock, C. L. Sadron—92
Viscometers for petroleum oils, E. Willihnganz—61

Mobility of ions (see **Ions, mobility**)

Optical constants and properties
Refractive index of vitreous silica, J. B. Austin, R. H. H. Pierce, Jr.—43

Photoelasticity
Theory for amorphous solids, H. Mueller—179

Piezoelectric effect
Displacements of media subjected to electric fields, A. D. Hestenes, H. Osterberg—291
Modes of vibration in quartz and tourmaline, H. Osterberg, J. Cookson—246
Potential distribution due to space charge in dielectric, W. G. Cady—10
Two-dimensional longitudinal and flexural vibrations in rectangular plates, H. Osterberg, J. W. Cookson—234

Photoelectric effect and properties; cells
Temperature variation of photoelectric emission, J. H. Marchant, Jr.—202

Secondary electrons (see **Electrons, secondary**)

Shot effect
Of secondary electrons, L. J. Hayner—323
And thermal agitation in space charge limited current, G. L. Pearson—6

Sound (see **Acoustics**)

Spark discharge
Propagation of lightning discharges, A. M. Cravath, L. B. Loeb—125

Surface tension (see also **Capillary action**)
And distillation range of creosote, C. J. Frosch—171
Interfacial tension of creosote against H_2O, C. J. Frosch—174

Thermal conductivity
Problem in conduction, L. B. Snoddy—139
Temperatures in a solid and its scaled model, R. V. Churchill—100

Vacuum tubes (see **Electron tubes**)

Vapor pressure
And capillary structure of wood, A. J. Stamm—334

Viscosity
Of aeolotropic liquids, Y. Björnståhl—257
Association by fluidity method, E. C. Bingham, J. E. Hatfield—64
Of boron trioxide, G. S. Parks, M. E. Spaght—69
Calibration of a capillary-tube viscometer, L. W. Spooner, P. Serex—162
Dissipation in solids for small cyclic strains, R. L. Wegel, H. Walther—141
Distillation range and viscosity of creosote, C. J. Frosch—165
Of mixtures of liquids at high pressures, R. B. Dow—71
Motion of viscous fluid under surface load, N. A. Haskell—265
Of oils, as function of volume and temperature, R. B. Dow—270
Penetration-viscosity relationships in asphalt, R. N. Traxler, C. U. Pittman, F. B. Burns—58
Of polyisobutylene, J. D. Ferry, G. S. Parks—356
Properties of protoplasm, W. Seifriz—159
Velocity-gradient methods, E. G. Richardson—273
Viscometers for petroleum oils, E. Willihnganz—61
Waves in media with complex viscosity, A. Gemant—363